ADVANCING HEAT-TRANSFER AND IMPEDANCE BASED TRANSDUCER PLATFORMS FOR BIOMIMETIC RECEPTORS

Peter CORNELIS

Supervisors:
Promotor:
Prof. Dr. Patrick Wagner
Co-promotor:
Prof. Dr. Christ Glorieux

Members of the Examination Committee:
Prof. Dr. Michael Wübbenhorst
Prof. Dr. Carmen Bartic
Prof. Dr. Liesbet Lagae
Prof. Dr. Michael J. Schöning
Dr. Kasper Eersels

Dissertation presented in partial fulfilment of the requirements for the degree of Doctor in Science

June 2019

Preface

Completing all the work presented here has been very challenging at times and would not have been possible without the help and support of so many people. Therefore, I would like to take this opportunity to express my heartfelt appreciation and gratitude to all those who made it possible.

To be able to work and have a career in science has been a long-standing dream of mine. Realizing this after so many years is an incredible feeling that is very hard to put into words.

First of all, I would like to thank Professor Patrick Wagner for believing in my ability to obtain a master's degree in biomedical sciences, more specifically bioelectronics and nanotechnology, and for all his support, guidance and stimulating conversations. Without him I would probably never have had the chance to start this exciting and challenging Doctoral program.

I would also like to thank all the members of my supervisory committee, Prof. Dr. Carmen Bartic, and Prof. Dr. Liesbet Lagae, my co-promotor Prof. Dr. Christ Glorieux and the head of our laboratory Prof. Dr. Michael Wübbenhorst for guiding me and fine-tuning my PhD thesis through regular meetings and follow-up.

From the Institute of Nano-and Biotechnologies at the Aachen University of Applied Sciences in Jülich I would like to thank Prof. Dr. Michael J. Schöning, M. Eng. Heiko Iken, and Dr. Farnoosh Vahidpour for a very valued and close collaboration on many different projects.

A special thanks to Prof. Dr. Bart van Grinsven, and Dr. Kasper Eersels from the Maastricht Science Program at Maastricht for their invaluable scientific and technical support, discussions, great friendship, and all the fun and memorable moments in- and outside of the lab.

For providing a relaxed, entertaining and stimulating working environment I would like to extend my sincere gratitude to Drs. Gideon Wackers, Dr. Mehran Khorshid, Drs. Derick

Abstract

Biological receptors demonstrate a high affinity and selectivity towards their target, which is why they receive great interest for integration into biosensor applications. However, their instability in non-physiological conditions is a major drawback, which poses significant challenges. To address this, synthetic receptors have been developed that mimic these biological receptors. These so-called biomimetic receptors show a similarly high affinity and selectivity towards their target while also being very stable under non-physiological conditions.

This work focuses on advancing two widely used transducer platforms for use with these biomimetic receptors. The first platform is electrochemical impedance spectroscopy (EIS). For medical diagnostics, food-safety analysis and detection of environmental pollutants, simultaneous detection and quantification of multiple target molecules would be a great advantage. Commonly implemented systems use non-faradaic impedance spectroscopy. Adding a redox potential probe, such as silver/silver chloride, as a reference electrode besides the standard working and counter electrodes allows for the use of faradaic impedance spectroscopy techniques using redox-active molecules such as ferricyanide, thereby extending the range of possible applications through increased sensitivity of the measurements. Also, the ability to perform differential measurements would allow using undiluted patient samples, which significantly simplifies sample preparation. The differential impedimetric sensor cell (DISC) system, which has been designed and constructed in this work, meets all of these requirements as it can quasi-simultaneously analyze up to eight different targets inside a single small liquid sample. Furthermore, it was validated against a high-resolution dielectric spectrometer (Novocontrol, Alpha analyzer) using well characterized samples at different temperatures (25, 30, 35, 37, and 40 °C) over its whole frequency range (10 Hz – 100 kHz).

The second platform is a thermal technique based on the heat-transfer method (HTM). In this work, a novel biomimetic sensor based on this principle was designed, which allows for the sensitive and specific detection of *Escherichia coli* (*E. coli*) bacteria in a broad concentration range (10^2 - 10^6 CFU/mL) in buffer fluids as well as in relevant food samples (i.e., apple juice). Surface imprinted polymers (SIPs) were used as biomimetic receptors in this system. The increased sensitivity, which enables this low detection limit, originates from the planar meander heater element, which enables a more focused and efficient heat-flow through the system. Moreover, reference tests with other species of *Enterobacteriaceae* closely related to *E. coli*, show a very low cross-sensitivity: i.e., a sensor response at or below the noise level. Furthermore, the experiments performed in this part of the work show that the presence of bacteria enhances the thermal conductivity of a liquid.

Both systems designed in this work use a flow-through cell, which enables easy exchange of sample and buffer liquids during measurements. This allows the experience acquired during the design of one system to be implemented during the design of the other system and vice versa, or even combining both transducer platforms into a single system.

Samenvatting

Biologische receptoren vertonen een hoge affiniteit en selectiviteit voor hun doelwit, en daarom zijn ze zeer gegeerd voor integratie in biosensortoepassingen. Hun instabiliteit in niet-fysiologische omstandigheden is echter een groot nadeel, hetgeen aanzienlijke uitdagingen met zich meebrengt. Om dit aan te pakken, werden synthetische receptoren ontwikkeld die deze biologische receptoren nabootsen. Deze zogenaamde biomimetische receptoren vertonen een vergelijkbare hoge affiniteit en selectiviteit voor hun doelwit terwijl ze ook zeer stabiel zijn onder niet-fysiologische omstandigheden.

Dit werk richt zich op het uitbreiden van de toepassingsmogelijkheden en op het verbeteren van twee veel gebruikte transducerplatformen die gebruik kunnen maken van deze biomimetische receptoren. Het eerste platform is elektrochemische impedantiespectroscopie (EIS). Voor medische diagnostiek, voedsel-veiligheidsanalyse en detectie van milieuverontreinigende stoffen zou de gelijktijdige detectie en kwantificering van meerdere doelwitmoleculen een groot voordeel zijn. De meest voorkomende systemen maken gebruik van niet-faradische impedantiespectroscopie. Het toevoegen van een redox-potentiaal probe, zoals zilver/zilver-chloride, als referentie-elektrode naast de standaard counter- en werkings-elektrodes maakt het gebruik van faradische impedantiespectroscopie technieken mogelijk met behulp van redox-actieve moleculen zoals ijzercyanide, waardoor het aantal mogelijke toepassingen sterk uitgebreid wordt omwille van een verhoogde gevoeligheid van de metingen. Ook zou de mogelijkheid om differentiële metingen uit te voeren het gebruik van onverdunde patiënten stalen mogelijk maken, hetgeen de voorafgaande behandeling van stalen aanzienlijk vereenvoudigd. Het nieuwe differentieel impedimetrisch sensor-cel (DISC)-systeem, dat werd ontworpen en gebouwd in dit werk, voldoet aan al deze vereisten omdat het quasi-gelijktijdig verschillende doelwitten aanwezig in hetzelfde vloeibare staal kan analyseren. Bovendien werd

het gevalideerd ten opzichte van een hoge resolutie diëlektrische spectrometer (Novocontrol, Alpha-analysator) bij verschillende temperaturen (25, 30, 35, 37, en 40 °C) en over het gehele frequentiebereik (10 Hz - 100 kHz) met behulp van goed gekarakteriseerde stalen.

Het tweede platform is een thermische techniek gebaseerd op de warmteoverdrachtsmethode (Heat-Transfer Method - HTM). In dit werk werd een nieuwe biomimetische sensor op basis van dit principe ontworpen die een gevoelige en specifieke detectie van *Escherichia coli* (*E. coli*) bacteriën in een breed concentratiebereik (10^2 - 10^6 CFU/mL) in buffervloeistoffen ook mogelijk maakt in relevante voedselstalen (vb. appelsap). Oppervlakte-bedrukte polymeren (SIP's) werden gebruikt als biomimetische receptoren in dit systeem. De verhoogde gevoeligheid, die deze lage detectiegrens mogelijk maakt, resulteert uit het gebruik van een vlak meandervormig verwarmingselement hetgeen een meer gerichte en efficiënte warmtestroom door het systeem mogelijk maakt. Bovendien vertonen referentietests met andere soorten *Enterobacteriaceae*, die nauw verwant zijn aan *E. coli*, een zeer lage kruisgevoeligheid: d.w.z., een sensorrespons op of onder het ruisniveau. Bovendien tonen de experimenten, die in dit deel van het werk werden uitgevoerd, aan dat de aanwezigheid van bacteriën de thermische geleidbaarheid van een vloeistof verbetert.

Beide systemen die in dit werk werden ontworpen, maken gebruik van een doorstroom flow-cel, die een eenvoudige uitwisseling van staal- en buffervloeistoffen tijdens metingen mogelijk maakt. Hierdoor kan de ervaring die tijdens het ontwerpen van het ene systeem werd opgedaan, worden geïmplementeerd tijdens het ontwerp van het andere systeem en omgekeerd, of is het zelfs mogelijk beide transducerplatforms in één systeem te combineren.

Table of Contents

List of Figures

List of Tables

List of Symbols and Abbreviations

A/D	Analogue to Digital
AAC	Acoustic Alternating Contact (Tapping Mode)
AFM	Atomic Force Microscopy
AISI	American Iron and Steel Institute
c	Cell constant
C	Capacitor
C_{DL}	Double-Layer Capacitance
Ch.	Channel
C_L	Liquid Capacitance
CFU	Colony Forming Unit
D/A	Digital to Analogue
DISC	Differential Impedimetric Sensor Cell
DMM	Digital multi-meter
DNA	DeoxyriboNucleic Acid
DPPC	Dipalmitoylphosphatidylcholine
DROID	Dual Reference Organic Impedimetric Device
EBU	Electronic Base Unit
EC	European Commission
EIS	Electrochemical Impedance Spectroscopy
ELISA	Enzyme-Linked Immuno Sorbent Assay
EU	European Union
f	Frequency
FLOF	Facultair Luik OnderzoeksFonds (PhD bursary financed by the Department)
FWO	Fonds Wetenschappelijk Onderzoek (Research Foundation Flanders)

HTM	Heat-Transfer Method
I/O	Input/Output
IC	Integrated Circuit (microchip)
I²C	Inter-IC
ISO	International Organization for Standardization
L	Coil
LB	Lysogeny Broth
LoD	Limit of Detection
MIP	Molecularly Imprinted Polymer
MPN	Most Probable Number
M_W	Molecular Weight
NCSTR	Non-Contact / Soft Tapping Recording (AFM)
NIP	Non-Imprinted Polymer
NIR	Near Infrared Spectrum
OD600	Optical Density at 600 nm
P	Power
PBS	Phosphate Buffered Saline
PCR	Polymerase Chain Reaction
PDMS	PolyDiMethylSiloxane
PEEK	PolyEther Ether Ketone
PID	Proportional, Integral, Derivative
pK_a	Logaritmic acid dissociation constant
PMMA	Poly(Methyl MethAcrylate)
Pt100	Platinum resistor (100 Ω at 0 °C)
PU	PolyUrethane

QCM	Quartz Crystal Microbalance
R	Resistance
R_{CT}	Charge-Transfer Resistance
R_L	Liquid Resistance
R_S	Device Resistance
R_{th}	Heat-transfer resistance
SAM	Self-Assembled Monolayer
SDS	Sodium DodecylSulfate
SEM	Scanning Electron Microscopy
SIP	Surface Imprinted Polymer
SPM	Scanning Probe Microscopy
SPR	Surface Plasmon Resonance
T_A	Ambient Temperature
T_C	Flow-cell Temperature
T_H	Heater Temperature
TCR	Thermal Coefficient of Resistivity
THF	TetraHydroFuran
TWTA	Thermal Wave Transport Analysis
USB	Universal Serial Bus
VIS	Visible Spectrum
W	Warburg element
Z	Impedance
ZMB	Zachte Materie en Biofysica (Soft Matter and Biophysics)
$\bar{\alpha}$	Time constant in Newton's law of cooling and heating
γ_{PBS}	PBS conductivity

Ω   Ohm

ø   Diameter

Chapter 1: General Introduction

Biological receptors have a very strong affinity and selectivity towards their targets. This has already been the subject of various studies for many years[1-4]. The incorporation of these receptors into sensor applications faces specific challenges as they are often not very stable under non-physiological conditions. In recent years, biomimetic receptors have been developed to address these challenges[5, 6]. The specific properties of these receptors will further be described in more detail. Upon binding of targets to these receptors, their properties change, and these changes will be measured by so-called transducer platforms. Widely used platforms are electro-chemical, optical, micro-gravimetric, and thermal techniques.

This work focuses specifically on extending the range of possible applications for an electrochemical read-out platform and improving the sensitivity of a thermal read-out platform, respectively electrochemical impedance spectroscopy (EIS) and the heat-transfer method (HTM). Several physical characterization techniques will be used along the way to assist in validating the enhanced transducer platforms. Chapter 2 focuses on the electrochemical and Chapter 3 on the thermal transducer platform.

Most of the software used in this work was developed in-house. An in-depth description of the main features of these software packages is provided in Chapter 4. Moreover, a slightly adapted version of the program for HTM measurements has been successfully used in many other projects[7-11].

1.1 Biomimetic Receptors

Over millions of years of evolution, nature has produced receptors with a remarkably high affinity for their targets. Therefore, biosensors, which are based on these receptors allow the development of sensors systems with very high selectivity and sensitivity. Several types of

biosensors are available, such as enzymes[2, 3], aptamers[12, 13], and antibodies[14, 15]. However, their isolation and purification from nature is usually very expensive and labor-intensive. Moreover, another drawback is their limited physical and chemical stability, which leads to a short shelf-life for these types of biosensors.

To overcome these drawbacks, biomimetic receptors have been developed[5]. These are physically and chemically stable synthetic receptors with an affinity for their target, which is comparable to their natural counterparts. In other words, they copy/mimic the function of biological receptors, which is why they are called biomimetic receptors. The most wide-spread of this kind of receptor are the molecularly imprinted polymers (MIPs)[16]. These are created by polymerizing a mixture of suitable functional monomers, a cross-linker, and optionally a reaction initiator, in the presence of the selected target, at this stage denominated as template. Afterwards, the template is washed out of the created polymer leaving behind small cavities that can selectively rebind the target during measurements. It is important to note that the physiological conditions, especially the pH, during the polymerization process should be similar to the conditions during measurements because the bond between target and polymer mainly depends on the formation of hydrogen bridges. Changes in pH can cause changes in the protonation level of the target and/or the polymer, which not only changes the number of possible hydrogen bridges, but also the charge distribution in the system. These changes weaken the bond or even create repulsive forces between the target and the polymer, which can significantly reduce the affinity of the MIP for its target. The possible pH ranges for measurements using MIPs therefore depends on the acid dissociation constant(s) (pK_a) of the target and of the functional monomers. MIPs have been synthesized for various targets: from small molecules, like histamine[17, 18], up to macromolecular structures, such as proteins[19-21]. However, the extraction of the target from the polymer can pose significant challenges. The working principle behind MIPs is based on the fact that rebinding of the target to the cavities

in the MIP changes the properties of the interface between the polymer and the surrounding liquid, which in turn can be detected by a suitable transducer platform. Surface imprinted polymers (SIPs) are another group of biomimetic receptors[22]. Their working principle is similar to the one for MIPs. However, they allow the use of much larger targets, such as whole cells. **Figure 1-1** illustrates the working principle behind both MIPs and SIPs for the transducer platforms used in this work. In essence, a target that binds to a cavity increases the electrical resistance, in case of electrochemical impedance spectroscopy (EIS)[23], or the heat-transfer resistance, in case of the heat-transfer method (HTM)[24], across the interface.
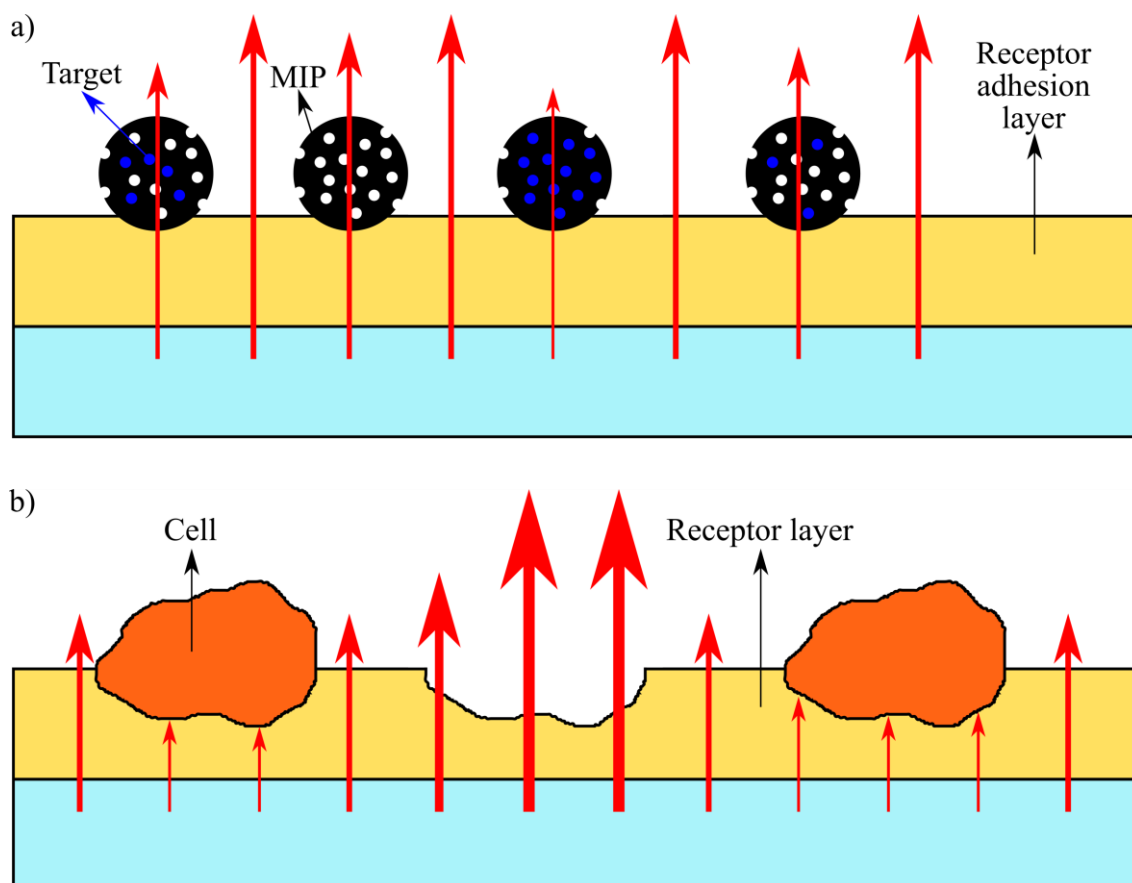
Figure 1-1 *Schematic illustration of the MIP (a) and SIP (b) working principle. The red arrows indicate the flow of electrical current, in case of electrochemical impedance spectroscopy, or heat, in case of the heat-transfer method. Thinner lines represent higher resistivity. Thus, upon target binding the electrical and heat resistivity increases. These changes in resistivity can then be measured by their respective transducer platform.*

1.2 Transducer Platforms

1.2.1 Electrochemical Impedance Spectroscopy (EIS)

The basic idea of electrical resistance is well known. It is the ability of a material to resist the flow of an electrical current. For an ideal conductor this resistance (R) is defined by Ohm's law (**Equation 1.1**) in terms of the ratio between the potential difference across the resistor (V) and the current running through the resistor (I).

$$R = \frac{V}{I} \hspace{4cm} (1.1)$$

This relationship only holds for 'ohmic' or 'linear' resistors, i.e. when the potential difference across it varies linearly with the current. On the other hand, real world systems exhibit a much more complex behavior. For these systems the basic idea of linear electric resistance must be extended to impedance, which provides a more general description. Like resistance, impedance is a measure for the ability of a material to resist the flow of an electrical current. However, unlike ohmic resistance, AC voltage and current signals can differ in phase from each other, and the impedance amplitude can also be frequency dependent.

For impedance measurements, electrochemical cells are used, which in this case are devices capable of using electrical energy to cause redox chemistry. Therefore, biomimetic receptors that are electrically conductive are preferred in these applications. Electrochemical impedance is the response of these electrochemical cells to an applied AC voltage signal. Low amplitude voltage signals are used to make sure that the response of the electrochemical system is quasi-linear. This in turn ensures that the input and output signal have the same frequency and can only potentially differ in phase. The frequency dependence of the electrochemical impedance allows for analyzing the underlying chemical processes inside the electrochemical cell. For example, low frequencies can be used to assess certain interfacial characteristics of the sensor surface, while high (> 1 kHz) frequencies can be used to assess the conductive features of the

sample liquid. However, most electrochemical cells contain multiple inductive, capacitive, and resistive elements, which infers a complex composition of global impedance signal. Therefore, equivalent circuits are used to model the cells, which allows analyzing the individual elements of the cell. **Figure 1-2** shows a simplified so called Randles cell[25] as an example of such an equivalent circuit.
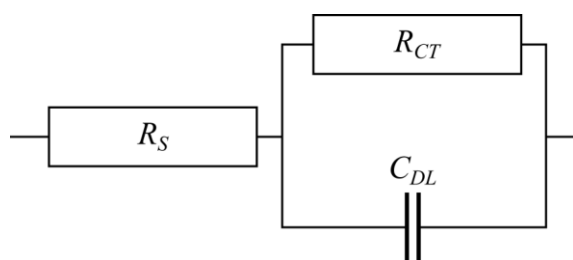
Figure 1-2 *Equivalent circuit of a simplified Randles cell. With R_S the electrolyte resistance, R_{CT} the charge-transfer resistance between the electrode and the electrolyte, and C_{DL} the double-layer capacitance caused by a ionic layer formed at the electrode-electrolyte interface.*

This circuit consists of an electrolyte resistor (R_S), which is the resistance of the liquid between the electrodes of the impedance analyzer, in series with a charge-transfer resistor (R_{CT}), which models the transfer of charge between the electrodes and the liquid, and a double-layer capacitor (C_{DL}), which models the ionic layer formed at the electrode-electrolyte interface, in parallel. The complex response of the system is usually displayed in Nyquist format, which plots the real part against the imaginary part of the response. As most of these electrochemical systems are inherently capacitive. The current lags behind the potential difference and the complex impedance has a negative phase, i.e. a negative imaginary part. Therefore, the imaginary part is inverted (**Figure 1-3A**). However, looking at any datapoint on this plot, it is impossible to know at which frequency it was recorded. To solve this, Bode-plots are used, which plot the amplitude and phase of the signal against the logarithm of the frequency (**Figure 1-3B**). Depending on its range of values, the impedance amplitude is sometimes also plotted on a

logarithmic scale as demonstrated in **Figure 1-3B**. A Randles cell with chosen values for R_S (560 Ω), R_{CT} (10 kΩ), and C_{DL} (33 nF) was used to create these graphs. **Figure 1-3B** also shows that at the lowest frequencies R_{CT} is the main contributing element in the impedance signal, while at the highest frequencies R_S is the main contributing element. This infers that low frequencies allow analyzing the sensor surface characteristics, while high frequencies allow analyzing conductive properties of the sample liquid.
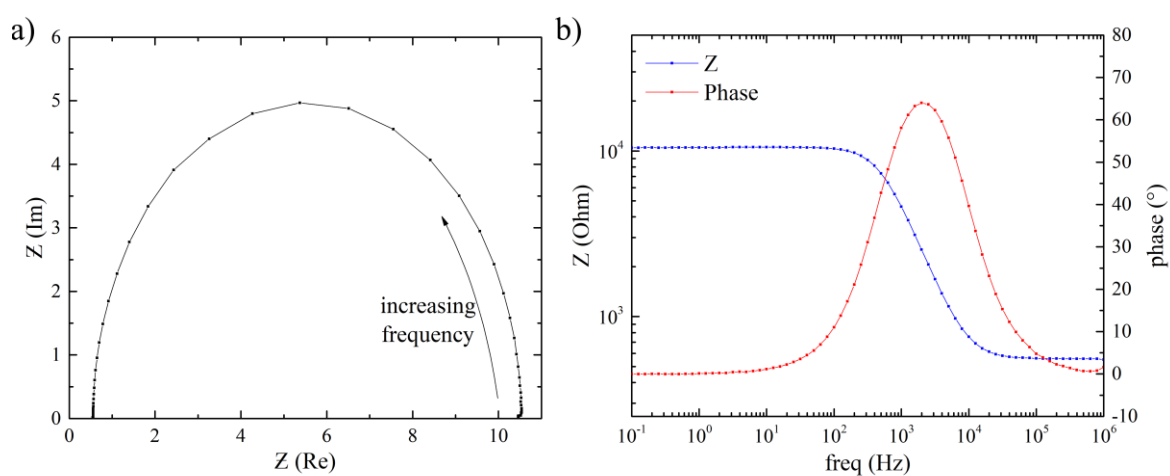
Figure 1-3 *Example data plots in Nyquist (a) and Bode (b) format of an electrochemical impedance spectrum for a simplified Randles cell ($R_S = 560$ Ω, $R_{CT} = 10$ kΩ, $C_{DL} = 33$ nF).*

Any complex electrochemical system can be modelled as a serial and/or parallel combination of basic electrical circuit elements. In addition, processes that depend on the diffusion of reactants towards or away from the surface have a low-frequency character, which is described by the so-called "Warburg" impedance[26, 27]. So, these need to be considered when designing the equivalent circuit that models the electrochemical system. It is important to note that their contribution increases as the distance between the two electrodes inside the measurement cell decreases: i.e., the distance the signal has to travel through the liquid inside the cell. Each element has a specific expression to calculate its impedance. However, several expressions are

available to describe "Warburg" elements. To minimize the complexity of the model describing the electrochemical system, general "Warburg" elements, which are a special case of constant phase elements (CPE) with a phase angle of 45° independent of frequency (**Table 1-1**), are used in all further calculations.

Table 1-1 *Formulas to calculate the impedance of various circuit elements used to design an equivalent circuit to model an electrochemical system.*

Circuit element	Description	Impedance
R	Resistor	R
C	Capacitor	$\dfrac{1}{i\omega C}$
L	Coil	$i\omega L$
W	Warburg element (CPE with 45° phase)	$(1-i) \cdot \dfrac{A_w}{\sqrt{\omega}}$

The two main categories of EIS-based transducer platforms[28] are: faradaic (f-EIS)[29] and non-faradaic (nf-EIS)[30]. The difference between the two types is the use of a reduction/oxidation (redox) reagent, such as ferricyanide ($Fe(CN)_6^{3-/4-}$), combined with an additional DC offset voltage in case of f-EIS[29]. The redox reagent enables a higher sensitivity by generating higher electrical currents through the sensor interface. However, the DC voltages required to stimulate the redox reactions that produce these high electrical currents significantly exceed the 70 mV resting potential of living cells[31]. For this reason, nf-EIS is preferred in biological applications using cells and specifically for applications inside the human body. Both categories of EIS-based transducer platforms also differ in the contributions of the different elements in their respective equivalent circuits. In f-EIS the charge-transfer resistance (R_{CT}) is the component

that correlates with the concentration of a target at the sensor surface, while in nf-EIS it is the double-layer capacitance (C_{DL}).

1.2.2 Heat-Transfer Method (HTM)

It is well established that the thermal resistance at the interface between two different materials has an additional contribution known as thermal interface resistance. This was studied for the first time by P. L. Kapitza in 1941 on interfaces between copper and superfluid helium and attributed to the fact that the mechanisms of thermal conductance in both materials are different[32]. This thermal resistance was also studied for other interfaces between solids and liquids and between dissimilar solids. Heat propagation is considered to be mainly based on sound waves and different materials have evidently different sound velocities and phonon frequencies. Combining these elements, one can calculate the probability that phonons are transmitted from one medium to the other or are reflected at the interface in the framework of the Acoustic Mismatch Model AMM or the more refined Diffusive Mismatch Model DMM[33, 34]. The decisive quantity that describes the transmission- and reflection probabilities (hence the macroscopic interface resistance) is the amount of acoustic impedance matching between both materials, given by the product of their mass densities and sound velocities. In the context of biosensors, van Grinsven et al. found in 2012 that the thermal interface resistance between a solid chip (silicon covered with synthetic diamond) and the supernatant liquid increases substantially when double-stranded DNA (covalently bound to the chip) undergoes thermal denaturation to single-stranded DNA[35]. The measured quantity that represents the thermal conductance across the interface is the so-called thermal resistance R_{th}, which was originally introduced as a parameter that describes the heat dissipation from integrated-circuit devices[36]. Applied to a biosensing situation in which the chip is heated from the backside, R_{th} is given as the ratio between the temperature difference between the backside of the chip and the liquid on

top of the interface, divided by the supplied heating power (**Equation 1.2**). This way of measuring, the configuration is illustrated in **Figure 1-4**, is termed the Heat-Transfer Method (HTM), and many more applications have been studied and identified since the original proof-of-concept with the HTM-based detection of single-nucleotide polymorphisms (SNPs) in DNA[35]. Combined with MIPs it is possible to detect small molecules such as the inflammation mediator histamine[37] and the neurotransmitter serotonin[38]. Aptamer-based biosensors can be used to detect proteins such as the peanut allergen Ara h1[39]. Whole cells can be detected using SIPs[40, 41]. It is even possible to monitor the growth of micro-organisms like *saccharomyces cerevisiae*[42], and to detect phase transitions in lipid vesicles consisting of bilayers of dipalmitoylphosphatidylcholine (DPPC)[43].

HTM is a low-cost technique as it only requires a controlled heat source and a second temperature measurement, and it does not need any kind of labelling of the target or the sensor. More specifically, the heat source is kept at a predefined temperature using a proportional–integral–derivative (PID) controller and a temperature sensor (T_H), the temperature of the liquid in the flow cell positioned above the heat source is monitored by a second temperature sensor (T_C), and the sensor itself is positioned between the heat source and the liquid, with its sensitive side towards the liquid (**Figure 1-4**). As mentioned above, the thermal resistance (R_{th}) can then be calculated by dividing the temperature difference ($T_H - T_C$) by the power (P) required to keep the heat source at its predefined temperature (**Equation 1.2**).

$$R_{th} = \frac{(T_H - T_C)}{P} \qquad\qquad (1.2)$$
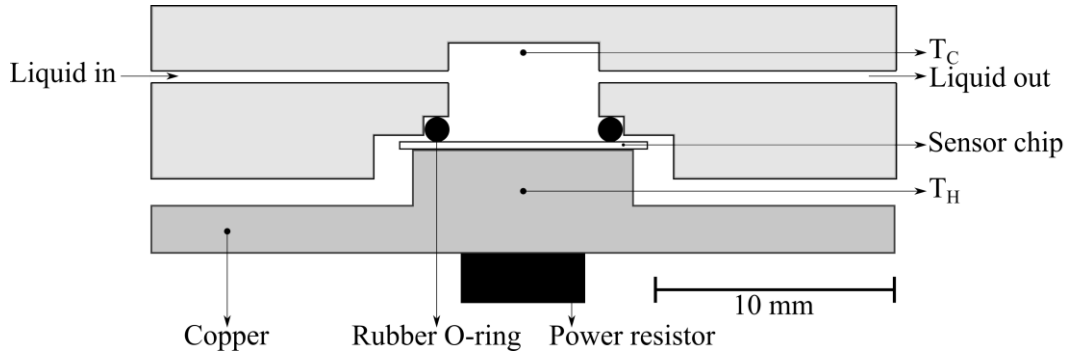
Figure 1-4 *Schematic drawing of a setup using the heat-transfer method (HTM) technique. All elements are drawn to scale.*

Figure 1-5 shows a typical HTM measurement curve for cell detection using SIPs[40] exemplarily for the rat macrophage cell line NR8383. There is a significant amount of noise on the signal, which has three contributing factors: The noise on the power (P) supplied by the heater, and on the measurement of temperatures T_H and T_C. As an important part of Chapter 3, the aim of this work is to reduce this noise in order to lower the limit of detection (LoD) of the HTM measurement system.
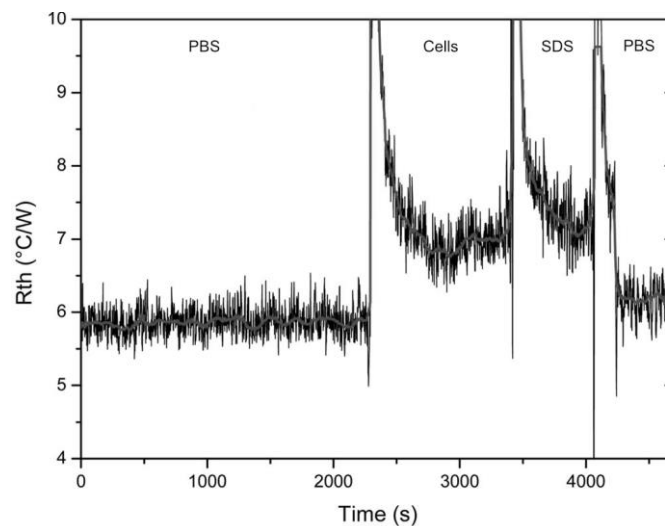
Figure 1-5 *Example of a typical HTM measurement for cell detection using SIPs which was adapted from Eersels et al.* [40]. *The measurement starts in PBS followed by the injection of cells, which cause a rise in the R_{th}. Next, an anionic detergent is injected to remove all the bound cells from the sensor surface. Finally, PBS was injected to verify the removal of all the bound cells.*

1.3 Physical Characterization Techniques

1.3.1 Contact Angle Measurement

Contact angle measurements are commonly used to determine the wetting behavior of combinations of solid surfaces and liquids[44]. They are a measure for the similarity in the level of hydrophobicity between the liquid and the solid surface. In other words, more similar levels enable the liquid to more easily cover the surface with a thin homogeneous layer (good wetting). The contact angle is defined as the angle (θ) between the solid-liquid interface and the tangent on the surface of the liquid drop starting at the border of the solid-liquid interface (**Figure 1-6**).
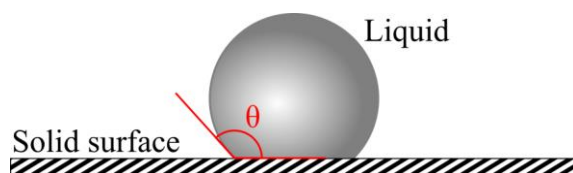
Figure 1-6 *Illustration of a contact angle measurement.*

To measure the contact angle a small drop of liquid is dropped onto the solid surface and a picture is taken perpendicular to the solid-liquid interface and consequently analyzed. For example, using water as the testing liquid, small contact angles correspond to hydrophilic surfaces and large contact angles correspond to hydrophobic surfaces.

In this work, contact angle measurements were used to analyze the hydrophobicity of the surface imprinted polymers, which were used to detect *E. coli* with an HTM-based technique. During the imprinting process parts of the cell membrane can get incorporated into the SIP[45]. Cell membranes mainly consist of a phospholipid bilayer. Phospholipids are amphiphilic molecules, which have a hydrophilic head group and a hydrophobic tail. The hydrophobic tails form the center of the membrane, while the hydrophilic heads form the outer layer of the membrane. Therefore, the heads of the phospholipids get incorporated into the SIP leaving the

hydrophobic tails exposed on the sensor surface as the inner layer of the cell membrane separates from the outer layer during cell extraction from the sensor surface. Comparing SIPs made using *E. coli* and SIPs made using solid silica beads of equivalent size, the *E. coli* SIPs are more hydrophobic as evidenced by an increased contact angle[45].

1.3.2 Fluorescence Microscopy

The fluorescence microscopy technique is an essential tool in biology and biomedical sciences because of its ability to identify cells, sub-microscopic cellular components, and even single molecules with a high degree of specificity in an otherwise heterogenous non-fluorescent matrix[46]. Its working principle is based on the specific properties of fluorochromes, also known as fluorescent labels. These molecules absorb light of a specific wavelength, after which they immediately or with a short delay time (1 - 100 ns) re-emit light at a slightly longer wavelength, and with a lower intensity (**Figure 1-7**). This shift in wavelength between the absorption spectrum of the fluorochrome and its emission spectrum is the phenomenon known as Stokes shift[47].
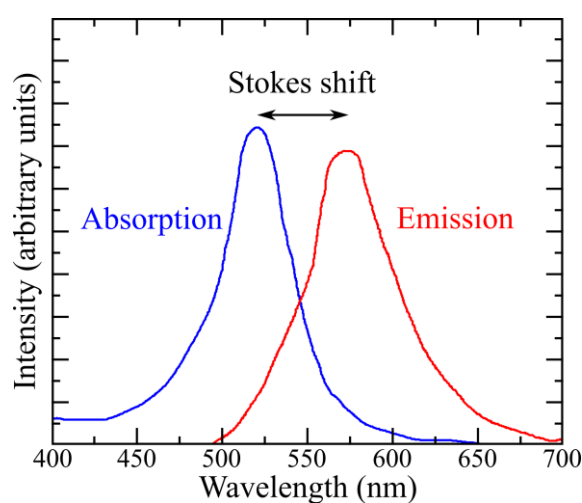
Figure 1-7 *Artist illustration of the absorption and emission spectra of a fluorochrome with a 50 nm Stokes shift[47].*

When combined with an appropriate band-pass, notch or long-pass filter, it allows to remove all light other than the emission wavelength from the microscope image. This creates a high contrast image on which the location of the fluorochromes can be easily identified. However, these fluorochromes are susceptible to the so-called photobleaching effect. This means that over time and especially under intense light exposure, which includes wavelengths in the range of their absorption spectrum, they lose their fluorescent properties.

In this work this technique was used to verify the presence or absence of *E. coli* bacteria respectively during the SIP imprinting process and after washing the SIPs to confirm that all template cells were removed. Moreover, it was also used to assess the surface coverage of the SIPs with *E. coli*. During the imprinting, the SIP should ideally be covered with a monolayer of bacteria consisting of individual cells: i.e. as many cells as possible without clustering, which is when two or more cells stick together to form larger structures. For this purpose, the pRSETb-mEmerald plasmid was inserted into the *E. coli* bacteria. The mEmerald fluorochrome emits green light (510 nm) when exposed to a blue light source (489 nm)[48]. In other words, it has a stokes shift of 21 nm.

1.3.3 Atomic Force Microscopy (AFM)

To evaluate for example surface roughness or the topography of a cell imprint on a surface imprinted polymer, imaging techniques with a spatial resolution in the nanometer or even fractions of a nanometer range are required. Due to the optical diffraction limit these high resolutions are unattainable for optical microscopes. Fluorescent microscopes can practically reach a resolution of 0.2 µm, which translates to a maximum magnification of 2000 ×. One way to overcome this limitation is the use of focused beams of electrons instead of light beams. These beams have much shorter wavelengths, which enables higher resolution images. However, the basic principle behind this technique is the same as for standard optical

microscopy, which is focusing beams of electromagnetic waves to produce magnified images. The scanning electron microscope (SEM) is an example of this technique[49], which can reach a resolution of 10 nm, which translates to a $10^5 \times$ magnification factor. Unfortunately, the sample pre-treatment required for this technique is destructive for biological material.

In contrast, the atomic force microscope (AFM) uses the atomic forces between a probe and a sample to create an image of the sample[50], which allow it to reach a resolution of 0.5 nm ($10^6 \times$ magnification). **Figure 1-8** shows the typical configuration of an AFM. A small tip, which is fixed to the open end of a cantilever, acts as the probe. A detector, located above this tip, monitors the deflection and motion of the cantilever, which are influenced by the atomic forces between the tip and the sample. The amplitude of these forces depends on their mutual distance.
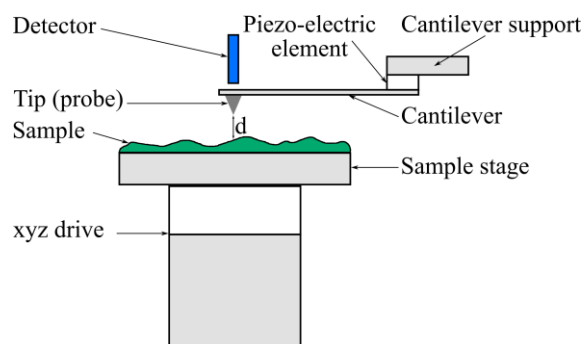
Figure 1-8 *Typical configuration of an AFM. The piezo-electric element is optional and only used in tapping and non-contact mode imaging.*

The AFM can be used in three modes: Contact, tapping, and non-contact mode. In this work the microscope was used in tapping mode because the samples were measured in ambient conditions. Under these conditions most samples form a thin liquid layer on their surface, which interferes with the short-range forces between the probe and the sample. In order to bypass this problem, the cantilever was driven to oscillate near its resonance frequency using a small piezo-electric element between the cantilever and its support. The amplitude of the oscillation was

kept constant using a feedback loop which controls the distance between the probe and the sample. As the probe oscillates it made intermittent contact with the sample. The AFM images made in tapping mode were therefore produced by visualizing the force of these intermittent contacts.

In this work, this technique was used to create images of the cavities left behind in de SIP layer as to analyze their size and shape. Moreover, these images were used to compare SIPs created on different types of support materials, such as glass, aluminum, and stainless-steel. Additionally, images with a slightly lower magnification were used to calculate the surface coverage of the SIP (number of cavities per square centimeter).

1.3.4 Thermal Coefficient of Resistivity (TCR)

The electrical resistance of solid materials depends on their temperature[51]. The rate at which the resistance changes depends on the thermal coefficient of resistivity (α) of the material as can be seen in **equation 1.3**. This property plays an important role in Chapter 3.

$$R_{T_1} = R_0\big(1 + \alpha(T_1 - T_0)\big) \tag{1.3}$$

Most pure metals (copper, silver, etc.) have a positive TCR: their electrical resistance increases as their temperature rises. On the other hand, some semiconductor materials (carbon, germanium, etc.) have a negative TCR as their electrical resistance decreases with increasing temperatures. The TCR of some alloys, for example constantan and manganin, is so low that they can be considered to be zero, making their electrical resistance virtually insensitive to changes in temperature. **Table 1-2** shows an overview of the resistivity and TCR of these materials.

Table 1-2 *Literature values for the resistivity and TCR of common materials. The electrical resistance of materials with a positive TCR rises as they get warmer, in contrast to materials with a negative TCR whose resistance lowers as they get warmer. The TCR of some materials is so close to zero that their resistance can be considered as independent of temperature.*

Material	Resistivity (ρ) (Ω.m)[52]	TCR (α) (°C⁻¹)[53]
Copper	$1.724 \cdot 10^{-8}$	0.0039
Silver	$1.59 \cdot 10^{-8}$	0.0061
Gold	$2.24 \cdot 10^{-8}$	0.0034
Carbon	$(3 - 60) \cdot 10^{-5}$	-0.0005
Germanium	$(1 - 500) \cdot 10^{-3}$	-0.048
Constantan	$49 \cdot 10^{-8}$	0.000008
Manganin	$4.2 \cdot 10^{-7}$	0.000002

For this work, a gold meander-based heater was used (**Figure 1-9A**). They were made by H. Iken at Aachen University of Applied Sciences (FH Aachen) in Jülich using a lithographic process to deposit a 100 nm thick gold pattern onto a 1 mm thick glass support (10×15 mm²) using a 10 nm thick chromium adhesion layer. The lines of the meander are 100 µm wide with an interline distance of 50 µm. In order for it to function as a controllable heat source, its electrical resistance was employed to monitor its temperature. So before use, each heater needed to be calibrated in order to correlate its electrical resistance with its temperature. To achieve this the heater was placed near a factory-calibrated Pt100 temperature sensor and slowly in an oven without air convection (**Figure 1-9B-C**). In the temperature range 0 - 100 °C, the correlation can be considered as linear, as demonstrated by the linear fit shown in **Figure 1-10A**. As the heater's meander structure was almost entirely composed of gold, its calibration could be validated by calculating its TCR (($2.8 \pm 0.02) \cdot 10^{-3}$ °C⁻¹) and comparing it to the literature value of gold[53] (TCR $= 3.4 \cdot 10^{-3}$ °C⁻¹) (**Figure 1-10B**).
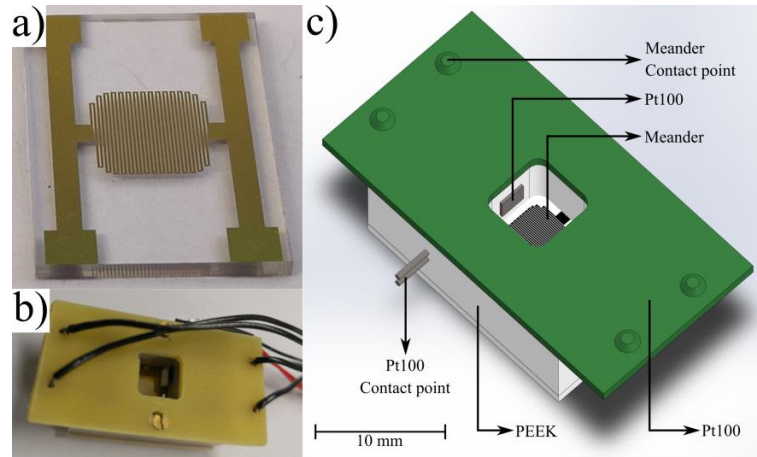
Figure 1-9 *Picture of the gold meander-based heater (a) and the calibration device (b). Schematic illustration of the device used to calibrate the meander-based heaters (c).*
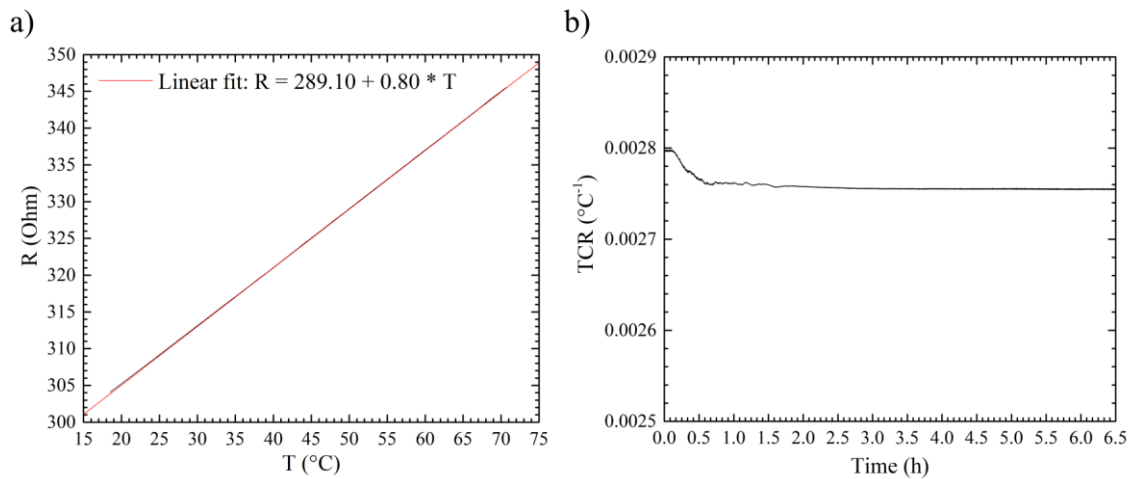
Figure 1-10 *a) Calibration data for a meander-based heater. The red line indicates a linear fit of the data with an R^2-value of 0.99. b) Values for the thermal coefficient of resistance (TCR) as a function of time (calculated from the calibration data).*

In order to choose the appropriate material to produce the meander-based heaters it is important to find a good balance between resistivity, the TCR value and long-term stability (corrosion-resistance, etc.). A change of around 1 Ω/°C for the total meander resistance allows reaching a temperature measurement sensitivity of at least 0.1 °C using standard measuring equipment. Using gold, the meander can cover a relatively large area (5 × 5 mm²) with a total resistance of 450 Ω and a temperature dependency of 1.5 Ω/°C. The meander lines are 100 µm wide with an interline distance of 50 µm. Furthermore, it is very corrosion-resistant and unaffected by air,

water, alkalis and all acids except aqua regia. Silver and copper would also be good candidates regarding their TCR. However, silver readily forms a surface tarnish of silver sulphide and copper reacts with moist air to form a protective oxide layer. These effects change the electrical conductivity of the material over time, which is unfavourable for achieving the required measurement precision that can also be maintained over longer periods of time. Moreover, it requires adding a protective layer to the contact pads to make sure the connections to the measurement device stay in good condition and do not add additional contact resistances.

1.4 Electrical Resistance Measurements

1.4.1 2-Wire vs. 4-Wire Concept

The most commonly used method to determine the electrical resistance is the 2-wire measurement technique using a digital multi-meter (DMM) (**Figure 1-11**). A test current large enough to measure the voltage drop over the resistor to be tested is sent through the lead wires between the DMM and the resistor under test. As the current magnitude is known, the resistance can be calculated from the measured voltage drop over the resistor using Ohm's law (**Equation 1.1**). However, the voltage drop is measured inside the DMM (V_M). The current running through the system during measurement is high enough to cause a voltage drop across the lead wires. So, the voltage measured by the DMM is the sum of the voltage drop over the test resistor (V_R) and the voltage drops over the lead wires. Therefore, the DMM measures the total resistance of the circuit (test resistor + lead wires). As the resistance of a wire depends on its length, among other factors, the measured resistance depends on the length of the wires used to perform the measurement. For resistors that are only one or two orders of magnitude larger in resistance value than the lead wires, this can have a significant influence on the precision of the measurements. This is the case for the resistors used in this work (meander and Pt100). As

mentioned at the end of the previous paragraph on the TCR, the change in resistance for a meander is around 1.5 $\Omega/°C$, which infers a measurement precision of less than $\pm 0.15 \Omega$ is required to reach a temperature sensitivity of 0.1 °C. The variance in the resistance of the lead wires is larger than this, so this technique cannot be used to perform precision resistance measurements on the resistors used in this work.
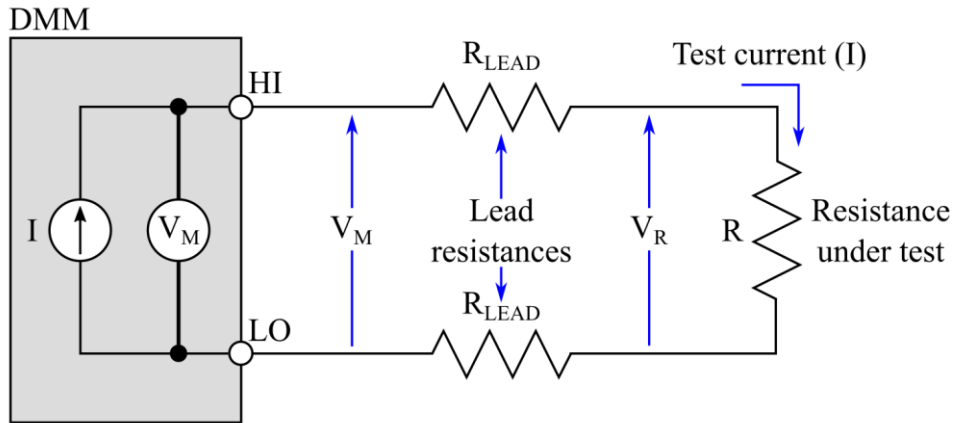
Figure 1-11 *Schematic illustration of a 2-wire resistance measurement. The test current creates a significant voltage drop over the lead resistances (R_{LEAD}), which means V_M will be higher than V_R. Therefore, the measured resistance $V_M / I = R + (2 \times R_{LEAD})$.*

To address this drawback, the 4-wire measurement technique can be used instead (**Figure 1-12**). This technique also sends a similar test current through two lead wires connected to the resistor under test. However, to measure to voltage drop over the resistor a second set of lead wires connects the voltage measurement part of the DMM close to each side of the resistor to be tested instead of the internal connection to the circuit in the 2-wire technique. Voltage measurements only require a very small sense current in the pA range. So, the voltage drop over these lead wires is negligible, which means the voltage drop measured by the DMM (V_M) can be considered equal to the voltage drop over the test resistor. Therefore, the resistance measurement becomes independent from the length of the lead wires used in the system, which allows for the required precision measurement of the resistors used in this work.
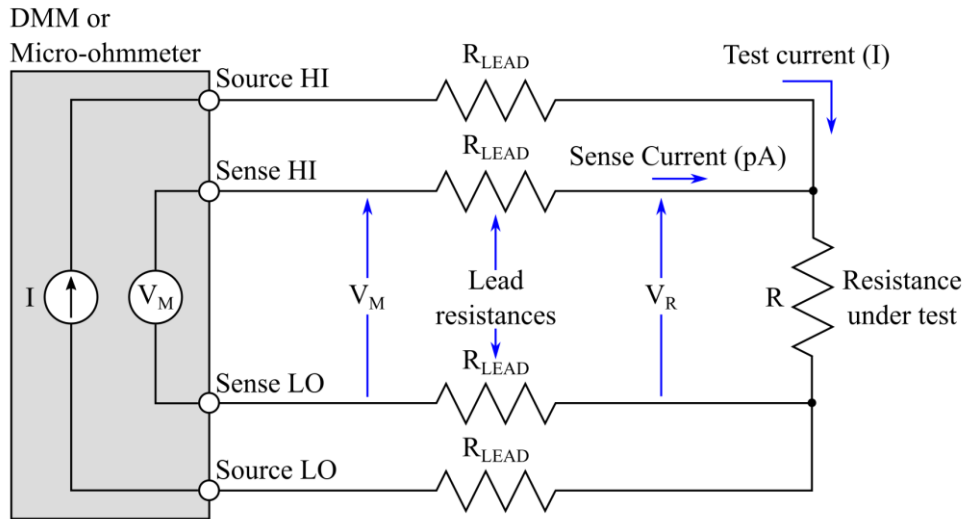
Figure 1-12 *Schematic illustration of a 4-wire resistance measurement. Because the sense current is negligible, $V_M = V_R$. This means the measured resistance $V_M / I = V_R / I$, which infers that the type and length of the lead wires no longer influence the resistance measurements.*

1.4.2 Two-Point Delta vs. Three-Point Delta Principle

In this work meander-based chips were simultaneously used as a heater and as a thermometer. In order to use these chips as a controlled heat-source the current running through them had to be fast and precisely adjustable, while still allowing precision resistance measurements to monitor their temperature. For this purpose, a square wave current was applied over the meander-based heater and the voltage was measured using the second pair of contact pads. This allowed precision resistance measurements similar to the 4-wire technique mentioned previously. However, increasing temperatures generate a changing thermoelectric voltage error (**Figure 1-13**), which increased upon each consecutive voltage measurement (100 nV in the example). In a Two-Point Delta measurement the voltage on the positive-going step of the square wave is averaged with the voltage of the negative-going step. Comparing two consecutive Two-Point Delta measurements V_a and V_b using **equations 1.4**, there is a significant difference from the actual value of 2.5 µV at the start of the measurement.

$$V_a = \frac{(V_1 - V_2)}{2} = \frac{(2.5 + x - (-2.5 + x + 0.1))}{2}\, \mu V = 2.45\ \mu V \qquad (1.4)$$

$$V_b = \frac{(V_3 - V_2)}{2} = \frac{(2.5 + x + 0.2 - (-2.5 + x + 0.1))}{2}\, \mu V = 2.55\ \mu V$$
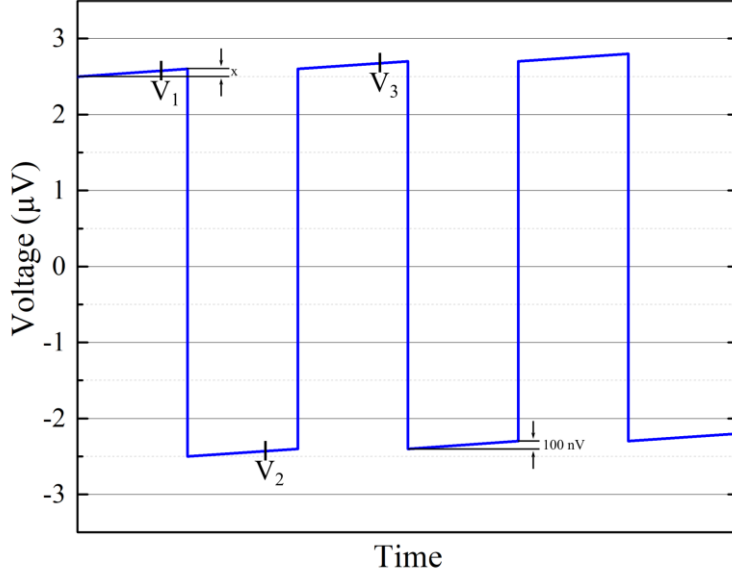
Figure 1-13 *Voltage measurements performed on a square current wave showing a changing thermoelectric voltage error.*

The thermoelectric error adds a negative error term to V_a and a positive error term to V_b. If the thermal drift is linear, these error terms are equal in magnitude so they can be cancelled out by averaging V_a and V_b giving V_f (**Equation 1.5**).

$$V_f = \frac{(V_a + V_b)}{2} = \frac{(2.45 + 2.55)}{2}\, \mu V = 2.5\ \mu V \qquad (1.5)$$

Figure 1-14 shows that by compensating for the thermoelectric error the Three-Point Delta Method has a much lower noise level compared to the Two-Point Delta Method. However, the voltages recorded over the meander-based chips used in this work during heating are in the range 0.1 - 10 V, which infers that the thermoelectric voltages (nV - µV range) are comparably

negligible and therefore do not require compensation. Even so, the Three-Point Delta Method was implemented as a forward-looking feature. More specifically, further miniaturisation could reduce the voltages over the meander during heating down to the µV range where the thermoelectric voltage errors can no longer be ignored. In which case, it allows for similarly precise temperature measurements for the meander-based heater as the 4-wire measurement technique provides for the Pt100-based thermometer.
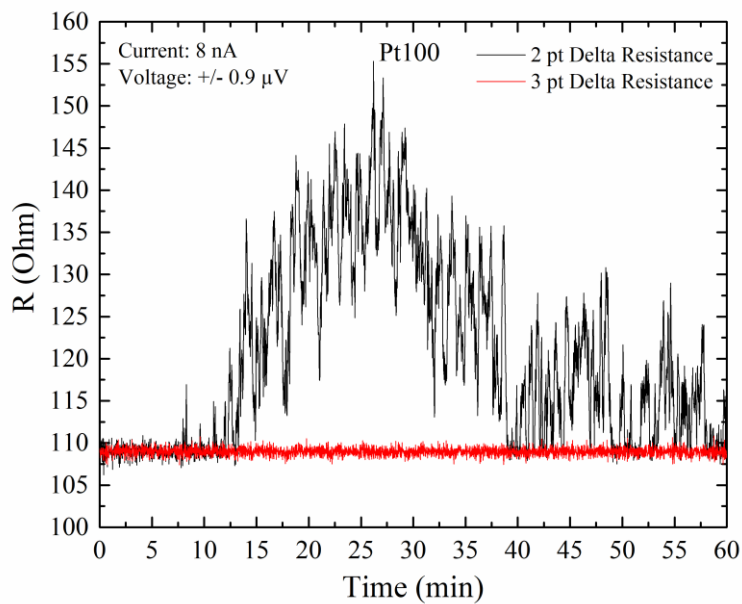
Figure 1-14 *Comparison of the Two- and Three-Point Delta method during a low-voltage measurement of a factory calibrated Pt100 resistor.*

As mentioned before, the Three-Point Delta Method depends on the linear approximation of the thermoelectric voltage error. Therefore, the measurement cycle time must be faster than the thermal time constant of the system. This requires that the current source alternates quickly in evenly timed intervals so that the thermoelectric voltage error remains equal between consecutive measurements. Moreover, the voltmeter must be tightly synchronized with the current source and be able to make accurate measurements in a short time interval. This type of

synchronization favours hardware handshaking, which is an automated negotiation process that happens before communications starts between two devices to select a mutually supported communication protocol, between the current source and the voltmeter. In this work the magnitude of the current source output must be able to change dynamically, which ruled out hardware handshaking. Therefore, software handshaking was implemented, which, although limiting the maximum frequency of the current source, proved to be more than fast enough for use in this work.

References

[1]   P. Mehrotra, Biosensors and their applications – A review, *Journal of Oral Biology and Craniofacial Research* **6** (2), 153-159 (2016).

[2]   G. Rocchitta, A. Spanu, S. Babudieri, G. Latte, G. Madeddu, G. Galleri, S. Nuvoli, P. Bagella, M. I. Demartis, V. Fiore, R. Manetti and P. A. Serra, Enzyme biosensors for biomedical applications: Strategies for safeguarding analytical performances in biological fluids, *Sensors (Basel)* **16** (6), 780 (2016).

[3]   P. Bollella and L. Gorton, Enzyme based amperometric biosensors, *Current Opinion in Electrochemistry* **10**, 157-173 (2018).

[4]   A. Juste, B. Lievens, I. Frans, M. Klingeberg, C. W. Michiels and K. A. Willems, Development of a DNA array for the simultaneous detection and identification of sugar thick juice bacterial contaminants, *Food Analytical Methods* **4** (2), 173-185 (2011).

[5]   F. L. Dickert, Biomimetic receptors and sensors, *Sensors (Basel)* **14** (12), 22525-22531 (2014).

[6]   A. N. Kozitsina, T. S. Svalova, N. N. Malysheva, A. V. Okhokhonin, M. B. Vidrevich and K. Z. Brainina, Sensors based on bio and biomimetic receptors in medical diagnostic, environment, and food analysis, *Biosensors (Basel)* **8** (2), 35 (2018).

[7]   K. Eersels, H. Diliën, J. W. Lowdon, E. Steen Redeker, R. Rogosic, B. Heidt, M. Peeters, P. Cornelis, P. Lux, C. P. Reutelingsperger, L. J. Schurgers, T. J. Cleij and B. van Grinsven, A novel biomimetic tool for assessing vitamin K status based on molecularly imprinted polymers, *Nutrients* **10** (6), 751 (2018).

[8]   B. van Grinsven, K. Eersels, S. Erkens-Hulshof, H. Diliën, K. Nurekeyeva, P. Cornelis, D. Klein, F. Crijns, G. Tuijthof, P. Wagner, E. Steen Redeker and T. J. Cleij, SIP-based thermal detection platform for the direct detection of bacteria obtained from a contaminated surface, *Physica Status Solidi a-Applications and Materials Science* **215** (15), 1700777 (2018).

[9]   H. Diliën, M. Peeters, J. Royakkers, J. Harings, P. Cornelis, P. Wagner, E. Steen Redeker, C. E. Banks, K. Eersels, B. van Grinsven and T. J. Cleij, Label-free detection of small organic molecules by molecularly imprinted polymer functionalized thermocouples: Toward in vivo applications, *ACS Sensors* **2** (4), 583-589 (2017).

[10]   E. Steen Redeker, K. Eersels, O. Akkermans, J. Royakkers, S. Dyson, K. Nurekeyeva, B. Ferrando, P. Cornelis, M. Peeters, P. Wagner, H. Diliën, B. van Grinsven and T. J. Cleij, Biomimetic bacterial identification platform based on Thermal Wave Transport Analysis (TWTA) through surface-imprinted polymers, *ACS Infectious Diseases* **3** (5), 388-397 (2017).

[11] W. Stilman, S. Jooken, G. Wackers, P. Cornelis, M. Khorshid, D. Yongabi, O. Akkermans, S. Dyson, B. van Grinsven, T. Cleij, L. van Ijzendoorn, P. Wagner and K. Eersels, Optimization and characterization of a flow cell for heat-transfer-based biosensing, *Physica Status Solidi a-Applications and Materials Science* **214** (9), 1600758 (2017).

[12] A. K. Deisingh, Aptamer-based biosensors: Biomedical applications, *Handbook of Experimental Pharmacology* (173), 341-357 (2006).

[13] W. Zhang, Q. X. Liu, Z. H. Guo and J. S. Lin, Practical application of aptamer-based biosensors in detection of low molecular weight pollutants in water sources, *Molecules* **23** (2), 344 (2018).

[14] S. Sharma, H. Byrne and R. J. O'Kennedy, Antibodies and antibody-derived analytical biosensors, *Essays in Biochemistry* **60** (1), 9-18 (2016).

[15] J. Kang, S. Kim and Y. Kwon, Antibody-based biosensors for environmental monitoring, *Toxicology and Environmental Health Sciences* **1** (3), 145-150 (2009).

[16] G. Vasapollo, R. D. Sole, L. Mergola, M. R. Lazzoi, A. Scardino, S. Scorrano and G. Mele, Molecularly imprinted polymers: present and future prospective, *International Journal of Molecular Sciences* **12** (9), 5908-5945 (2011).

[17] F. A. Trikka, K. Yoshimatsu, L. Ye and D. A. Kyriakidis, Molecularly imprinted polymers for histamine recognition in aqueous environment, *Amino Acids* **43** (5), 2113-2124 (2012).

[18] M. Akhoundian, A. Ruter and S. Shinde, Ultratrace detection of histamine using a molecularly-imprinted polymer-based voltammetric sensor, *Sensors* **17** (3), 645 (2017).

[19] H. R. Culver and N. A. Peppas, Protein-imprinted polymers: The shape of things to come?, *Chemistry of Materials* **29** (14), 5753-5761 (2017).

[20] M. Dabrowski, P. Lach, M. Cieplak and W. Kutner, Nanostructured molecularly imprinted polymers for protein chemosensing, *Biosensors and Bioelectronics* **102**, 17-26 (2018).

[21] J. Erdőssy, V. Horváth, A. Yarman, F. W. Scheller and R. E. Gyurcsányi, Electrosynthesized molecularly imprinted polymers for protein recognition, *TrAC Trends in Analytical Chemistry* **79**, 179-190 (2016).

[22] O. Hayden and F. L. Dickert, Selective microorganism detection with cell surface imprinted polymers, *Advanced Materials* **13** (19), 1480-1483 (2001).

[23] B.-Y. Chang and S.-M. Park, Electrochemical impedance spectroscopy, *Annual Review of Analytical Chemistry* **3** (1), 207-229 (2010).

[24] B. van Grinsven, K. Eersels, M. Peeters, P. Losada-Pérez, T. Vandenryt, T. J. Cleij and P. Wagner, The heat-transfer method: A versatile low-cost, label-free, fast, and user-friendly readout platform for biosensor applications, *ACS Applied Materials & Interfaces* **6** (16), 13309-13318 (2014).

[25] J. J. Giner-Sanz, E. M. Ortega, M. Garcia-Gabaldon and V. Perez-Herranz, Theoretical determination of the stabilization time in galvanostatic EIS measurements: The simplified Randles cell, *Journal of the Electrochemical Society* **165** (13), E628-E636 (2018).

[26] T. Q. Nguyen and C. Breitkopf, Determination of diffusion coefficients using impedance spectroscopy data, *Journal of the Electrochemical Society* **165** (14), E826-E831 (2018).

[27] J. Huang, Diffusion impedance of electroactive materials, electrolytic solutions and porous electrodes: Warburg impedance and beyond, *Electrochimica Acta* **281**, 170-188 (2018).

[28] R. A. D. de Faria, L. G. D. Heneine, T. Matencio and Y. Messaddeq, Faradaic and non-faradaic electrochemical impedance spectroscopy as transduction techniques for sensing applications, *International Journal of Biosensors & Bioelectronics* **5** (1), 29–31 (2019).

[29] R. E. Ionescu, C. Gondran, L. Bouffier, N. Jaffrezic-Renault, C. Martelet and S. Cosnier, Label-free impedimetric immunosensor for sensitive detection of atrazine, *Electrochimica Acta* **55** (21), 6228-6232 (2010).

[30] E. Katz and I. Willner, Probing biomolecular interactions at conductive and semiconductive surfaces by impedance spectroscopy: Routes to impedimetric immunosensors, DNA-Sensors, and enzyme biosensors, *Electroanalysis* **15** (11), 913-947 (2003).

[31] S. H. Wright, Generation of resting membrane potential, *Advances in Physiology Education* **28** (4), 139-142 (2004).

[32] P. L. Kapitza, Heat transfer and superfluidity of helium II, *Physical Review* **60** (4), 354-355 (1941).

[33] G. L. Pollack, Kapitza resistance, *Reviews of Modern Physics* **41** (1), 48-81 (1969).

[34] E. T. Swartz and R. O. Pohl, Thermal boundary resistance, *Reviews of Modern Physics* **61** (3), 605-668 (1989).

[35] B. van Grinsven, N. Vanden Bon, H. Strauven, L. Grieten, M. Murib, K. L. Monroy, S. D. Janssens, K. Haenen, M. J. Schöning, V. Vermeeren, M. Ameloot, L. Michiels, R. Thoelen, W. De Ceuninck and P. Wagner, Heat-transfer resistance at solid-liquid interfaces: A tool for the detection of single-nucleotide polymorphisms in DNA, *ACS Nano* **6** (3), 2712-2721 (2012).

[36]   M. Lenz, U. Striedl and Fröhler, SMD Packages. Thermal resistance, theory and practice, *Released by Infineon Technologies AG, Munich, Germany*, (2000).

[37]   M. Peeters, S. Kobben, K. L. Jiménez-Monroy, L. Modesto, M. Kraus, T. Vandenryt, A. Gaulke, B. van Grinsven, S. Ingebrandt, T. Junkers and P. Wagner, Thermal detection of histamine with a graphene oxide based molecularly imprinted polymer platform prepared by reversible addition–fragmentation chain transfer polymerization, *Sensors & Actuators B: Chemical* **203**, 527-535 (2014).

[38]   M. Peeters, P. Csipai, B. Geerets, A. Weustenraed, B. van Grinsven, R. Thoelen, J. Gruber, W. De Ceuninck, T. J. Cleij, F. J. Troost and P. Wagner, Heat-transfer-based detection of L-nicotine, histamine, and serotonin using molecularly imprinted polymers as biomimetic receptors, *Analytical and Bioanalytical Chemistry* **405** (20), 6453-6460 (2013).

[39]   M. Peeters, B. van Grinsven, T. J. Cleij, K. L. Jiménez-Monroy, P. Cornelis, E. Pérez-Ruiz, G. Wackers, R. Thoelen, W. De Ceuninck, J. Lammertyn and P. Wagner, Label-free protein detection based on the heat-transfer method--A case study with the peanut allergen Ara h 1 and aptamer-based synthetic receptors, *ACS Applied Materials & Interfaces* **7** (19), 10316-10323 (2015).

[40]   K. Eersels, B. van Grinsven, A. Ethirajan, S. Timmermans, K. L. Jiménez Monroy, J. F. Bogie, S. Punniyakoti, T. Vandenryt, J. J. Hendriks, T. J. Cleij, M. J. Daemen, V. Somers, W. De Ceuninck and P. Wagner, Selective identification of macrophages and cancer cells based on thermal transport through surface-imprinted polymer layers, *ACS Applied Materials & Interfaces* **5** (15), 7258-7267 (2013).

[41]   B. van Grinsven, K. Eersels, O. Akkermans, S. Ellermann, A. Kordek, M. Peeters, O. Deschaume, C. Bartic, H. Diliën, E. Steen Redeker, P. Wagner and T. J. Cleij, Label-free detection of *Escherichia coli* based on thermal transport through surface imprinted polymers, *ACS Sensors* **1** (9), 1140-1147 (2016).

[42]   K. Betlem, S. Hoksbergen, N. Mansouri, M. Down, P. Losada-Pérez, K. Eersels, B. van Grinsven, T. J. Cleij, P. Kelly, D. Sawtell, M. Zubko, C. Banks and M. Peeters, Real-time analysis of microbial growth by means of the Heat-Transfer Method (HTM) using *Saccharomyces cerevisiae* as model organism, *Physics in Medicine* **6**, 1-8 (2018).

[43]   P. Losada-Pérez, K. L. Jiménez-Monroy, B. van Grinsven, J. Leys, S. D. Janssens, M. Peeters, C. Glorieux, J. Thoen, K. Haenen, W. D. Ceuninck and P. Wagner, Phase transitions in lipid vesicles detected by a complementary set of methods heat-transfer measurements, adiabatic scanning calorimetry, and dissipation-mode quartz crystal microbalance, *Physica Status Solidi (a)* **211** (6), 1377-1388 (2014).

[44]   E. L. Decker, B. Frank, Y. Suo and S. Garoff, Physics of contact angle measurement, *Colloids and Surfaces A: Physicochemical and Engineering Aspects* **156** (1-3), 177-189 (1999).

[45] D. Yongabi, M. Khorshid, P. Losada-Pérez, K. Eersels, O. Deschaume, J. D'Haen, C. Bartic, J. Hooyberghs, R. Thoelen, M. Wübbenhorst and P. Wagner, Cell detection by surface imprinted polymers SIPs: A study to unravel the recognition mechanisms, *Sensors and Actuators B: Chemical* **255**, 907-917 (2018).

[46] M. J. Sanderson, I. Smith, I. Parker and M. D. Bootman, Fluorescence microscopy, *Cold Spring Harbor Protocols* **2014** (10), 1042-1065 (2014).

[47] M. H. W. Stopel, C. Blum and V. Subramaniam, Excitation spectra and stokes shift measurements of single organic dyes at room temperature, *Journal of Physical Chemistry Letters* **5** (18), 3259-3264 (2014).

[48] E. Balleza, J. M. Kim and P. Cluzel, Systematic characterization of maturation time of fluorescent proteins in living cells, *Nature Methods* **15** (1), 47-51 (2018).

[49] S. Thiberge, A. Nechushtan, D. Sprinzak, O. Gileadi, V. Behar, O. Zik, Y. Chowers, S. Michaeli, J. Schlessinger and E. Moses, Scanning electron microscopy of cells and tissues under fully hydrated conditions, *Proceedings of the National Academy of Sciences of the United States of America* **101** (10), 3346-3351 (2004).

[50] F. J. Giessibl, Advances in atomic force microscopy, *Reviews of Modern Physics* **75** (3), 949-983 (2003).

[51] M. L. Zhang and D. A. Drabold, Theory of temperature coefficient of resistivity: Application to amorphous Si and Ge, *EPL* **98** (1), 17005 (2012).

[52] Engineering Toolbox: https://www.engineeringtoolbox.com/conductors-d_1381.html: data retrieved on October 16, 2018.

[53] Resistor Guide: http://www.resistorguide.com/temperature-coefficient-of-resistance/: data retrieved on October 10, 2016.

Chapter 2: A Novel Modular Device for Biological Impedance Measurements - The Differential Impedimetric Sensor Cell (DISC)

Authors: ***Peter Cornelis***, *Gideon Wackers, Isabelle Thomas, Max Brand, Tristan Putzeys,*

Alessia Gennaro, Michael Wübbenhorst, Sven Ingebrandt and Patrick Wagner.

Scientific contribution: *Design and assembly of the devices, design of experiments, data analysis,*

software development, writing the manuscript (corresponding author)

Highlights

- Simultaneous detection and quantification of multiple target molecules

- Low-cost device capable of both faradaic and non-faradaic impedance spectroscopy

- Validated against a high-resolution dielectric spectrophotometer (10 Hz - 100 kHz)

Abstract

For medical diagnostics, food-safety analysis and detection of environmental pollutants, simultaneous detection and quantification of multiple target molecules would be a great advantage. Impedimetric measurements using molecularly imprinted polymers (MIPs), antibodies or aptamers as biomimetic sensors are becoming a well-established technique for detecting, quantifying and analyzing various biological targets such as DNA, proteins and small molecules. The most commonly implemented systems use non-faradaic impedance spectroscopy. Adding a redox probe, such as silver/silver chloride, as a reference electrode besides the standard working and counter electrodes allows for the use of faradaic impedance spectroscopy techniques using redox-active molecules such as ferricyanide, thereby extending the range of possible applications through increased sensitivity of the measurements. Furthermore, the ability to perform differential measurements would allow the use of undiluted patient samples, which significantly simplifies sample preparation. Therefore, adapting this low-cost technique to simultaneously perform differential measurements on multiple targets and making it easy to use has great potential in a wide range of applications. In this work, a system that meets these requirements has been successfully designed and fabricated. Up to eight different targets can be quasi-simultaneously analyzed. Furthermore, the system was validated against a high-resolution dielectric spectrometer (Novocontrol, Alpha analyzer) using well characterized samples at different temperatures over the frequency range 10 Hz – 100 kHz.

2.1 Introduction

Impedimetric measurements using biosensors are becoming well-established as evidenced in multiple review articles[1-4]. This technique has a broad variety of applications as the following examples demonstrate: DNA detection and analysis[5-7], monitoring cell viability

using interdigitated electrodes[8], characterizing self-assembled monolayers[9] and detecting and quantifying proteins using sensors functionalized with antibodies[10] or aptamers[11]. Furthermore, even small molecules can be detected and quantified in the nano-molar range using antibodies[12] or molecularly imprinted polymers (MIPS)[13-15]. Performing differential measurements, where the response of a functionalized and a non-functionalized (reference) sensor are compared, allows analysis of undiluted patient samples. Ideally, both measurements should be done simultaneously on the same sample. Impedimetric measurement techniques are also widely used in medical applications such as body fluid volume measurements and tracking of changes in the body cell mass[16-18]. For medical, food-safety and environmental applications, simultaneous measurement of multiple target molecules would be a great advantage. For instance, the presence of cadaverine dramatically increases the toxicity of histamine found in spoiled food[19, 20]. All the previously mentioned applications use non-faradaic impedance spectroscopy, which does not use redox probes. Faradaic impedance spectroscopy allows measurement of redox-active molecules by using a (pseudo) reference electrode in addition to the standard working and counter electrode[21, 22]. This technique has even lower detection limits, below 1 nM, but requires the use of auxiliary chemicals[21]. The novel modular device that was developed in this work enables up to eight measurement channels in any combination of functionalized and non-functionalized biosensor chips. Moreover, both non-faradaic and faradaic impedance spectroscopy techniques can be employed.

2.2 Materials and Fabrication

The device consists of two main subassemblies: The "Differential impedimetric sensor cell" and its controller, the "Electronic base unit" or respectively DISC and EBU for short. Polyether ether ketone (PEEK) has been used to fabricate several of the components inside the

DISC. This material is thermally and chemically stabile and, most importantly, easily sterilizable.

2.2.1 Differential Impedimetric Sensor Cell (DISC)

The core component is the flow cell shown in **Figure 2-1**. The fluid compartment has an internal volume of 310 µl. At its center, traversing the entire cell, a gold wire is attached, which serves as the counter electrode for the impedance measurements. Also, two small ports are present respectively at the bottom and the top allowing an easy exchange of fluids. To counteract the formation of air bubbles, concave recesses at the inlet and outlet of the flow cell are used as transitional structures. Liquid is injected at the bottom and leaves at the top. A thermocouple is present in the bottom recess to monitor the liquid temperature.
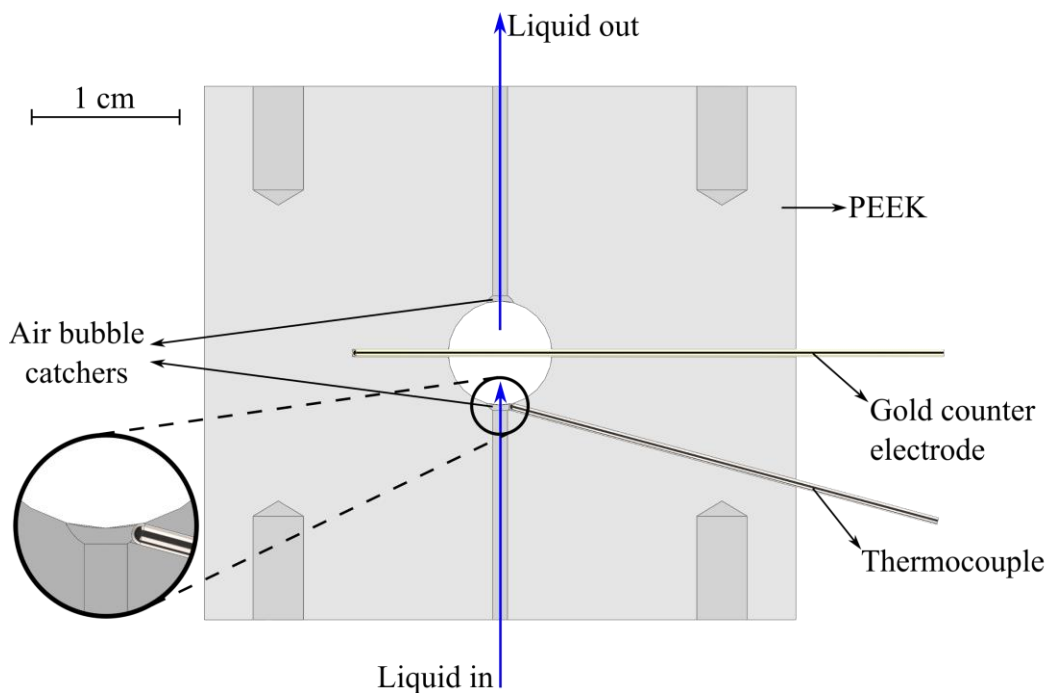
Figure 2-1 *Schematic illustration of the flow cell. The gold counter electrode is used for impedance measurements while the thermocouple is used to monitor the temperature of the liquid. Where the liquid enters/leaves the flow cell concave recesses are present to capture and remove air bubbles from the system.*

Two chip-holder modules, each containing a sensor chip, are positioned on the left and right side of the flow cell. For this, two different module versions have been designed (**Figure 2-2**): A basic module, for single channel sensors with an active surface area that covers the entire area exposed to the flow cell, and an advanced module that can accommodate 1- to 4-channel sensors for which the active surface area is distributed among the required number of channels. Each module version incorporates a viton® O-ring for a perfect leak-free seal with the flow cell.
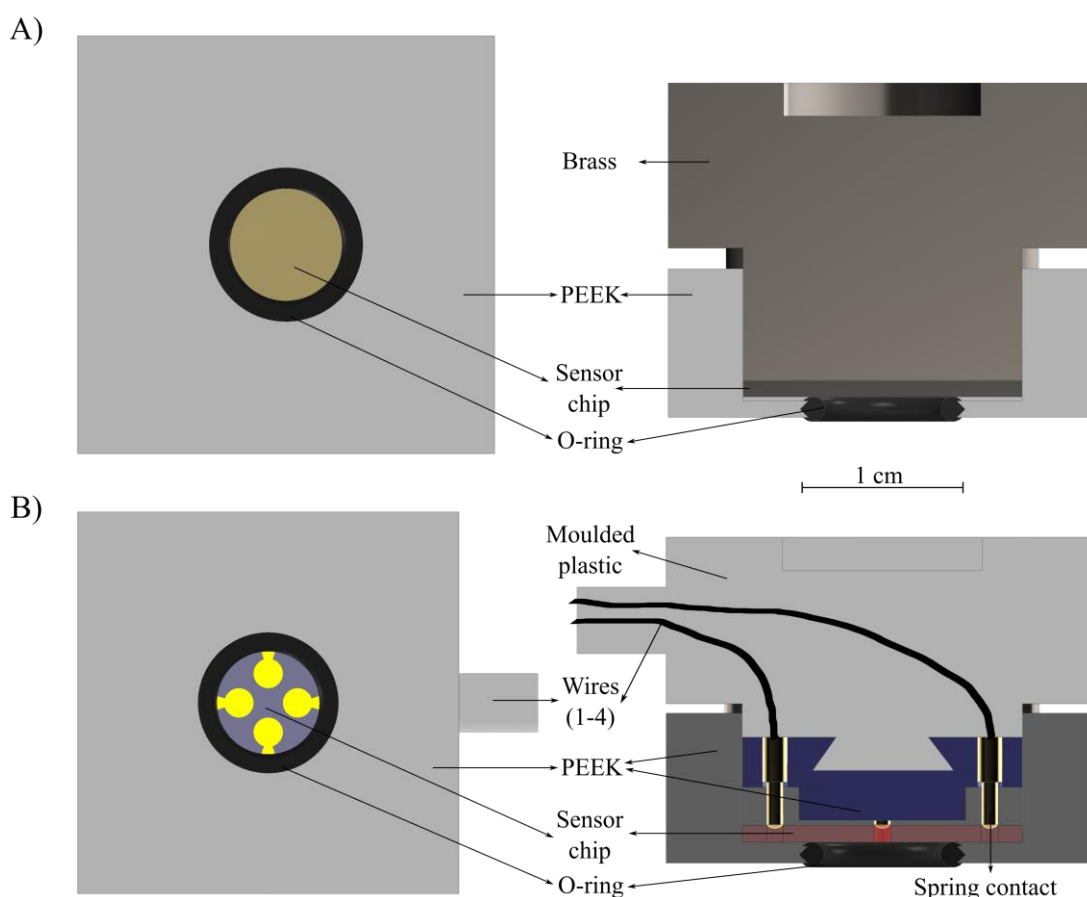
Figure 2-2 *Schematic illustration and cross-section of the basic (A) and advanced (B) chip-holder module.The basic module uses the whole sensor chip as the measurement (working) electrode while in the advanced module spring-loaded contacts are used to connect up to four separate working electrodes on a single sensor chip.*

The complete measuring unit incorporates two of these modules (**Figure 2-3**). A large screw is used to achieve a good seal by fastening the O-ring between the flow cell and the modules and allows also for a fine-grained control over the distance between the sensor chips in the modules and the gold wire in the flow cell thanks to the compressibility of the O-ring. The vertical placement of the electrodes inside the modules has the advantage that larger particles inside complex samples cannot sediment onto their surface.
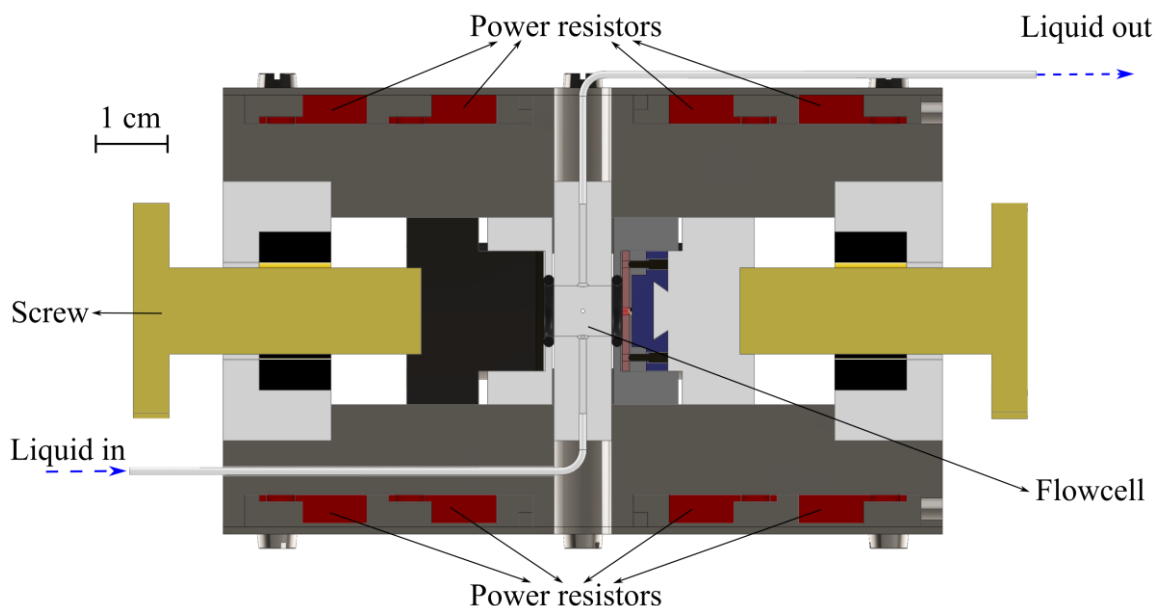
Figure 2-3 Schematic illustration of a cross section through the temperature-controlled measurement unit.Power resistors are used for a homogeneous temperature distribution and pre-heating the incoming liquid. The screws allow fine tuning the distance between the sensor chips and the gold counter electrode.

The impedance of an electrolyte depends on its temperature and measurement frequency[23]. Therefore, a stable and tightly controlled temperature is very important for impedimetric measurements where the sensor needs to detect a change in impedance caused by the presence of its bio-molecular targets. Two large heater elements, one below and one on top of the flow

cell, not only allow precise control over the temperature of the flow cell but also the injected liquid by routing the injection tubing through the bottom heater element as shown in **Figure 2-3**. Each heater consists of four 10 Ω power resistors in series encased in an aluminum block, which has a suitably placed hole for a thermocouple to monitor its temperature. A small T-junction can be placed at the back of the top heating element allowing a silver/silver chloride redox probe to be inserted into the outgoing liquid stream as a reference electrode for use in faradaic impedance measurements[24]. Finally, to minimize the influence of electro-magnetic noise and thermal convection effects caused by air turbulence that may be present in the environment, the whole measurement unit is located inside an aluminum box, with a lid for easy access as shown in **Figure 2-4**.
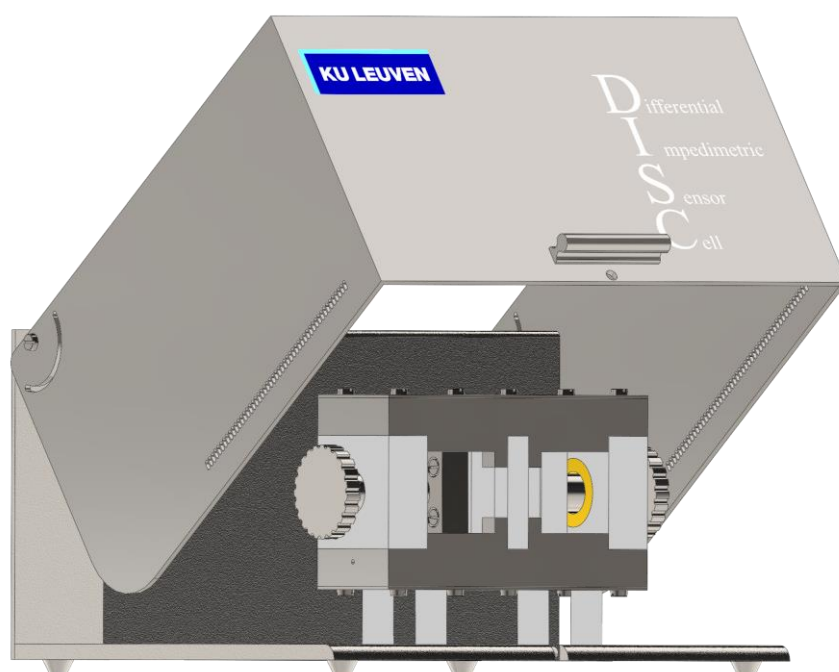
Figure 2-4 *Schematic illustration of the DISC. The metal cover provides a stable thermal environment while also acting as a Faraday cage to reduce electromagnetic noise from the environment.*

During measurements, this box acts as a Faraday cage reducing the electro-magnetic noise. The small holes at the bottom of the lid allow for a slow non-turbulent airflow and therefore heat exchange with the environment, ensuring proper operation of the heater elements. All electrical, thermocouple and liquid tubing (Teflon, 1 mm outside ⌀, 0.5 mm inside ⌀) connections were built into a panel at the back of the box for ease of use. This also ensures a clear separation between the liquid and the electronics to minimize the risk of short-circuits within the system.

2.2.2 Electronic Base Unit (EBU)

Like the DISC, this is a mainly custom-made device (**Figure 2-5**). It is connected via USB to a computer running an in-house written LabView program, which does a basic pre-processing of the measurement data allowing easier analysis of the data at a later stage. The program also includes PID (proportional–integral–derivative) based temperature controllers for the heater elements of the DISC to keep them at a constant temperature. Moreover, it provides an easy to navigate user interface to set up and run experiments. Inside the EBU, two 4-port micro USB hubs are used to connect all internal components and to add two additional external

Figure 2-5 *Picture of the assembled electronic base unit (EBU).*

USB ports at the back for additional devices. In this case, they serve to control syringe pumps automating the exchange of fluids in the flow cell. The internal components comprise a PowerDAC, a temperature measurement device, an impedimetric device and their supporting electronic components.

2.2.2.1 PowerDAC

This device is essentially a precisely controlled dual channel voltage source with each channel capable of delivering up to 50 W in power (**Figure 2-6**). Connected to the power resistors inside heating elements it can be used as a controllable heat source. All active components are connected through an I²C-bus. The FT232B-SC18IM700 chip combination enables USB communication with these components. The maximum voltage can be set to 5, 10, 25 or 50 V for each channel separately. The supply voltage of the PowerDAC needs to be at least 10 % higher than the highest selected maximum voltage.

Figure 2-6 *Schematic representation of the main components and interconnections of the PowerDAC device(inset: Photograph with scale bar).*

The requested output voltage is achieved using a 2-stage process: In the first step, a digital to analogue (D/A) converter (LTC2606) combined with an operational amplifier (OP07CP) produces a voltage in the range 0 - 5 V. Finally, a second operational amplifier (ADA4700-1) increases this voltage to the user-requested value. A set of three relays (G6K-2FY) controlled by a general purpose I/O-chip (PCA9535) determine the amplification factor in this second stage. Choices are 1 ×, 2 ×, 5 × and 10 × corresponding to the maximum voltages mentioned above. This flexibility in setting the maximum output voltage enables use of this device in low power applications where the maximum power delivered to the system needs to be restricted. Another advantage of using a 2-stage process is the possibility to monitor the actual output voltage during the measurements. To this end, an analogue to digital (A/D) converter (ADS1110) was placed between both stages.

2.2.2.2 Temperature Measurements

For this purpose, the National Instruments NI-9212 thermocouple card was selected. It offers 8 channel-to-channel isolated thermocouple inputs, cold-junction compensation and fast read-outs of all channels simultaneously. Type K is the most common general-purpose thermocouple. It is inexpensive and its temperature range (0 °C to 1100 °C) and sensitivity (± 0.15 °C at 37 °C) are more than sufficient as the relevant temperature for biosensor measurements ranges from room temperature up to the denaturation temperature of DNA at around 90 °C. Thermocouples of type K with a diameter of 500 µm were purchased from TC Direct (The Netherlands).

2.2.2.3 Dual Reference Organic Impedimetric Device (DROID)

Similar to the PowerDAC, all the active components are interconnected via an I²C-bus and the FT232B-SC18IM700 chip combination enables USB communication. However, unlike the PowerDAC, this device is completely USB-powered just as the NI-9212 mentioned in section 2.2.2.2. **Figure 2-7** shows a schematic representation of its main components: The core

component is the AD5933 impedance analyzer, which has already proven itself in custom impedimetric designs[25, 26]. Its output voltage can be set to four distinct levels (200 mV, 400 mV, 1.0 V and 2.0 V). For biological (organic) samples, the voltage between the sample and the counter electrode should not exceed 70 mV[27]. Therefore, an adjustable voltage divider was added at the V_{out}-pin to reduce the output from 2 V to 65 mV. This allows lower settings to be programmatically enabled in case of very sensitive biological samples. Using its internal oscillator, the AD5933 has a frequency measurement range between 1 kHz and 100 kHz. To extend the lower limit to 10 Hz an external oscillator (DS1077) was added to the system.

For calibration purposes, a set of ten reference resistors ranging between 39 Ω and 3.9 MΩ were added to the device. During calibration, the phase-shift and impedance for the requested measurement frequencies is individually measured for each of these resistors and stored in a calibration file to be used during the actual biosensing measurements. To select the appropriate feedback-, measurement- and/or reference channel, two general purpose I/O-chips (PCA9535) drive twenty-four relays (**inset Figure 2-7**). The LabView software calculates the phase shift and impedance amplitudes from the real and imaginary values it receives from the AD5933 and adjusts these using the calibration data.
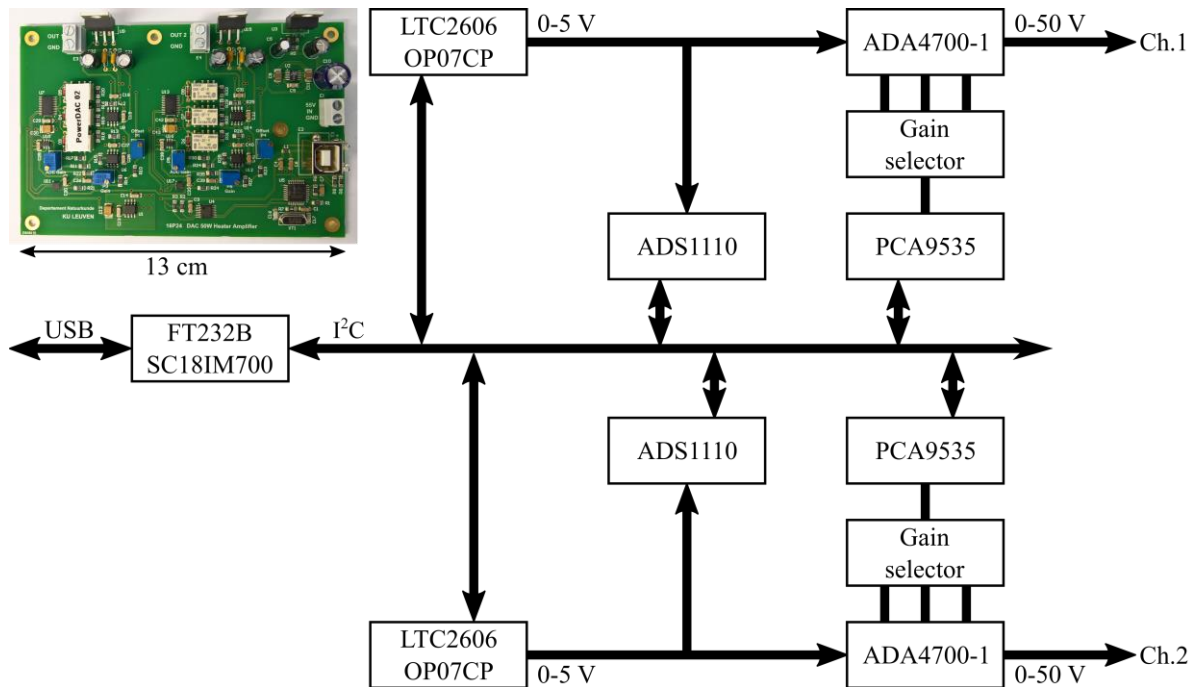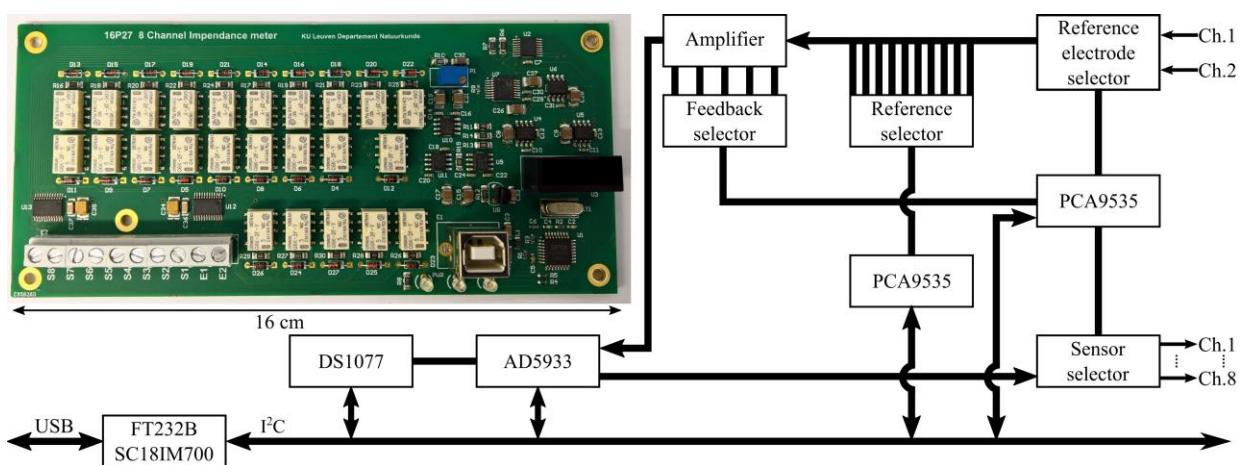

Figure 2-7 *Schematic representation of the main components and interconnections of the DROID device(inset: Photograph with scale bar).*

2.2.3 Final assembly

The basic system consists of the DISC, the EBU and a computer running the measurement software. Optionally, any kind of USB-connectable liquid pumping system such as peristaltic or syringe-driven pumps can be attached to the EBU to simplify connections.

2.3 Device characterization

Several control experiments were performed to determine the main device characteristics of the DISC. Based on previous experience the same PID parameters were used for both temperature controllers (P = 1, I = 8, D = 0). As can be seen from the heater profile T_H in **Figure 2-9** (Paragraph 2.4) there was no need for further optimization of these parameters, so they remained unchanged for all subsequent experiments. Furthermore, all measurements were carried out under no-flow conditions of the liquid inside the flow cell.

2.3.1 Materials

Chips measuring 10×10 mm² were cut from a 0.5 mm thick aluminum sheet (Brico N.V., Leuven, Belgium). Polystyrene (Mw = 932 kDa), and anhydrous toluene (99.8%) were purchased from Sigma-Aldrich (Diegem, Belgium). Phosphate buffer saline (PBS) solution with pH 7.4 was prepared using NaCl, Na_2HPO_4, and KH_2PO_4, also purchased from Sigma-Aldrich (Diegem, Belgium).

2.3.2 Sensor Chips

Smooth aluminum substrates were covered with a thin polystyrene layer. Compared to gold-coated chips, aluminum chips are low-cost while having a similarly high electrical and thermal conductivity. They are also natively covered with a thin protective oxide layer that is stable at neutral pH values[28, 29]. Moreover, they have been tested before using polymers as a model system for biological layers and/or as an adhesive layer to attach MIPs[13-15]. To

manufacture these chips, 8 mg of polystyrene was dissolved in 5 ml toluene. This solution was then left to cure while stirring at 80 °C under nitrogen atmosphere for 60 minutes before spin-coating it onto the aluminum substrates (60 s at 3000 rpm). Finally, the substrates were stored at 80 °C under nitrogen atmosphere for 18 hours to completely cure the polystyrene. A layer thickness of 91 ± 7 nm was measured using an Agilent 5500 AFM system with NCSTR probes (spring constant 7.4 N/m, resonant frequency 160 kHz, tip radius of curvature < 7 nm) purchased from NanoAndMore GmBH, Germany for morphological imaging in intermittent contact (AAC) mode. The AFM topography images were levelled, line-corrected and analyzed (height profiles) using Gwyddion, a free and open-source SPM (scanning probe microscopy) data visualization and analysis program[30].

2.3.3 Heating Characteristics

After installing two identical sensor chips, the flow cell of the system was filled with a $1 \times$ PBS solution. This PBS solution was chosen because it has similar salt concentrations, conductivity and pH value as typical biological samples like blood plasma. A stepped temperature profile for the heater elements was programmed into the system (25 °C, 30 °C, 35 °C, 37 °C, 40 °C and 50 °C) with each step lasting 2 hours. All temperatures and voltages were calculated by averaging the measurement over a 10-minute period starting 90 minutes after the start of each step. The required power P was calculated using **Equation 2.1** with R the resistance of one heater element and V the voltage applied to the respective heater elements.

$$P = \frac{V_{\text{heater bottom}}^2 + V_{\text{heater top}}^2}{R} \tag{2.1}$$

The results of these experiments were used to determine the temperature profile of the liquid inside the flow cell as well as the correlation between the temperature of the two heating elements and the resulting temperature inside the flow cell.

2.3.4 Impedance Characteristics

Similar to the experiments performed to study the heating characteristics, two identical sensor chips were installed, and the flow cell filled with a $1 \times$ PBS solution. Using **Equation 2.2**, which will be discussed in more detail in section 2.4, a stepped temperature profile was created and programmed into the system to set and stabilize the temperature of the liquid inside the flow cell at specific values (25 °C, 30 °C, 35 °C, 37 °C, 40 °C, 45 °C and 50 °C). Each step lasted 1 hour, during which the impedance measurement channels were disconnected from the EBU after 45 minutes and connected to a high-resolution dielectric spectrometer (Novocontrol, Alpha analyzer). After two measurement cycles the DISC was reconnected to the EBU. Impedance measurements were performed in the frequency range 10 Hz to 100 kHz with 10 logarithmically equidistant points per decade. For both devices the results were averaged over three measurement cycles and the final results were then compared. To correlate the physical elements (such as the conductivity of the liquid and the interface capacitance of the double-layer) with the elements from the equivalent circuit, which represents a mathematical model of the impedimetric biosensor system, two clean aluminum sensor chips were installed, and the flow cell filled with a PBS solution. Three individual experiments were run at room temperature, with respectively a $0.1 \times$, $1 \times$, and $10 \times$ PBS solution, to evaluate the effect of the ionic strength of the liquid inside the flow cell on the measurements. During each experiment, six frequency sweeps from 10 Hz to 100 kHz, with 10 logarithmically equidistant points per decade, were performed and their results averaged.

2.4 Results and Discussion

The results displayed in **Figure 2-8** show a clear linear correlation between the temperature of the heating elements and the temperature of the liquid inside the flow cell

(**Equation 2.2**). In the equation, the heater (T_H) and flow cell temperature (T_C) are in Kelvin units as opposed to °C units in the figure.

$$T_H = 1.223 \cdot T_C - 66.3 \text{ K} \qquad (R^2 = 0.999) \qquad (2.2)$$

Based on this equation a temperature profile for the heater elements can be calculated to precisely control the liquid temperature inside the flow cell. **Equation 2.3** was constructed to fit the power values in **Figure 2-8**. The linear contribution is related to heat conduction and convection while the 4th order contribution relates to heat loss through radiation according to the law of Stefan-Boltzmann[31]. The small correction factor is presumably necessary because the aluminum enclosure of the DISC device, see **Figure 2-4**, acts as a radiation shield. The flow cell temperature (T_C) and ambient temperature (T_A) are in Kelvin units.

$$P = 0.037 \frac{W}{K} \cdot (T_C - T_A) + 1.7 \cdot 10^{-9} \frac{W}{K^4} \cdot (T_C^4 - T_A^4) - 0.56 \text{ W} \qquad (R^2 = 0.997) \quad (2.3)$$
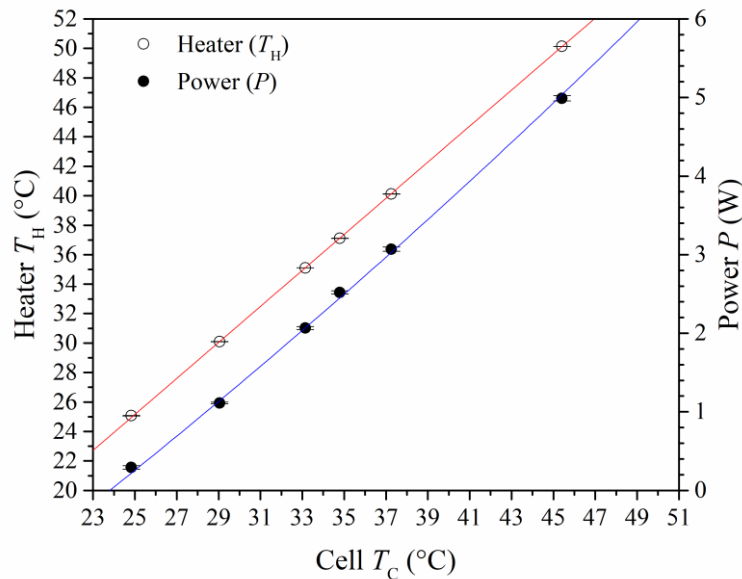
Figure 2-8 *Required heater temperature (open circles) and power (closed circles) as a function of the chosen liquid temperature inside the flow cell.Linear fit (**Equation 2.2**) for the heater temperature (red line). Power fit based on **Equation 2.3** (blue line). Error bars were calculated by averaging measurements over a 10-minute period.*

The measured data plotted in **Figure 2-9** show the response of the liquid temperature inside the flow cell when the temperature of the heater elements increases from 40 °C to 50 °C. The temperature oscillations of the heater elements (red line) are caused by the PID controller trying to achieve the requested temperature as fast as possible. A fitting algorithm based on an adapted version of Newton's law of cooling and heating (**Equation 2.4**)[32] was applied to the liquid temperature data (dotted line) resulting in a value of $0.0018 \pm 3.8 \cdot 10^{-6}$ s^{-1} (R^2 = 0.997) for the time constant $\bar{\alpha}$. In case the heater temperature would follow a step profile, the fit is expected to be perfect. However, during the first 10 minutes the heater temperature oscillates due to PID regulation. After this initial phase, the heater temperature stabilizes and changes in liquid temperature now fit perfectly with Newton's law of cooling and heating[32]. The temperature of the liquid inside the flow cell stabilizes at its new level within 30 minutes.

$$T(t) = T_{\text{end}} - (T_{\text{end}} - T_{\text{start}}) \cdot \exp\{-\bar{\alpha} \cdot t\} \qquad (2.4)$$
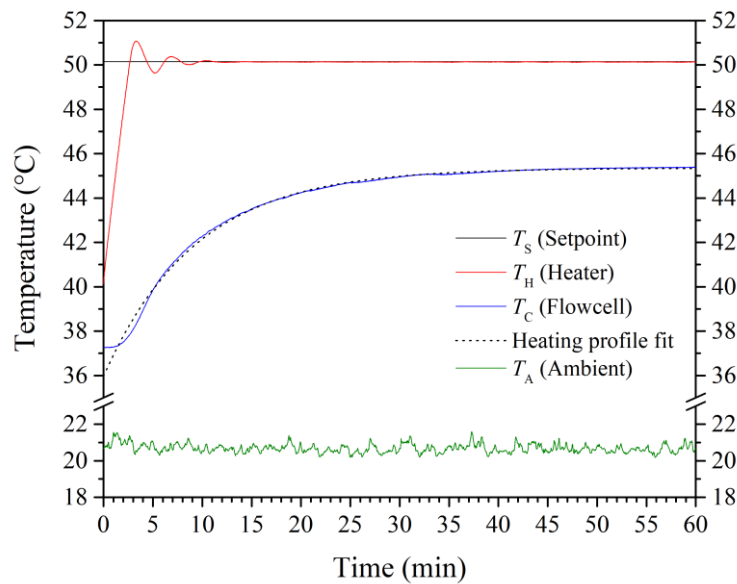
Figure 2-9 *The left temperature scale refers to the heater temperature T_H (red line) while the right scale refers to the flow cell temperature T_C (blue line). Fluctuations in the ambient temperature T_A are presented as a green line. An adapted version of Newton's law of cooling and heating (**Equation 2.4**) was used to calculate a fit based on this profile (dotted line).*

2.4.1 Validation of the Impedance Analyzer

As an example, **Figure 2-10** shows the impedance measurement results for both the Novocontrol and the DISC/EBU when the liquid temperature was stabilized at 30 °C. For both devices error bars were calculated by averaging three consecutive measurements. Comparing the results from both devices confirms that in the chosen frequency range the accuracy of the DISC/EBU is just as good as an established, high-end commercial instrument. Only at very low frequencies (around 10 Hz) a significant difference can be seen. However, at those frequencies the device operates beyond the frequency limits of the AD5933 impedance analyzer chip. Comparing the impedance measurements results yielded a similar agreement between both
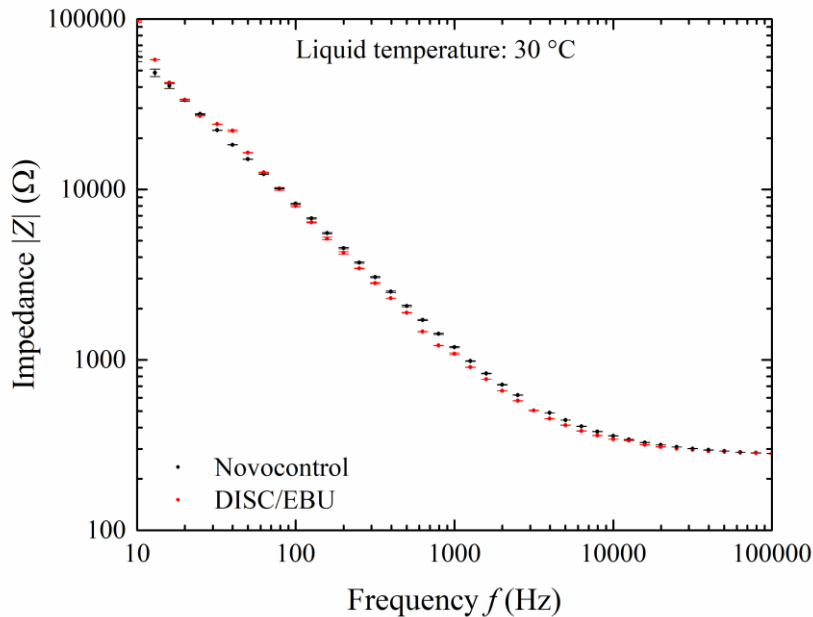
Figure 2-10 Comparison of the impedance amplitude measurement results between the DISC/EBU (red circles) and the Novocontrol instrument (black circles) using 1 × PBS as the liquid medium in the flow cell.

instruments for the other liquid temperatures tested (25 °C, 30 °C, 35 °C, 37 °C, 40 °C, 45 °C and 50 °C). Moreover, as expected a decreasing trend can be seen for the impedance amplitude with rising liquid temperatures.

Figure 2-11 shows the impedance phase angle measurement results for both the Novocontrol and the DISC/EBU after the liquid temperature was stabilized at 30 °C. The underlying dataset is the same one that was used for **Figure 2-10**. At frequencies below 300 Hz both devices become less accurate. Considering the entire frequency range, the results for both devices are similar within the 1000 Hz to 10 kHz range. Therefore, the DROID impedance analyzer inside the EBU can provide a good indication of the phase angle during impedance measurements when necessary. In biosensing measurements phase angles are mostly caused by capacitive effects. Therefore, the difference between the Novocontrol and the DROID concerning this aspect is probably due to a lack of calibration using reference capacitors in the DROID.
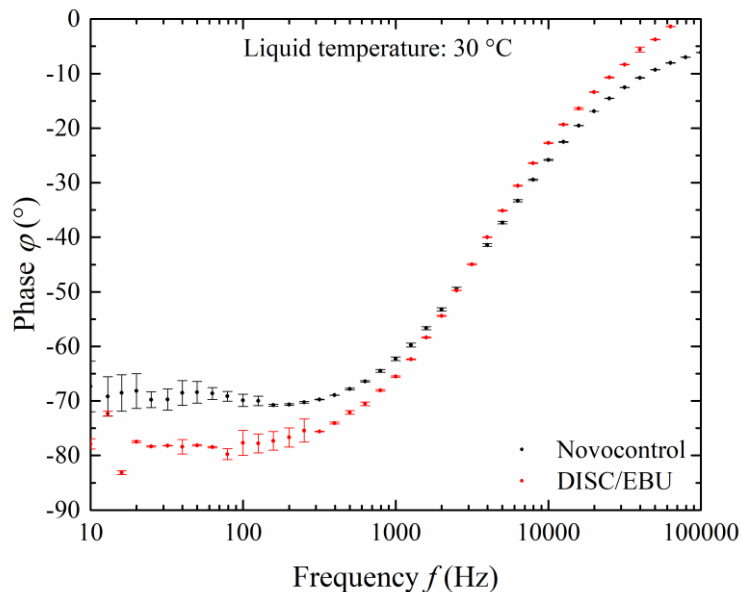
Figure 2-11 *Comparison of the impedance phase angle measurement results between the DISC/EBU (red circles) and the Novocontrol instrument (black circles) using 1 × PBS as the liquid medium in the flow cell.*

2.4.2 Equivalent Circuit Fitting

The complete impedimetric system of the DISC can be modeled using the equivalent circuit shown in **Figure 2-12**. The model consists of three resistive elements: R_S represents the resistance of the wiring between the electrode and the impedance analyzer, R_L is the resistance of the liquid inside the flow cell, and R_{CT} represents the resistance of the solid-liquid interface of the sensor surface. Furthermore, there are two capacitive elements: C_L represents the capacitance of the liquid inside the flow cell, which is negligible, while C_{DL} models the double-layer capacitance, which is created when ions from the liquid diffuse to the solid-liquid interface to form a monolayer that tries to compensate the surface charge. And finally, the Warburg element (A_W) models the slow-moving charges between the electrodes. Therefore, its contribution depends on the distance between the electrodes.
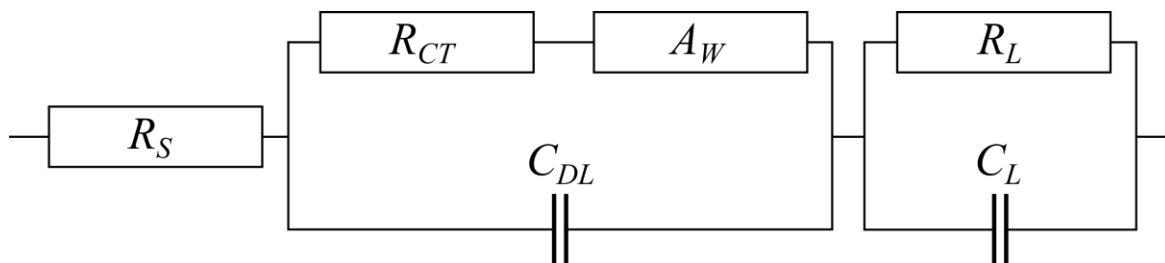
Figure 2-12 *The equivalent circuit used for fitting the impedance data. From left to right respectively, the device resistance (R_S), the interface model (charge-transfer resistance (R_{CT}), double-layer capacitance (C_{DL}) and Warburg element (A_W)) and the liquid model (liquid resistance (R_L) and liquid capacitance (C_L)).*

Using the equivalent circuit shown in **Figure 2-12**, the Novocontrol measurement data from **Figure 2-10** were fitted and the obtained fitting parameters are summarized in **Table 2-1**.

Table 2-1 *Fitting results Novocontrol data with an equivalent circuit.*

Parameter	Description	Value
R_S	Device resistance	$248 \pm 9\ \Omega$
A_W	Warburg coefficient	$344.6 \pm 32.9\ k\Omega.s^{-0.5}$
C_{DL}	Double-layer capacitance	$163 \pm 11\ nF$
R_{CT}	Charge-transfer resistance	$209 \pm 152\ \mu\Omega$
C_L	Liquid capacitance	$214 \pm 42\ nF$
R_L	Liquid resistance	$109 \pm 16\ \Omega$

In liquids, ions facilitate the movement of electrical current. Therefore, liquids with higher ionic strengths should have lower values for R_L. **Figure 2-13** shows the absolute impedance values of a $0.1 \times$, $1 \times$, and $10 \times$ PBS solution. In the higher frequencies (> 10 kHz), R_L is the main contributor to the impedance, which can be clearly seen as its absolute value drops with higher ionic strengths of the PBS solution. In the lower frequencies (< 1 kHz), C_{DL} is the main contributor to the impedance in this case because the slope of the impedance is close to -1, as opposed to a slope of -1/2 in case A_w is the main contributor.

These results are confirmed by the measured phase angles plotted in **Figure 2-14** for the same measurements. For an ideal resistor the phase angle equals $0\ °$, while the phase angle for an ideal capacitor equals $-90\ °$. In the higher frequencies the impedance behavior is almost purely ohmic. However, as the ionic strength of the liquid rises, the contribution of the liquid capacitance also rises. In the lower frequencies, the measurements show that as the ionic strength increases, and hereby also the number of available ions in the liquid, the impedance behavior resembles more and more that of an ideal capacitor.
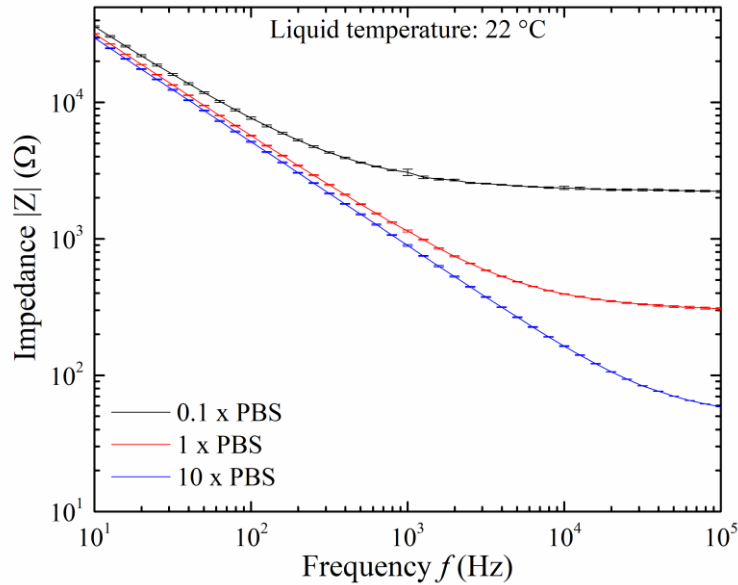
Figure 2-13 *Comparison of the absolute impedance values for 0.1 ×, 1 ×, and 10 × PBS solutions. Higher ionic strengths lower the resistance of the liquid (R_L), which can be seen in the higher frequencies (> 10 kHz), and increase the double-layer capacitance (C_{DL}), which can be seen in the steeper slopes visible in the lower frequencies (< 1 kHz).*
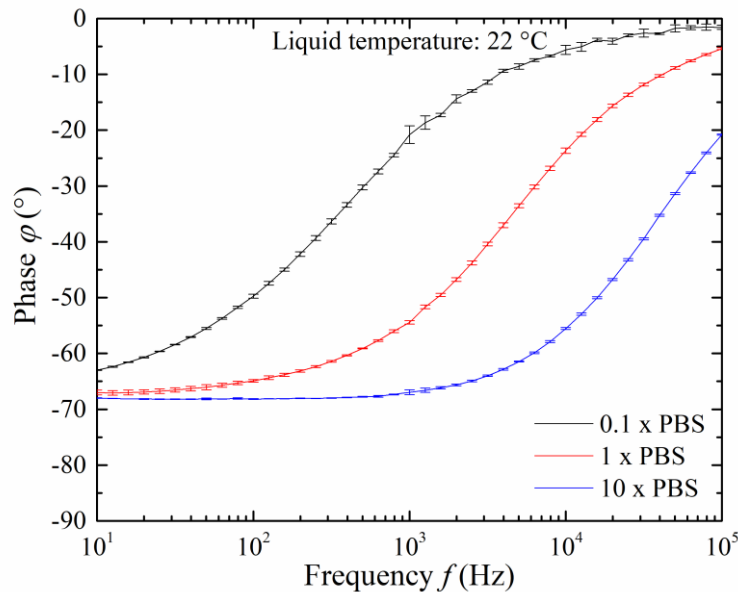
Figure 2-14 *Comparison of the phase angle measurements for 0.1 ×, 1 ×, and 10 × PBS solutions. At higher frequencies (> 10 kHz), the response comes close to an ideal resistor, which has a 0 ° phase angle, as R_L becomes the main contributor in the system, but only at low ionic strengths of the liquid. At lower frequencies (< 1 kHz), the system behaves more and more like an ideal capacitor, which has a 90 ° phase angle, as the ionic strength of the liquid increase. In this frequency range, the double-layer capacitance (C_{DL}) is the main contributor to the impedance signal.*

To evaluate the influence of the liquid inside the flow cell, impedance measurements were performed using different concentrations of PBS ($0.1 \times$, $1 \times$, and $10 \times$) and their results fitted to the equivalent circuit using Matlab software (**Table 2-2**).

Table 2-2 Comparison of the fitting results for different PBS concentrations.

Parameter	$0.1 \times$ PBS	$1 \times$ PBS	$10 \times$ PBS
R_S	$61.8 \pm 24.6\ \Omega$	$50.1 \pm 11.1\ \Omega$	$51.4 \pm 2.7\ \Omega$
A_W	$84 \pm 9.72\ k\Omega.s^{-0.5}$	$158 \pm 12.5\ k\Omega.s^{-0.5}$	$152 \pm 12\ k\Omega.s^{-0.5}$
C_{DL}	$28.4 \pm 2.8\ nF$	$125 \pm 9.7\ nF$	$148 \pm 11\ nF$
R_{CT}	$20.1 \pm 20.4\ \mu\Omega$	$177 \pm 142\ \mu\Omega$	$3.12 \pm 8.75\ \mu\Omega$
C_L	$0.16 \pm 0.02\ nF$	$84.1 \pm 12.1\ nF$	$164 \pm 21.7\ nF$
R_L	$1975 \pm 444\ \Omega$	$330.9 \pm 49.3\ \Omega$	$80.8 \pm 17.9\ \Omega$

Figure 2-15A-F shows the results for each individual circuit element. As expected, the device resistance R_S is constant because it represents the wires connecting the electrodes to the impedance analyzer and the internal resistance of the analyzer (**Figure 2-15A**). Higher PBS concentrations have a higher ionic strength. Therefore the resistance of PBS solutions decreases as its ionic strength increases, while its capacitance increases for the same reason (**Figure 2-15B-C**). The Warburg coefficient A_W is proportional to the square root of ion concentrations multiplied by the square root of the diffusion constants of the ions[33, 34]. **Figure 2-15D** shows that A_W is similar for the two highest PBS concentrations. This might be some kind of saturation effect. However, it is also possible that diffusion constants of the ions decrease with higher concentrations[35]. The charge-transfer resistance R_{CT} shows a lot of variation, but it is always very low ($\mu\Omega$) (**Figure 2-15E**). This element does not play a significant role in non-faradaic impedance spectroscopy, which was performed here, as opposed to in faradaic impedance

spectroscopy, which applies higher bias voltages to facilitate redox reactions. Finally, the double-layer capacitance of the electrode surface increases rapidly with increasing concentrations. However, it does reach a maximum value when the ion double-layer is completely formed (**Figure 2-15F**).
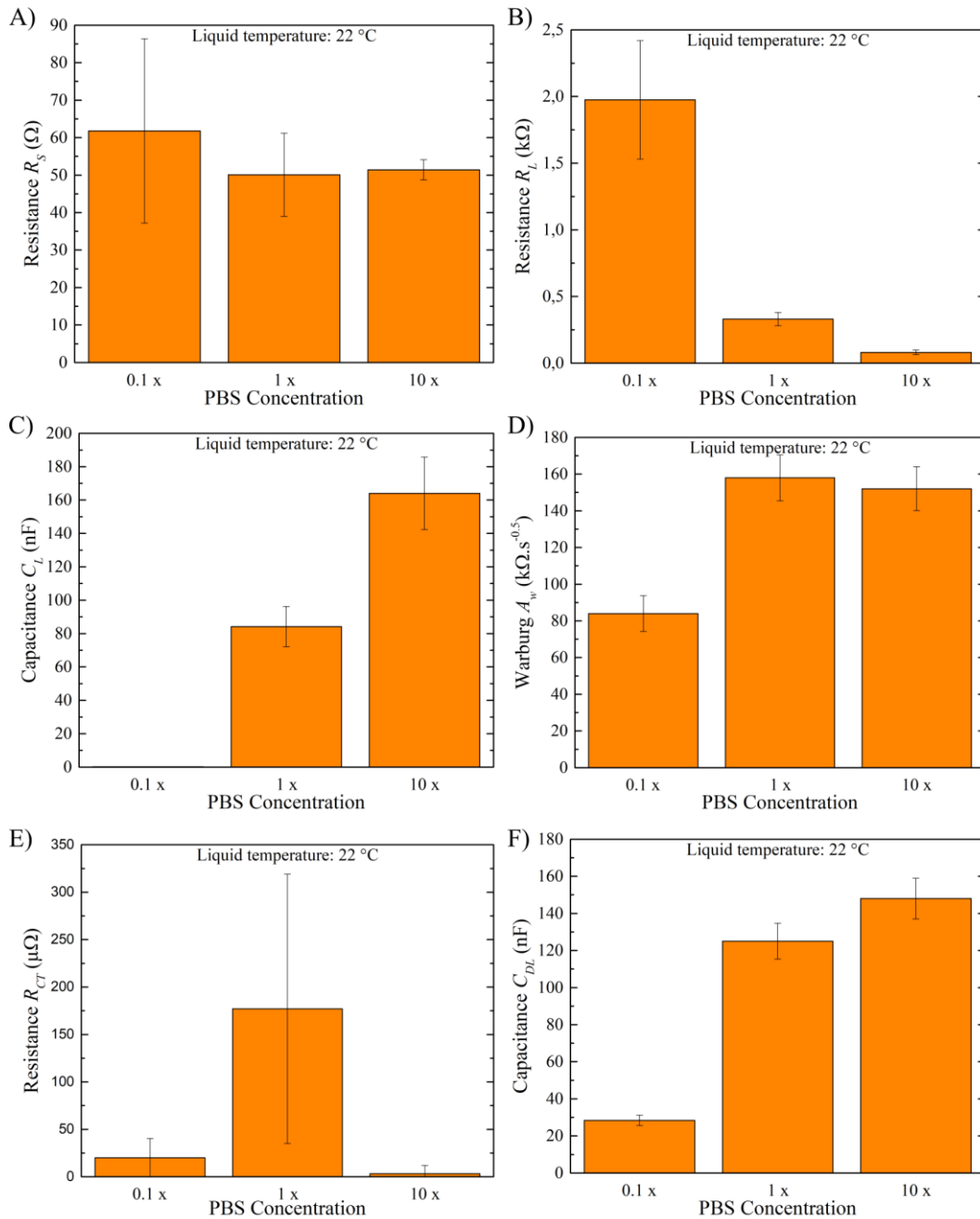
Figure 2-15 *Comparison of the fitting results for different PBS concentrations (0.1 ×, 1 ×, and 10 ×) for all elements of the equivalent circuit: A) Device resistance R_S, B) Liquid resistance R_L, C) Liquid capacitance C_L, D) Warburg coefficient A_W, E) Charge-transfer resistance R_{CT}, and F) Double-layer capacitance C_{DL}.*

2.4.3 Cell Constant Determination

Measurement cells in impedance spectroscopy are also characterized by their cell constant c, which is a measure of the ratio between the inter-electrode distance and the active surface area of the electrodes. Measurements with low conductivity require a low cell constant, while high conductivity measurements require a high cell constant[36]. The liquid resistance (R_L) was calculated to be 109 Ω (**Table 2-1**), and based on the conductivity of the $1 \times$ PBS solution (γ_{PBS}), which was measured at 1.2 S/m using a Mettler Toledo S230 conductivity meter, the cell constant was calculated to be 130.8 m^{-1} using **Equation 2.5**.

$$\gamma_{PBS} = \frac{1}{R_L} \cdot c \qquad \text{or} \qquad c = \gamma_{PBS} \cdot R_L \qquad (2.5)$$

This value is a very good approximation: Based on the flow cell geometry and a distance between the electrodes of 5 mm, a value of 147.5 m^{-1} was expected. This value was calculated using the average surface area of the chip (56.8 mm²) and the gold wire (11.0 mm²), resulting in an average electrode size of 33.9 mm².

2.5 Conclusion

The aim of this work was to develop an easy to use device to perform simultaneous multi-channel impedance measurements on a single liquid sample. In its simplest form, it measures one bio-molecular target and one background reference. Using two 4-channels models any combination of reference and target sensors can be used up to a total of 8 channels. The heating characteristics of the system show that it is fast, liquid temperature stabilizes within 30 minutes after changing the setpoint temperature for the heater elements, and that it has a linear correlation between the temperature of the heater elements and the liquid inside the flow cell allowing precise control of all temperatures. Moreover, the performance of the custom-made

DROID impedance analyzer was validated against a high-resolution dielectric spectrometer from Novocontrol. All these results clearly demonstrate the promising potential of the DISC/EBU system. More proof-of-concept measurements are ongoing to determine the performance of this novel and innovative device in more detail in real bioanalytical applications.

Acknowledgements

References

[1]   E. B. Bahadir and M. K. Sezginturk, A review on impedimetric biosensors, *Artificial Cells Nanomedicine and Biotechnology* **44** (1), 248-262 (2016).

[2]   M. I. Prodromidis, Impedimetric immunosensors-A review, *Electrochimica Acta* **55** (14), 4227-4233 (2010).

[3]   J. S. Daniels and N. Pourmand, Label-free impedance biosensors: Opportunities and challenges, *Electroanalysis* **19** (12), 1239-1257 (2007).

[4]   E. Katz and I. Willner, Probing biomolecular interactions at conductive and semiconductive surfaces by impedance spectroscopy: Routes to impedimetric immunosensors, DNA-Sensors, and enzyme biosensors, *Electroanalysis* **15** (11), 913-947 (2003).

[5]   M. Riedel, J. Kartchemnik, M. J. Schöning and F. Lisdat, Impedimetric DNA detection-Steps forward to sensorial application, *Analytical Chemistry* **86** (15), 7867-7874 (2014).

[6]   M. S. Murib, B. van Grinsven, L. Grieten, S. D. Janssens, V. Vermeeren, K. Eersels, J. Broeders, M. Ameloot, L. Michiels, W. De Ceuninck, K. Haenen, M. J. Schöning and P. Wagner, Electronic monitoring of chemical DNA denaturation on nanocrystalline diamond electrodes with different molarities and flow rates, *Physica Status Solidi a-Applications and Materials Science* **210** (5), 911-917 (2013).

[7]   B. van Grinsven, N. Vanden Bon, L. Grieten, M. Murib, S. D. Janssens, K. Haenen, E. Schneider, S. Ingebrandt, M. J. Schöning, V. Vermeeren, M. Ameloot, L. Michiels, R. Thoelen, W. De Ceuninck and P. Wagner, Rapid assessment of the stability of DNA duplexes by impedimetric real-time monitoring of chemically induced denaturation, *Lab Chip* **11** (9), 1656-1663 (2011).

[8]   J. Posseckardt, C. Schirmer, A. Kick, K. Rebatschek, T. Lamz and M. Mertig, Monitoring of *Saccharomyces cerevisiae* viability by non-Faradaic impedance spectroscopy using interdigitated screen-printed platinum electrodes, *Sensors and Actuators B: Chemical* **255**, 3417-3424 (2018).

[9]   A. Kleppisius, A. Kick and M. Mertig, Double-layer capacitance of pH-sensitive self-assembled thiol layers on gold determined by electrical impedance spectroscopy in a microfluidic channel, *Physica Status Solidi a-Applications and Materials Science* **214** (9), 1600921 (2017).

[10]   V. Vermeeren, L. Grieten, N. Vanden Bon, N. Bijnens, S. Wenmackers, S. D. Janssens, K. Haenen, P. Wagner and L. Michiels, Impedimetric, diamond-based immmunosensor for the detection of C-reactive protein, *Sensors and Actuators B: Chemical* **157** (1), 130-138 (2011).

[11]   D. T. Tran, V. Vermeeren, L. Grieten, S. Wenmackers, P. Wagner, J. Pollet, K. P. P. Janssen, L. Michiels and J. Lammertyn, Nanocrystalline diamond impedimetric aptasensor for the label-free detection of human IgE, *Biosensors and Bioelectronics* **26** (6), 2987-2993 (2011).

[12]   R. E. Ionescu, C. Gondran, L. Bouffier, N. Jaffrezic-Renault, C. Martelet and S. Cosnier, Label-free impedimetric immunosensor for sensitive detection of atrazine, *Electrochimica Acta* **55** (21), 6228-6232 (2010).

[13]   M. Peeters, F. J. Troost, R. H. G. Mingels, T. Welsch, B. van Grinsven, T. Vranken, S. Ingebrandt, R. Thoelen, T. J. Cleij and P. Wagner, Impedimetric detection of histamine in bowel fluids using synthetic receptors with pH-optimized binding characteristics, *Analytical Chemistry* **85** (3), 1475-1483 (2013).

[14]   M. Peeters, F. J. Troost, B. van Grinsven, F. Horemans, J. Alenus, M. S. Murib, D. Keszthelyi, A. Ethirajan, R. Thoelen, T. J. Cleij and P. Wagner, MIP-based biomimetic sensor for the electronic detection of serotonin in human blood plasma, *Sensors and Actuators B: Chemical* **171**, 602-610 (2012).

[15]   R. Thoelen, R. Vansweevelt, J. Duchateau, F. Horemans, J. D'Haen, L. Lutsen, D. Vanderzande, M. Ameloot, M. vandeVen, T. J. Cleij and P. Wagner, A MIP-based impedimetric sensor for the detection of low-MW molecules, *Biosensors and Bioelectronics* **23** (6), 913-918 (2008).

[16]   K. Norman, N. Stobaus, M. Pirlich and A. Bosy-Westphal, Bioelectrical phase angle and impedance vector analysis--clinical relevance and applicability of impedance parameters, *Clinical Nutrition* **31** (6), 854-861 (2012).

[17]   M. Y. Jaffrin and H. Morel, Body fluid volumes measurements by impedance: A review of bioimpedance spectroscopy (BIS) and bioimpedance analysis (BIA) methods, *Medical Engineering & Physics* **30** (10), 1257-1269 (2008).

[18]   J. R. Mager, S. D. Sibley, T. R. Beckman, T. A. Kellogg and C. P. Earthman, Multifrequency bioelectrical impedance analysis and bioimpedance spectroscopy for monitoring fluid and body cell mass changes after gastric bypass surgery, *Clinical Nutrition* **27** (6), 832-841 (2008).

[19]   L. Lehane and J. Olley, Histamine fish poisoning revisited, *International Journal of Food Microbiology* **58** (1-2), 1-37 (2000).

[20]   L. F. Bjeldanes, D. E. Schutz and M. M. Morris, On the aetiology of scombroid poisoning: cadaverine potentiation of histamine toxicity in the guinea-pig, *Food and Cosmetics Toxicology* **16** (2), 157-159 (1978).

[21]   T. P. Nguya, T. Van Phi, D. T. N. Tram, K. Eersels, P. Wagner and T. T. N. Lien, Development of an impedimetric sensor for the label-free detection of the amino acid sarcosine with molecularly imprinted polymer receptors, *Sensors and Actuators B: Chemical* **246**, 461-470 (2017).

[22] A. Bouafsoun, S. Helali, S. Mebarek, C. Zeiller, A. F. Prigent, A. Othmane, A. Kerkeni, N. Jaffrezic-Renault and L. Ponsonnet, Electrical probing of endothelial cell behaviour on a fibronectin/polystyrene/thiol/gold electrode by Faradaic electrochemical impedance spectroscopy (EIS), *Bioelectrochemistry* **70** (2), 401-407 (2007).

[23] W. Chen, W. Zhu, O. K. Tan and X. F. Chen, Frequency and temperature dependent impedance spectroscopy of cobalt ferrite composite thick films, *Journal of Applied Physics* **108** (3), 034101 (2010).

[24] D. M. Zhou, E. T. McAdams, A. Lackermeier and J. G. Jones, AC impedance of Ag/AgCl reference electrodes for use in disposable biosensors, *Proceedings of the 16th Annual International Conference of the IEEE Engineering in Medicine and Biology Society - Engineering Advances: New Opportunities for Biomedical Engineers, Pts 1&2*, 832-833 (1994).

[25] J. Broeders, S. Duchateau, B. van Grinsven, W. Vanaken, M. Peeters, T. Cleij, R. Thoelen, P. Wagner and W. De Ceuninck, Miniaturised eight-channel impedance spectroscopy unit as sensor platform for biosensor applications, *Physica Status Solidi a-Applications and Materials Science* **208** (6), 1357-1363 (2011).

[26] B. van Grinsven, T. Vandenryt, S. Duchateau, A. Gaulke, L. Grieten, R. Thoelen, S. Ingebrandt, W. De Ceuninck and P. Wagner, Customized impedance spectroscopy device as possible sensor platform for biosensor applications, *Physica Status Solidi a-Applications and Materials Science* **207** (4), 919-923 (2010).

[27] S. H. Wright, Generation of resting membrane potential, *Advances in Physiology Education* **28** (4), 139-142 (2004).

[28] J. Evertsson, F. Bertram, F. Zhang, L. Rullik, L. R. Merte, M. Shipilin, M. Soldemo, S. Ahmadi, N. Vinogradov, F. Carla, J. Weissenrieder, M. Gothelid, J. Pan, A. Mikkelsen, J. O. Nilsson and E. Lundgren, The thickness of native oxides on aluminum alloys and single crystals, *Applied Surface Science* **349**, 826-832 (2015).

[29] L. P. H. Jeurgens, W. G. Sloof, F. D. Tichelaar and E. J. Mittemeijer, Structure and morphology of aluminium-oxide films formed by thermal oxidation of aluminium, *Thin Solid Films* **418** (2), 89-101 (2002).

[30] D. Necas and P. Klapetek, Gwyddion: An open-source software for SPM data analysis, *Central European Journal of Physics* **10** (1), 181-188 (2012).

[31] A. De Vos, Thermodynamics of radiation energy conversion in one and in three physical dimensions, *Journal of Physics and Chemistry of Solids* **49** (6), 725-730 (1988).

[32] M. Gockenbach and K. Schmidtke, Newton's law of heating and the heat equation, *Involve* **2** (4), 419-437 (2009).

[33]   T. Q. Nguyen and C. Breitkopf, Determination of diffusion coefficients using impedance spectroscopy data, *Journal of the Electrochemical Society* **165** (14), E826-E831 (2018).

[34]   J. Huang, Diffusion impedance of electroactive materials, electrolytic solutions and porous electrodes: Warburg impedance and beyond, *Electrochimica Acta* **281**, 170-188 (2018).

[35]   J. S. Kim, Z. Wu, A. R. Morrow, A. Yethiraj and A. Yethiraj, Self-diffusion and viscosity in electrolyte solutions, *Journal of Physical Chemistry B* **116** (39), 12007-12013 (2012).

[36]   H. Acharya, N. J. Mozdzierz, P. Keblinski and S. Garde, How chemistry, nanoscale roughness, and the direction of heat flow affect thermal conductance of solid–water interfaces, *Industrial & Engineering Chemistry Research* **51** (4), 1767-1773 (2012).

Chapter 3: Sensitive and Specific Detection of *E. coli* using Biomimetic Receptors in Combination with a Modified Heat-Transfer Method

***Authors: <u>Peter Cornelis</u>**, Stella Givanoudi, Derick Yongabi, Heiko Iken, Sam Duwé, Olivier*

Deschaume, Johan Robbens, Peter Dedecker, Carmen Bartic, Michael Wübbenhorst,

Michael J. Schöning, Marc Heyndrickx, and Patrick Wagner.

Scientific contribution: *Design and assembly of the devices, design of experiments, data analysis,*

software development, writing the manuscript (corresponding author)
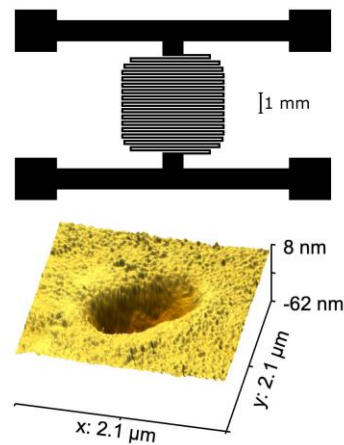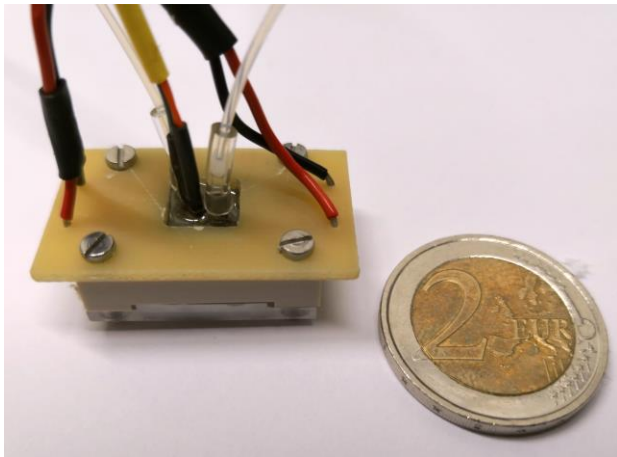
Highlights

- Surface imprinted polymers with a high affinity for *E. coli* and a negligible cross-sensitivity for other coliform bacteria

- The sensor chips consist of readily available and corrosion-resistant stainless-steel foils

- Sensor device uses a modified heat-transfer method with substantially improved thermal current focusing and noise levels

- Detection limit as low as 100 CFU/mL, both in PBS buffer and in non-cleared apple juice without sample-preparation

- The sensing device is especially low-cost and compact, matchbox size, making it also suitable for in-line measurements

Abstract

We report on a novel biomimetic sensor that allows sensitive and specific detection of *Escherichia coli* (*E. coli*) bacteria in a broad concentration range from 10^2 up to 10^6 CFU/mL in both buffer fluids and relevant food samples (i.e. apple juice). The receptors are surface imprinted polyurethane layers deposited on stainless-steel chips. Regarding the transducer principle, the sensor measures the increase in thermal resistance between the chip and the liquid due to the presence of bacteria captured on the receptor surface. The low noise level that enables the low detection limit originates from a planar meander element that serves as both a heater and a temperature sensor. Furthermore, the experiments show that the presence of bacteria in a liquid enhances the thermal conductivity of the liquid itself. Reference tests with a set of other representative species of *Enterobacteriaceae*, closely related to *E. coli*, indicate a very low cross-sensitivity with a sensor response at or below the noise level.

3.1 Introduction

Recently, biosensors have been developed for food safety and quality evaluation in food, feed, and environmental applications because of their advantageous rapidity and ease of use[1-3]. Crucial for a proficient (bio)sensor is the development of recognition elements with high affinity and specificity[4-8]. Specifically for microbes, be it pathogenic or other bacteria in the environment or food, the limitations associated with certain classical biorecognition elements and/or with a workable transducing system have led to a situation in which sensors are tested in lab conditions only, while not being suitable for real-life samples. In this work, we show that synthetic polymer receptors combined with the heat-transfer method (HTM) close this gap. Surface imprinted polymers (SIPs) constitute a type of biomimetic receptor that is already established as being selective in detecting its target[9, 10]. They can be synthesized in various

60

ways[11], and can also be coupled to a wide variety of detection platforms such as quartz-crystal microbalance (QCM)[12, 13], surface plasmon resonance (SPR)[12, 14], electrochemical impedance spectroscopy (EIS)[15], and thermal wave transport analysis (TWTA)[16]. Even without a transducer platform they have applications such as in the separation of bacteria[17] and cell sorting[18].

In recent years, experiments based on the heat-transfer method (HTM) have allowed to establish that small changes at the solid-liquid interface alter the efficiency of heat transfer from a solid chip to the supernatant liquid, for instance upon DNA denaturation[19], binding of cells to SIPs[9], or phase transitions in lipids[20]. Regarding cell detection, it is also known from molecular-dynamics simulations that the thermal conductivity of lipid bilayers is around four times lower than that of water[21]. Furthermore, HTM allows to study microbial growth, for example the proliferation of *Saccharomyces cerevisiae* strains[22]. In a nutshell, HTM monitors the thermal resistivity of a sample by measuring the temperature of a heat source at the backside of the sensor chip (T_H), the temperature inside the liquid (T_C) and the power (P) required by the system to keep T_H at a predefined value. The thermal resistance (R_{th}) is then calculated by dividing the temperature difference $T_H - T_C$ by the input power (**Equation 3.1**)[23]. R_{th} has the unit K/W, however we will use °C/W because only temperature differences play a role.

$$R_{th} = \frac{(T_H - T_C)}{P} \qquad (3.1)$$

E. coli is a relevant indicator for pathogenic enteric bacteria and for fecal contamination in environmental, food and agricultural samples, and therefore it is included in food safety regulations (see **Table 3-1**). In addition, *E. coli* is the organism of choice for the surveillance of drinking-water quality[24]. It is also frequently used as indicator organism in research on antimicrobial resistance, biosafety, and disinfection[25, 26]. Current detection methods for bacteria include polymerase chain reaction (PCR)[27], bacteriological colony counting[28], and

immunological[29] methods. Due to their sensitivity, selectivity and reliability, PCR and colony counting are the most used for *E. coli* enumeration in food and feed, for which standardized ISO methods are available[30]. The immunological methods employ antibody–antigen interactions to detect bacteria. The most proficient ELISA assay makes use of antibody specificity[31] and has a limit of detection (LoD) of 500 CFU/mL [29]. However, these methods are time-consuming and take from several hours up to days[31], thus hampering their use in acute situations, in which instant action is necessary. Moreover, they require trained staff and well-equipped laboratories. A recent potentiometric technique based on bacterial recognition by aptamers requires complex sample pre-treatment to remove all charged species[32]. Currently, the detection limit for *E. coli* using HTM combined with SIPs[33] or thermal wave transport analysis (TWTA)[16] is $1 \cdot 10^4$ CFU/mL, which is comparable to fluorescence microscopy[34] and electrochemical impedance spectroscopy (EIS)[15], implying that the LoD is too high for real-life samples. The goal of this work is to significantly lower the LoD to levels that comply with the legal limits for *E. coli* in various food products and water for different purposes, as required by European Commission regulations (**Table 3-1**).

The original implementation of the HTM[9] has a high noise level, which prohibits reaching detection limits low enough for relevant concentrations in food: The noise level on the R_{th} signal (see **Equation 3.1**) is the added uncertainty of the three independent parameters T_H, T_C, and P. To improve this, we replaced the heating unit by a planar meander-type metallic structure that acts simultaneously as a heat source and a temperature sensor for T_H, while T_C is measured with a calibrated Pt100 resistor at a fixed distance from the chip surface. The original design was also prone to parasitic heat flow losses, meaning that only a minor fraction of the power passed the bio-sensitive solid-liquid interface[35]. Moreover, the flow cell was made of poly(methyl methacrylate) (PMMA), which has a lower thermal conductivity than the water-based samples

Table 3-1 *European Commission Regulation (EC) 1441/2007 of 05/12/2007 on microbiological criteria for foodstuffs[36] and Council Directive 98/83/EC of 03/11/1998 on the quality of water intended for human consumption[37], and Proposal for a Directive of the European Parliament and of the Council concerning the quality of bathing water COM(2002) 581 final[38].*

Food, water, drinks	Legal limit[a] (*E. coli*)
Meat preparations	500 - 5000 CFU[b]/g
Cheeses (from heat treated milk)	100 - 1000 CFU[b]/g
Precut fruit and vegetables (ready-to-eat)	100 - 1000 CFU[b]/g
Unpasteurized fruit and vegetable juices (ready-to-drink)	100 - 1000 CFU[b]/g
Minced meat and mechanically separated meat	50 - 500 CFU[b]/g
Butter/cream from raw milk or milk with lower heat treatment than pasteurization	10 - 100 CFU[b]/g
Live bivalve mollusks and live echinoderms, tunicates and gastropods	230 MPN[c]/100 g
Shelled and shucked products of cooked crustaceans and molluscan shellfish	1 - 10 MPN[c]/g
Water (bathing)	250 - 500 CFU[b]/100 mL
Water (drinking)	0 CFU[b]/100 mL

a) The lowest value is the target value, while the highest value is the tolerance value as specified in the EC regulation 1441/2007. b) CFU: Colony forming units. c) MPN: Most probable number.

used in cell detection. This resulted in heat building up inside the flow cell, thereby affecting the measurement of T_C. These two system characteristics limit the control over the heat flow direction and intensity, thereby also limiting the sensitivity of the setup. In the new design, the materials of the flow cell were carefully chosen to avoid stagnation points in the heat flow. Thanks to a low aspect ratio of the flow cell, the risk of turbulent flow and air-bubble formation is reduced considerably.

3.2. Materials and Methods

3.2.1. Materials

Squared metallic substrates of size 10×10 mm² were cut from a 0.2 mm thick stainless-steel sheet[39]) and from a 0.5 mm thick aluminum sheet (Brico N.V., Leuven, Belgium). Microscope cover glasses of size 10×10 mm², 0.12 mm thick were purchased from VWR international BVBA (Leuven, Belgium). The Sylgard 184 silicone elastomer kit was purchased from Malvom N.V. (Schelle, Belgium). Acetone, isopropanol, sodium dodecylsulfate (SDS), anhydrous tetrahydrofuran (THF), bisphenol A, phloroglucinol, and 4,4'-diisocyanato-diphenylmethane were purchased from Sigma-Aldrich (Diegem, Belgium). Tissue culture grade Lysogeny broth and ampicillin sodium salt (91.0 - 102.0%) were purchased from VWR international BVBA (Leuven, Belgium). Phosphate buffer saline (PBS) solution with pH 7.4 was prepared using NaCl, Na_2HPO_4, and KH_2PO_4 purchased from Sigma-Aldrich (Diegem, Belgium). Non-cleared apple juice, meeting the requirements of the EU biolabel was purchased from Colruyt (Heverlee, Belgium) and used as received. *Citrobacter freundii* (LMG 3246[T]), *Hafnia alvei* (LMG 10392[T]), *Serratia marcescens* subsp. *Marcescens* (LMG 2792[T]) and *Escherichia blattae* (LMG 3030[T]) cultures were provided by ILVO. The *Escherichia coli* (JM109(DE3)) culture, a fluorescently green labeled lab-strain, was provided by the Laboratory for Nanobiology at KU Leuven. mEmerald-Paxillin-22 was a gift from M. Davidson (Addgene plasmid # 54219). The Mix & Go! *E. coli* transformation kit and buffer set was purchased from Zymo Research (Leiden, The Netherlands).

3.2.2. Meander-based Heat Source

To create the thermal gradient, which underlies the HTM principle, a meander structure was designed that was supplied with a variable current depending on the power required by the system (see **Figure 3-1A**). The meander consists of a gold layer deposited on a 1 mm thick glass substrate (10×15 mm²), using a 10 nm thick chromium adhesion layer [40]. The gold layer

is 100 nm thick and the meander lines are 100 µm wide with an interline distance of 50 µm (total length ≈ 15 cm, resistance ≈ 450 Ω). During calibration, to enable temperature measurements with the meander, the thermal coefficient of resistance (TCR) was determined as $(2.8 \pm 0.02) \cdot 10^{-3}$ °C^{-1}, which is comparable to the literature value for gold of $3.4 \cdot 10^{-3}$ °C^{-1}[41]. The four contact pads allow for a highly accurate Three-Point Delta resistance measurement of the meander, which will be discussed in detail in paragraph 3.2.4.

3.2.3. Optimized HTM Device

Figure 3-1B-D shows the device and its components from different perspectives. Heat losses from the heat source to the environment are limited by covering its backside with poly(methyl methacrylate) (PMMA) (λ = 0.2 W/m·K). A titanium (λ = 19.4 W/m·K) top cover on the flow cell was used to assist in directing the heat flow through the sensor chip by efficiently removing heat. A Pt100 sensor encased in the top cover provides the second required temperature for HTM measurements. Also, the flow cell has a low aspect ratio to achieve homo-
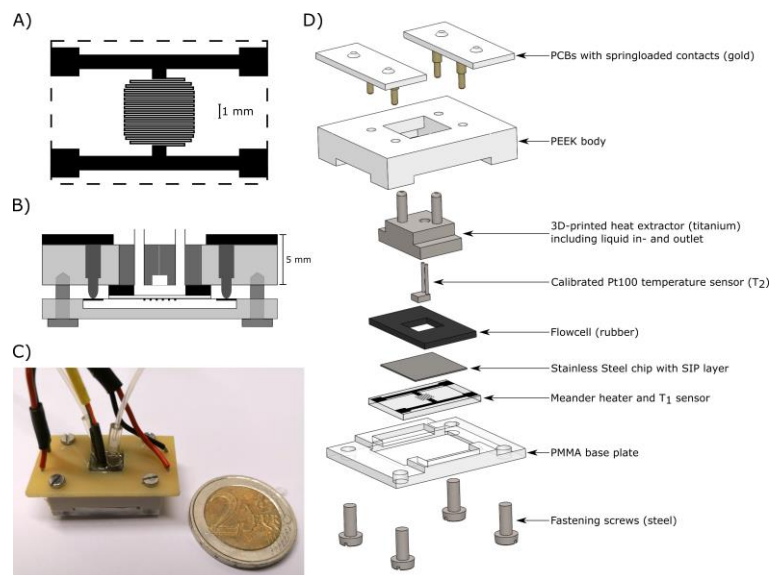
Figure 3-1 A) Schematic drawing of the meander structure of the heat source also used as T_H thermometer. The dashed line shows the dimensions of the supporting glass substrate. B) Schematic drawing of a cross-section of the HTM setup. C) Photo of the HTM-sensor device with a 2 € coin as a size reference. D) Schematic exploded view of the optimized HTM setup. All elements of the schematic drawings are drawn to scale (PEEK: Polyether ether ketone).

geneous heat flow and a laminar temperature profile, as suggested by Stilman et al.[35]. The flow cell compartment is 1 mm high with a surface area of 5×5 mm², resulting in an internal volume of 25 µL. Hence, the distance, over which the bacteria need to diffuse to be captured by the chip, is limited, which allows for a swift response.

3.2.4. Electronics and Software

To control the heat source, a combination of a Keithley 6221 current source and a Keithley 2182A nanovoltmeter was used. With this combination, the three-point delta measurement method was performed, which involved generating a square current wave and averaging three consecutive voltage measurements of the nanovoltmeter. Each voltage measurement was alternately taken at the center of a maximum and a minimum of the square wave. This method compensates for thermo-electric voltages and allows for accurate resistance measurements while also enabling control of the current amplitude and heating power. The Pt100 temperature sensor resistance was measured using the 4-wire resistance function of an HP 34401A digital multimeter. The entire measurement setup, including a proportional-integral-derivative controller for the heat source and remotely controlled syringe pumps (NE-500, ProSense, Oosterhout, The Netherlands), was controlled using an in-house LabView program.

3.2.5. Cell Cultures

Bacterial species were cultured in 200 mL lysogeny broth (LB) under a 5% CO_2 atmosphere at 37.0 °C (*C. freundii*), 30.0 °C (*H. alvei*), or 28.0 °C (*E. blattae* and *S. marcescens*) for a period of 24 - 48 h. Additionally, fluorescently labeled *E. coli* were generated by transforming Mix & Go! competent JM109(DE3) *E. coli* with pRSETb-mEmerald; Mix & Go! competent cells were prepared using the Zymo Research Transformation Kit, according to manufacturer's instructions. pRSETb-mEmerald was cloned by inserting the mEmerald coding sequence from mEmerald-Paxillin-22 between the *Bam*HI and *Eco*RI

restriction sites of pRSETb. Transformed *E. coli* were grown for 16 hours at 37.0 °C on LB agar plates supplemented with 100 µg/mL ampicillin. Liquid cultures were prepared by inoculating single colonies in 200 mL LB supplemented with 100 µg/mL ampicillin and growing the cultures for 24 hours at 37.0 °C in a shaking incubator (180 - 210 rpm). The cells were collected by centrifugation at 7500 rpm (7239 g) for 5 min at 4.0 °C and the pellet was resuspended in 5 mL of 1 × PBS. This washing step was repeated three times to remove all LB residues from the bacterial suspension. The cell concentration of these suspensions was then determined by measuring the optical density at 600 nm (OD600) using the Ocean Optics™ Red Tide VIS-NIR Fiber Optic Spectrometer.

3.2.6. Synthesis of SIP Receptor Chips

The soft-lithographic process of depositing a polymer coating with *E. coli* imprints on stainless-steel chips was performed under inert nitrogen atmosphere. First, 122 mg of 4,4'-diisocyanatodiphenylmethane and 222 mg of bisphenol A, which are functional monomers, were dissolved in 500 mL of anhydrous tetrahydrofuran (THF) together with 25 mg of phloroglucinol cross-linker. This mixture was stirred at 65.0 °C for 200 minutes until the solution turned into a gel. Then, it was diluted in a 1:5 ratio in THF and spin coated for 60 s at 2000 rpm onto stainless-steel substrates. Next, a cell-covered stamp (see below) was brought into the nitrogen atmosphere and gently pressed onto the polyurethane (PU) layer. This was left to cure for 18 h at 65.0 °C. After curing and returning to normal atmosphere, the stamp was removed from the surface and bound bacteria were removed by rinsing the layer with 1% SDS and 1 × PBS, leaving behind selective binding cavities on the polymer surface[9]. Finally, the backside of the substrate was covered with 40 µm thick Scotch™ tape to provide electrical insulation against the heating- and temperature-sensing gold meander.

The polydimethylsiloxane (PDMS) stamps, used for the imprinting step, were covered with template cells by applying 400 µL of an $8 \cdot 10^8$ CFU/mL *E. coli* stock solution onto the stamp,

and after 30 minutes sedimentation time, removing the excess liquid by spinning at 3000 rpm for 60 s. This creates a dense monolayer of template cells on the surface. The PDMS stamps (3 mm thick, 10×10 mm²) were made beforehand using the Sylgard 184 silicone elastomer kit. In addition to the SIPs, non-imprinted polymer (NIP) chips were made. The protocol used was the same except that pure $1 \times$ PBS was used instead of the *E. coli* stock solution. For comparison, SIP receptor chips were also prepared on glass and aluminum chips.

An optical contact angle device (DataPhysics, OCA 25, Filderstadt, Germany) was used to analyze the wetting behavior of these SIPs and NIPs by the sessile drop method. For all measurements, a 5 µL water drop was dispensed at a rate of 1.0 µL/s onto the surface of interest at 18.0 °C room temperature. Two SIP and two NIP surfaces were analyzed, and for each surface, measurements were performed on two spots. All chips were cleaned with SDS and Milli-Q water prior to measurements.

3.2.7 Optical and AFM Observations

To evaluate the SIPs after imprinting and to ensure complete removal of the bacteria from the cavities after template extraction, images of green-fluorescent *E. coli* expressing mEmerald were recorded with a Leica DM750 M microscope equipped with a HD Digital Camera (Leica MC170 HD) and a LED light source (Leica SFL100, excitation at 470 nm ± 20 nm). A Bruker Multimode 8 atomic force microscope (AFM) with MSNL-F cantilevers (f = 110 - 120 kHz, k = 0.6 N/m, average tip radius of 2 - 12 nm) was used for topographical imaging in PeakForce Tapping® mode. The AFM topography images were leveled, line-corrected and measured (height profiles) using Gwyddion software[42].

3.2.8. Dose-Response Behavior

Dose-response measurements of the R_{th} signal to detect *E. coli* were performed with two different liquids: For the first case with pure PBS as medium, a dilution series of overnight grown *E. coli* bacteria in pure $1 \times$ PBS solution was constructed with OD600 estimated

concentrations of 50, 100, 500, $1 \cdot 10^3$, $5 \cdot 10^3$, $1 \cdot 10^4$, $5 \cdot 10^4$ and $2 \cdot 10^5$ CFU/mL. In the second case, the bacteria in $1 \times$ PBS (5 vol.-%) were diluted with 95 vol.-% apple juice, resulting in the effective concentrations 0, 50, 100, 500, $1 \cdot 10^3$, $5 \cdot 10^3$, $1 \cdot 10^4$, $5 \cdot 10^4$, $1 \cdot 10^5$, $2 \cdot 10^5$ and $1 \cdot 10^6$ CFU/mL. In both cases the exposure protocol was identical, and the values given for flow rates, injection times and stabilization periods were optimized by a systematic variation of all parameters. The flow cell was filled with $1 \times$ PBS and left to stabilize for 5 to 10 minutes. After starting the measurement, the PBS was refreshed after 30 minutes and then the device was left to stabilize for another hour to define the baseline of the R_{th} signal. Then, the first and lowest cell concentration was measured using a four-step exposure protocol, which is illustrated in **Figure 3-2** exemplarily for the exposure to $5 \cdot 10^4$ CFU/mL of *E. coli*. Exactly the same protocol was used for each concentration of the dilution series in the order of increasing concentration. In the first step ("cell injection"), the cell suspension with the given concentration was delivered to the flow cell over a period of 5 minutes with a flow rate of 0.2 mL/min (1.0 mL in total) using a computer-controlled, automated syringe pump. In the second step ("cell sedimentation"), the flow halted, allowing the bacteria to sediment and bind to the SIP layer for a period of 20 minutes. In order to remove cells that were not bound specifically to the chip, a third step was performed, which involved flushing with pure PBS (5 minutes with 0.2 mL/min flow rate for a total volume of 1.0 mL). In the fourth step ("equilibrating"), the flow was stopped, and the sensor device was again allowed to reach thermal equilibrium for a period of 20 minutes. During the entire measurement series, the heater temperature (T_H) was kept constant at 37.0 °C, the ambient temperature being stable at 18.0 ± 0.1 °C.
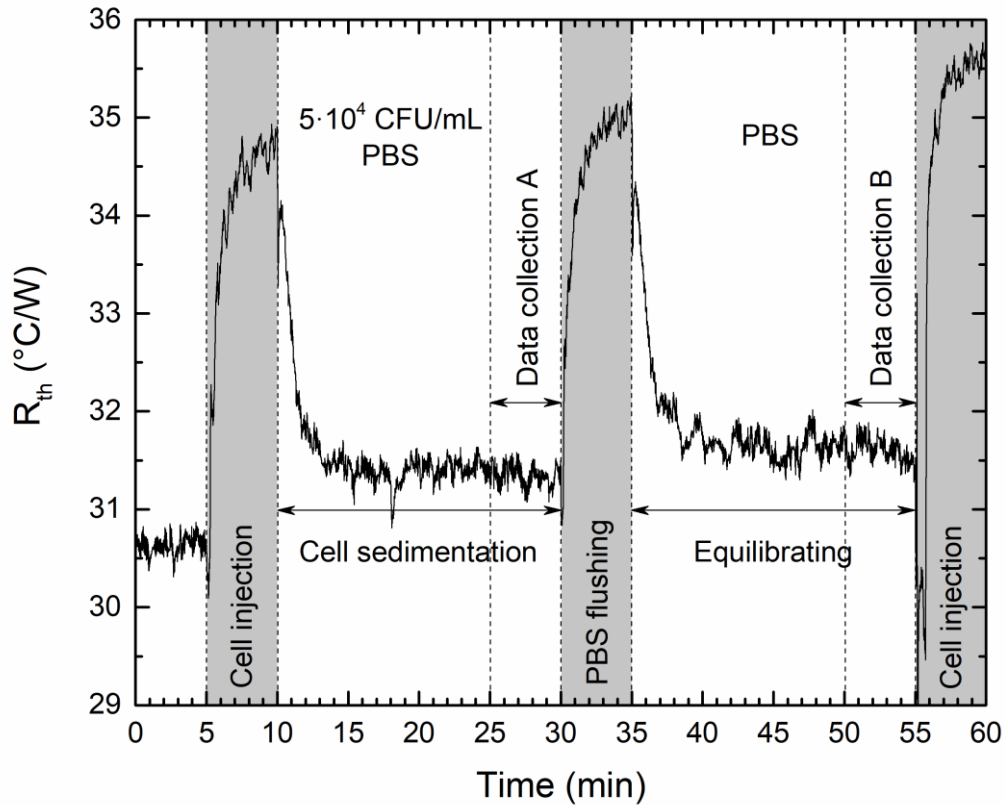
Figure 3-2 Detailed example of the four-step exposure protocol: The cell suspension injection during 5 minutes at a rate of 0.2 mL/min is followed by 20 minutes sedimentation time, 5 minutes of PBS flushing at 0.2 mL/min, and finally 20 minutes of equilibration.

3.2.9. Cross-sensitivity Testing

Cross-sensitivity of SIPs imprinted for *E. coli* were tested for their response to four closely related bacterial species, resembling *E. coli* in shape, size and cell membrane composition; i.e. *Citrobacter freundii*, *Hafnia alvei*, *Serratia marcescens* and *Escherichia blattae*. Each measurement started in PBS and after 30 minutes, fresh PBS was injected into the flow cell and left to stabilize for an additional 60 minutes. Next, a $1 \cdot 10^6$ CFU/mL concentration of a selected bacterial strain was injected. This high concentration was chosen on purpose to allow detecting very low levels of cross-sensitivity. After 25 minutes, the flow cell was flushed with pure PBS and again left to stabilize for 25 minutes. All injections were performed at a rate of 0.2 mL/min for 5 minutes, with a total injected volume of 1 mL. During all measurements,

the heater temperature (T_H) was kept constant at 37.0 °C. The same measurement was also done for a $1 \cdot 10^6$ CFU/mL concentration of *E. coli* as a reference. The resulting signals from the five individual measurements were then compared to assess the cross-sensitivity of these competitors with respect to the *E. coli* SIP. Each measurement was performed using a new SIP to ensure identical conditions. All SIPs for this purpose had been produced in the same batch.

3.3. Results and Discussion

3.3.1. SIP Receptor Chips

Figure 3-3 shows a fluorescence microscope image of a SIP imprinted with *E. coli*. As a reference, the inset of **Figure 3-3** shows the scanning electron microscope (SEM) image of an individual *E. coli* bacterium. The average *E. coli* bacterium has a diameter of 0.25 - 1 µm and
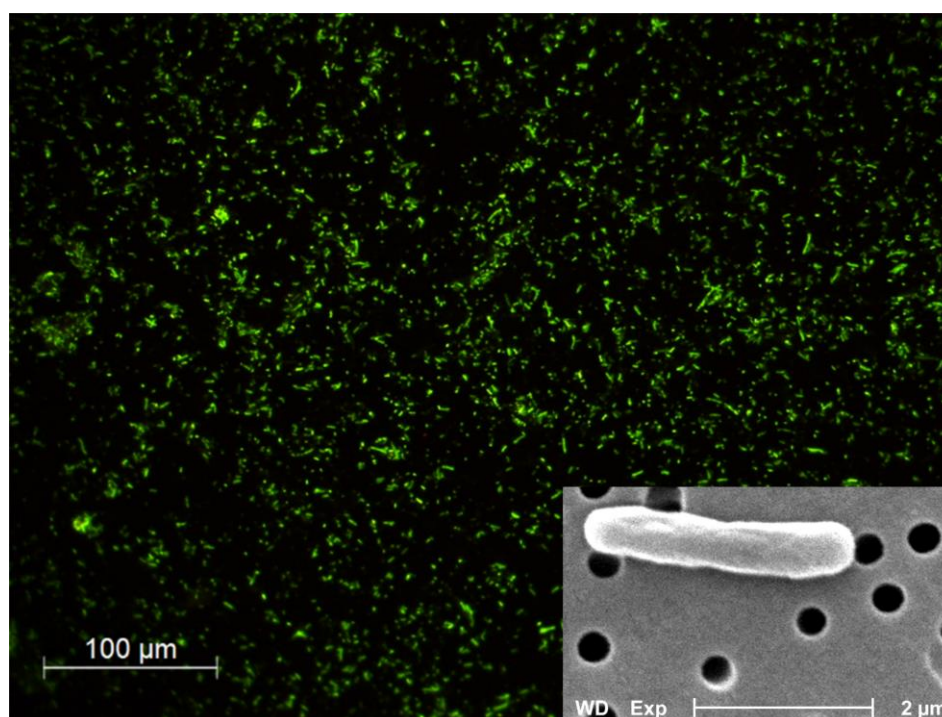
Figure 3-3 *Fluorescence image of a SIP imprinted on steel with fluorescent E. coli before the washing (magnification: 20 ×) (inset: SEM image of a single E. coli bacterium at 12800 × magnification).*

a length of about 2 µm. The cavities resulting from the imprinting process match these dimensions perfectly, as shown from the AFM profile analysis (**Figure 3-4A**). In order to
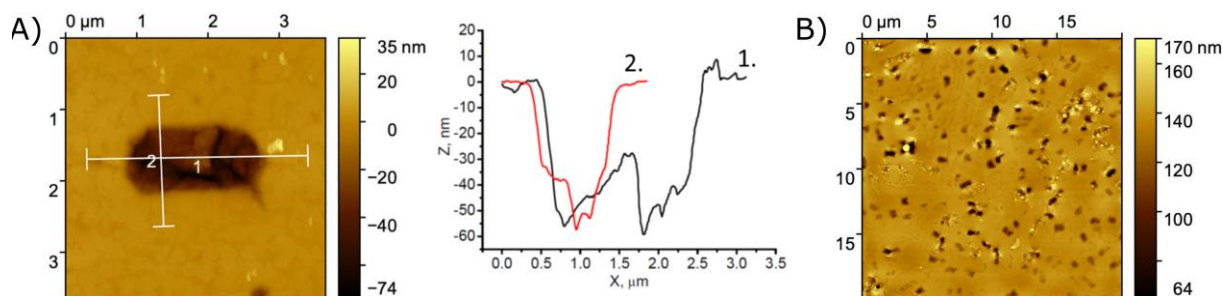
Figure 3-4 A) AFM profile analysis of a cavity created by the imprinting process. Length (1.9 µm) and width (0.96 µm) correspond very well to the size of an E. coli bacterium. The depth of the cavity (50 nm) is about one fifth of the thickness of the bacterium, the polyurethane layer is about 1 µm thick. B) AFM overview image used to calculate the surface coverage of the SIP receptor chip.

confirm that the cavities were created by the imprinted bacteria, an AFM image was taken before and after the washing step. In order to determine the homogeneity of the surface coverage of the SIP, a fluorescence microscopy image was taken before the washing step, exploiting the fact that fluorescent *E. coli* were used to make the imprints (**Figure 3-3**). Another fluorescence microscopy image was taken after the washing step to confirm that all fluorescent *E. coli* were removed during washing. To estimate the surface coverage of the SIP receptor chip, a 20×20 µm² AFM image was taken (**Figure 3-4B**), resulting in a value of 6.5 ($\pm$ 0.7) $\cdot 10^6$ cavities/cm². The SIP technique can be used on various support materials, as shown by the AFM images in **Figure 3-5**.

The average contact angle of the NIP surfaces is $72.0 \pm 3.0°$, which is comparable to literature values for polyurethane, thus confirming that the surface is covered with a polyurethane layer[43, 44]. On the other hand, the average contact angle on the SIP layers is $101.0 \pm 2.0°$. A similar increase in contact angle of polyurethane layers imprinted with cells has been reported in previous studies on SIPs synthesized by imprinting yeast cells[43].
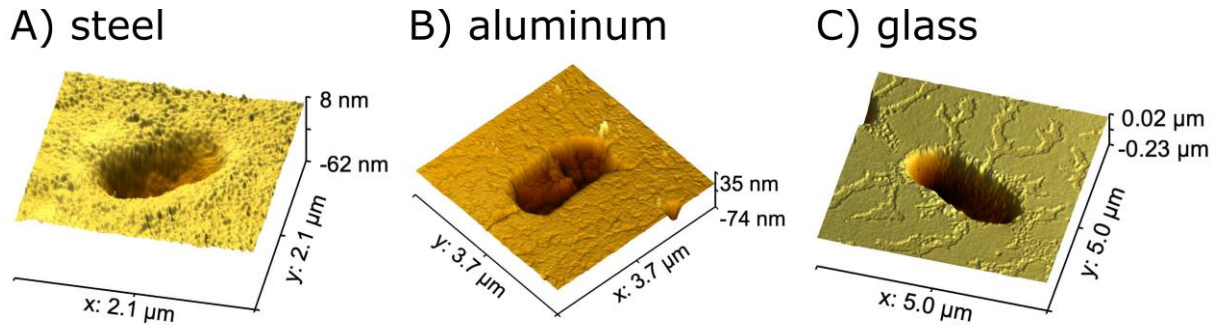
Figure 3-5 *3D AFM images of an empty cavity made on different support materials (respectively steel, aluminum and glass).*

3.3.2. Dose-Response Characterization with PBS Medium

Figure 3-6 shows the results of a recognition experiment for an *E. coli* SIP, which was exposed to increasing *E. coli* concentrations in PBS, starting from pure PBS over 50 CFU/mL to $2 \cdot 10^5$ CFU/mL. The sensor chip was not regenerated between the measurement for a given concentration and the next-higher concentration, owing to the difficulty to perform an efficient regeneration protocol inside the limited volume of the flow cell. The R_{th} value displays a systematic, stepwise increase and the apparent spikes in between the different concentrations arise from introducing room temperature liquids (cell suspensions and pure PBS) into the flow cell. This causes a temporary drop of the T_C parameter, resulting in sharp maxima of the R_{th} signal. For the highest concentration of $2 \cdot 10^5$ CFU/mL, the total increase in R_{th} with respect to the baseline (established with pure PBS) is 3.6 °C/W. This is twice the difference of $\Delta R_{th} \approx 1.7$ °C/W that was measured for the same concentration of *E. coli* using the classical heat-transfer method with a separate power source and two thermocouples[33].

The R_{th} data used to generate the dose-response curves in **Figure 3-7** and **Figure 3-9** were collected for each of the concentrations in twofold: In the sedimentation step (data collection A, see **Figure 3-2**) and in the equilibration step (data collection B, see **Figure 3-2**), for which the data of the final 5 minutes were taken where the R_{th} signal is stable without variation over
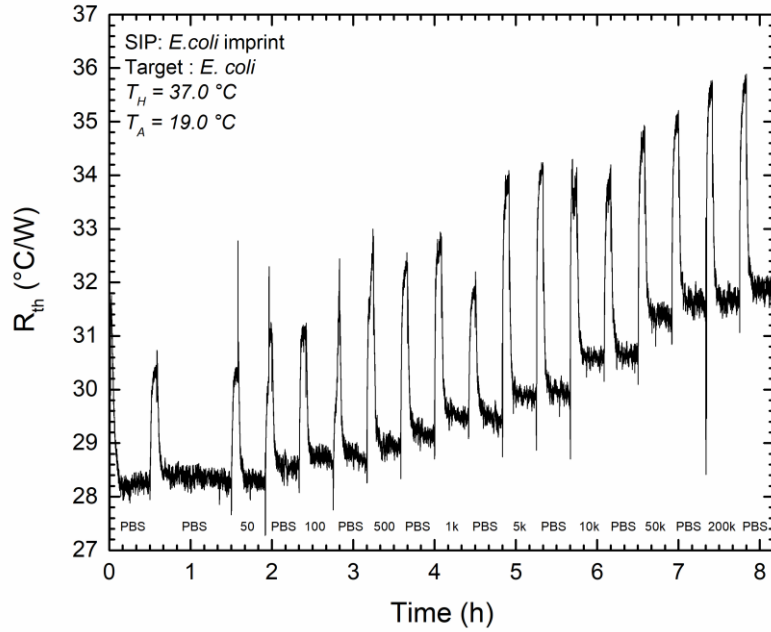
Figure 3-6 *Dose-response experiment performed on a SIP imprinted with E. coli. The SIP was exposed to increasing concentrations of target cells in PBS buffer (50, 100, 500, $1\cdot10^3$, $5\cdot10^3$, $1\cdot10^4$, $5\cdot10^4$, and $2\cdot10^5$ CFU/mL) alternated with PBS flushing. The thermal resistance increases noticeably in a systematic, concentration-dependent manner.*

Figure 3-7 *Dose-response curve for E. coli in PBS was created based on data sets from collection point A (sedimentation step, black squares) and collection point B (equilibration step, blue circles). Dose-response fits of the obtained data sets yielded R^2-values of respectively 0.92 (dataset A), and 0.96 (dataset B). The red dotted line corresponds to the 3σ level, defined as three times the standard deviation of the baseline measurement. Error margins were calculated as the standard deviation of the measurement during the 5-minute data collection period.*

time. For each of the two data sets, we calculated the numerical average and the standard deviation σ, which defines the height of the error bars in **Figure 3-7** and **Figure 3-9**. The goal of the equilibrating step is to have the flow cell filled with the pure buffer, thereby removing the influence of unbound cells on the R_{th} measurements.

The twofold data set obtained with *E. coli* in pure PBS reveals an interesting observation: The R_{th} values obtained in the equilibrating phase (after rinsing with pure PBS) are systematically higher than the R_{th} values in the cell-sedimentation phase, where a fraction of the administered bacteria is bound to the SIP chip while there are also unbound bacteria in the liquid. This proves directly that PBS containing cells has a lower thermal resistivity (higher thermal conductivity) than pure PBS. The fact that particles in a liquid enhance its thermal conductivity is known in literature from so-called "nanofluids" containing a small volume fraction of metal- or oxide-nanoparticles[45, 46]. Such additions can enhance the fluids' thermal conductivity by up to orders of magnitude and our results suggest that the effect is also present when cells are suspended in an electrolyte.

Thanks to this observation, the data point for the lowest concentration (100 CFU/mL) in the rinsed state, see **Figure 3-7**, lies already above the 3σ interval that defines the experimental uncertainty. Hence, there is a measured detection limit of 100 CFU/mL for the case with PBS buffer as matrix medium. Measurements of the entire concentration series were performed several times, recurrently showing this particularly low detection limit. The concentration axis in **Figure 3-7** is presented on a logarithmic scale and the dose-response fit function[47] is based on the following equation (**Equation 3.2**) incorporated in the Origin™ software package:

$$R_{th} = A_1 + \frac{(A_2 - A_1)}{\left(1 + 10^{\wedge}((\log(C_0) - C).p)\right)} \tag{3.2}$$

The goodness factor R^2 of the fit is 0.96 when pure PBS is present above the sensitive area (data collection B) and $R^2 = 0.92$ when the liquid contains unbound *E. coli* cells (data collection A). As can be expected, the difference between both data points becomes more pronounced when the concentration increases, the largest difference being observed for $2 \cdot 10^5$ CFU/mL.

3.3.3. Dose-Response in Apple Juice

Figure 3-8 shows the recognition experiment for an *E. coli* SIP, which was exposed to increasing *E. coli* concentrations in 95% apple juice, starting from pure PBS over 50 CFU/mL to $1 \cdot 10^6$ CFU/mL. Similar to the recognition experiment in PBS, no sensor chip regeneration was performed. The upper legal norm for *E. coli* in unpasteurized fruit juice is 1000 CFU/mL, see **Table 3-1**. In contrast to the measurement in a PBS matrix, the twofold data set obtained with E. coli in 95% apple juice shows R_{th} values obtained in the equilibrating phase (hence after rinsing with pure PBS) to be systematically lower than the R_{th} values in the cell-sedimentation phase. Therefore, we can conclude that apple juice has a higher thermal resistivity than pure PBS, as confirmed by the higher R_{th} of a 95% apple juice solution without *E. coli* compared to pure PBS. The concentration axis in **Figure 3-9** is also on a logarithmic scale and the dose-response fit function is based on equation (**Equation 3.2**). In this case, the goodness factor R^2 of the fit is 0.91 when pure PBS is present (data collection B) and $R^2 = 0.90$ when the liquid contains unbound *E. coli* cells with 95% apple juice as the medium (data collection A). The obtained limit-of-detection is roughly the same as for the measurement in a pure PBS matrix, more specifically 100 CFU/mL. Moreover, the ΔR_{th}, for example at $2 \cdot 10^5$ CFU/mL, is very similar, with values of 3.63 °C/W and 3.79 °C/W, respectively for the PBS and apple juice matrix.
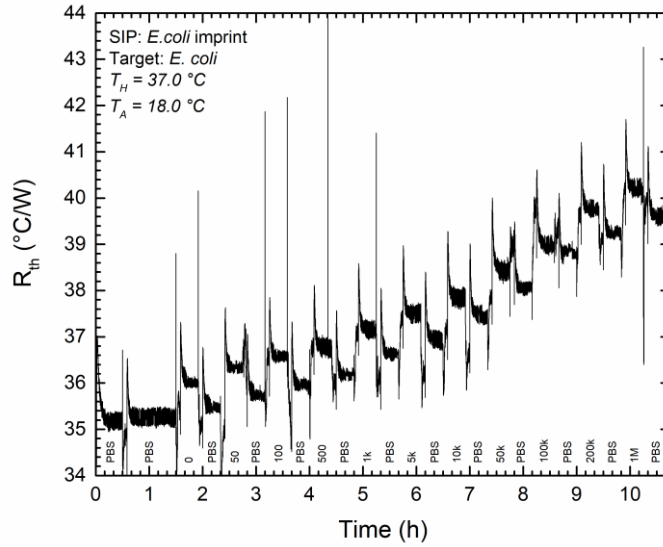
Figure 3-8 Dose-response experiment performed on a SIP imprinted with E. coli. The SIP was exposed to increasing concentrations of target cells in 95% apple juice (0, 50, 100, 500, $1·10^3$, $5·10^3$, $1·10^4$, $5·10^4$, $1·10^5$, $2·10^5$, and $1·10^6$ CFU/mL) alternated with PBS flushing. The thermal resistance increases noticeably in a systematic, concentration-dependent manner. Moreover, the thermal resistance of apple juice is systematically higher than PBS, which was expected.
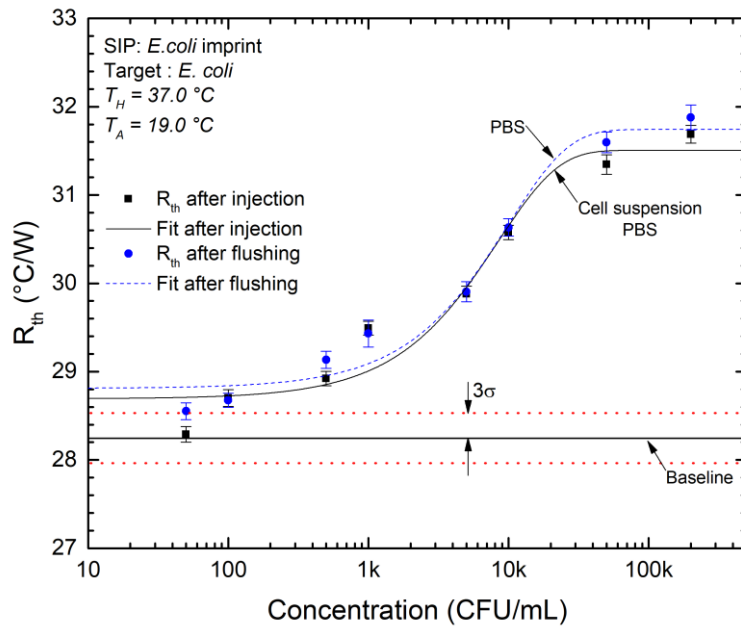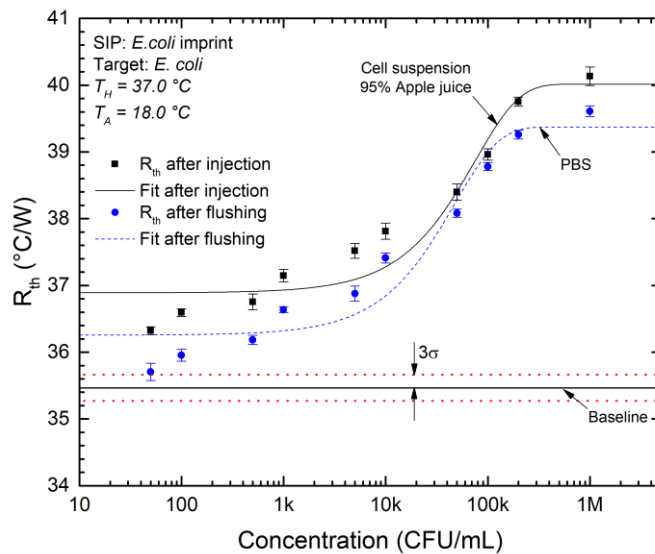

Figure 3-9 Dose-response curve for E. coli in 95% apple juice was created based on data sets from collection point A (sedimentation step, black squares) and collection point B (equilibration step, blue circles). Dose-response fits of the obtained data sets yielded R^2-values of respectively 0.90 (dataset A), and 0.91 (dataset B). The red dotted line corresponds to the 3σ level, defined as three times the standard deviation of the baseline measurement. Error margins were calculated as the standard deviation of the measurement during the 5-minute data collection period.

3.3.4. Cross-sensitivity Testing with *Enterobacteriaceae*

For a reliable identification of *E. coli* contaminations, it is important that the sensor system is adequately specific and not susceptible to false-positive results, which may originate from related organisms. It has recently been demonstrated that SIP receptors for *E. coli*, prepared with the same protocol we used here, have an unmeasurably low cross-sensitivity for a wide range of potential competitors including *Staphylococcus aureus*, *Klebsiella pneumonia*, *Pseudomonas aeruginosa*, *Enterococcus cecorum*, *Staphylococcus epidermidis*, *Acinetobacter baumannii*, and *Clostridium difficile*[16]. Furthermore, target cells have been selectively detected when they are mixed with a hundredfold excess of competitor cells[33]. As a persistent limitation, SIP receptors cannot yet distinguish between different *E. coli* strains, but this is less relevant when developing a sensor that should be sensitive to all possible subtypes of *E. coli* in order to assess conformance with legal microbiological criteria (**Table 3-1**).

In the present work, we pushed cross-sensitivity experiments a step further by testing the sensor with related *Enterobacteriaceae*. **Figure 3-10** shows the results of the cross-sensitivity measurements in which *E. coli* SIPs were exposed to *E. coli* itself and four closely related members of the *Enterobacteriaceae* family: *C. freundii*, *H. alvei*, *S. marcescens* and *E. blattae*, all with a $1 \cdot 10^6$ CFU/mL concentration. All these bacteria are Gram-negative with very similar dimensions and other features in common. More specifically, together with *E. coli*, the species belonging to these genera make up the coliforms, which is traditionally defined as the group of the *Enterobacteriaceae* with the ability to ferment lactose to acid and gas. Both *E. coli* and coliforms are fecal indicator bacteria because they inhabit the gastrointestinal tract of warm-blooded animals[48]. Coliforms are found in the aquatic environment, in soil, and on vegetation and therefore several coliform species can be simultaneously present in the same food, water or agricultural sample.

The response after injection, with unbound cells still present in the medium, is below the detection limit for all, except for *E. coli* itself. After flushing, with no unbound cells present in the medium, the response increases for all 5 species. However, the response for *S. marcescens* and *E. blattae* still remains below the detection limit and for *C. freundii* and *H. alvei* only slightly exceeds the detection limit indicating very limited cross-sensitivity to these species. The response for *E. coli* is slightly lower than expected from the dose-response curve. However, in this test the sensor was not previously exposed to lower concentrations, as was done in the dose-response curve of **Figure 3-6**. These results extend the established knowledge on cross-sensitivity, as described previously[16], and illustrate the discriminatory power of this biomimetic sensor technique to differentiate between *E. coli* and other *Enterobacteriaceae*.
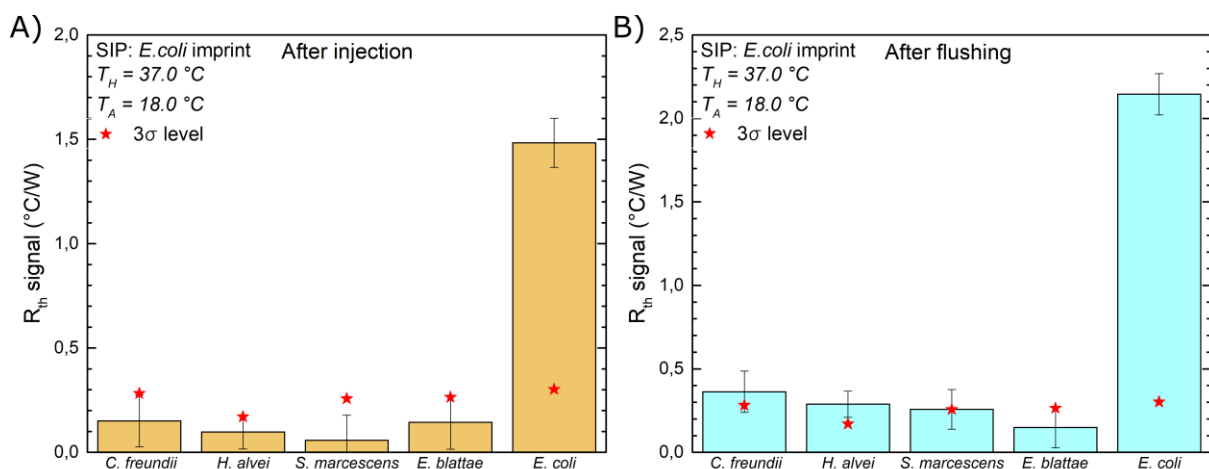
Figure 3-10 *Cross-sensitivity measurements with four coliform species of the Enterobacteriaceae family besides E. coli. All concentrations were uniformly $1 \cdot 10^6$ CFU/mL. The red stars represent the 3σ level of each measurement as defined from baseline. Error margins were calculated as the standard deviation of the measurement during the 5-minute data collection. A) After injection, with unbound cells still present in the medium, all measurements except the one with E. coli are below the detection limit. B) After flushing, without unbound cells in the medium, only two bacteria (C. freundii and H. alvei), besides E. coli, show a response above the detection limit. However, these responses are still more than five times lower when compared to the response obtained for E. coli.*

This level of selectivity cannot be explained solely by the geometry of the cavities in the SIPs because all bacterial strains used are similar in size and shape. Therefore, additional recognition mechanisms must be present. In fact, strong evidence was reported that chemical recognition, caused by remnants of cell membrane incorporated in the surface of the cavities[43, 49] and the arrangement of functional groups in the cavities[50] also play a role in the cell-SIP interaction.

3.3.5. Comparison with the State of the Art

An overview of the detection limits for various transducer/receptor combinations, without claiming to be exhaustive, is given in **Table 3-2**. This shows that the performance level of the

Table 3-2 Overview of detection limits of bio- and biomimetic sensors for bacterial detection.

Bacterial species[a]	Transducer principle	Receptor type	LoD	References
E. coli	Electromagnetic trap	Antibody	$6.6 \cdot 10^6$ CFU/mL (deionized water)	[51]
S. paratyphi	SPR	Microcontact imprinted polymer	$1.4 \cdot 10^6$ CFU/mL (water)	[14]
E. coli	QCM	Microcontact imprinted polymer	$3.72 \cdot 10^5$ CFU/mL (water)	[12]
D. radiodurans, S. natans, E. coli, B. subtilis, C. parvum	Fluorescence microscopy	Imprinted sol-gel films	10^3-10^4 CFU/mL (PBS)	[34]
P. aeruginosa, and *S. marcescens*	Dielectrophoresis	Molecularly imprinted polymers (MIP)	10^3 CFU/mL (water), 10^7 CFU/mL (apple juice)	[52]
E. coli, D. proteolyticus, S. epidermidis, S. pneumoniae	EIS	Cell imprinted polymer (CIP)	10^3 CFU/mL (PBS)	[15]
S. aureus	ELISA	Artificial antibodies / SIP	500 CFU/mL	[29]
C. jejuni	QCM	Mono- and polyclonal antibodies	150 CFU/mL (PBS)	[53]
E. coli	Capacitive	Microcontact imprinted sensor	70 CFU/mL (PBS)	[54]
E. coli	Potentiometric	Aptamers	4 CFU/mL (PBS)	[32]
E. coli	HTM	SIP	100 CFU/mL (PBS, apple juice)	This study

a) Escherichia coli (E. coli), Salmonella paratyphi (S. paratyphi), Deinococcus radiodurans (D. radiodurans), Sphaerotilus natans (S. natans), Bacillus subtilis (B. subtilis), Cryptosporidium parvum (C. parvum), Pseudomonas aeruginosa (P. aeruginosa), Serratia marcescens (S. marcescens), Deinococcus proteolyticus (D. proteolyticus), Staphylococcus epidermidis (S. epidermidis), Streptococcus pneumoniae (S. pneumoniae), Staphylococcus aureus (S. aureus), and Campylobacter jejuni (C. jejuni).

improved HTM sensor is comparable to the best current techniques for bacterial detection. Moreover, it demonstrates its sensitivity in a real food sample (fruit juice), even without further optimization or sample preparation.

3.3.6. Thermophysical Analysis of the Device

The baseline R_{th} value of the sensing device before cell recognition was always found in the limited range between 28 °C/W and 36 °C/W throughout all measurements. The scattering of the results arises from the fact that the constituting elements of the device are clamped mechanically, leading to variations in the thermal contact between the elements. The changes in ΔR_{th} upon binding bacteria are always concentration-dependent in the sense that a given dose of bacteria causes the same, absolute ΔR_{th} change, irrespective of the baseline value. A crosscheck calculation confirms that the baseline values comply with the dimensions of the device and the employed materials: The temperature difference $(T_H - T_C)$ measured between the meander and the Pt100 resistor in the top lid is related to a thermal current that passes through the electrically insulating Scotch tape (d_{tape} = 40.0 µm, λ_{tape} = 0.75 W/m·K), the steel chip (d_{steel} = 0.2 mm, λ_{steel} = 16.2 W/m·K), the imprinted PU layer (d_{PU} = 1.0 µm, λ_{PU} = 0.025 W/m·K), and the PBS liquid (d_{PBS} = 1.0 mm, λ_{PBS} = 0.6 W/m·K). The thermal conductivity λ values of water, steel, and polymers were taken from the Engineering Toolbox[55]. The meander measures A = 5 × 5 mm² and, as a simplification, we will in the following calculation only consider one-dimensional heat transport that is directed upward (from the meander through the liquid to the Pt100 sensor) and downward through the glass chip at the backside of the meander. The expected R_{th} value in the upward direction was calculated as follows; using thermal resistors in series (**Equation 3.3**):

$$R_{th}(expected) = \frac{1}{A}\left(\frac{d_{PBS}}{\lambda_{PBS}} + \frac{d_{PU}}{\lambda_{PU}} + \frac{d_{steel}}{\lambda_{steel}} + \frac{d_{tape}}{\lambda_{tape}}\right) = 71°C/W \qquad (3.3)$$

This is about twice the baseline value, but one should note that **Equation 3.1** assumes that the total heating power passes the solid-liquid interface while in reality a fraction of the power dissipates to the ambient through the backside of the chip and in lateral directions. Using the 1D-approximation, we can calculate the R_{th} value of the backside, in which heat passes through the glass chip ($d_{glass} = 1.0$ mm, $\lambda_{glass} = 1.05$ W/m·K), and the PMMA bottom of the device ($d_{PMMA} = 1.0$ mm, $\lambda_{PMMA} = 0.2$ W/m·K) (**Equation 3.4**):

$$R_{th}(backside) = \frac{1}{A}\left(\frac{d_{glass}}{\lambda_{glass}} + \frac{d_{PMMA}}{\lambda_{PMMA}}\right) = 238°C/W \tag{3.4}$$

To calculate the total R_{th} for the upward heat flow through the device, the contribution of the titanium cover ($d_{titanium} = 4.0$ mm, $\lambda_{titanium} = 19.4$ W/m·K) needs to be added to **Equation 3.3**, which results in a value of 79 °C/W. The fractions of power that are transmitted upward and downward are inversely proportional to the R_{th} values in the respective directions: In the given situation with $T_H = 37.0$ °C and $P_{total} = 192$ mW, this corresponds to an upward heat flow $P_{up} = 144$ mW and a heat flow through the backside $P_{down} = 48$ mW. In other words, the majority, namely 75% of the total heating power, passes the biosensitive interface. With this correction factor, the experimental R_{th} values (between 28 - 36 °C/W) translate into 37 - 48 °C/W, which agrees reasonably with the expected R_{th} value of 71 °C/W. Using more refined calculations, this model can be extended to three dimensions to include sideways heat dissipation and thermal boundary resistances between dissimilar materials. For the time being, the agreement between the 1D-model and the experimental results is satisfactory.

3.4. Conclusions

For this work, stainless-steel was selected because of its corrosion resistance, as most biosensor applications require contact with liquids, and its relatively high thermal conductivity,

which benefits the HTM principle. It is also a low-cost material, which is another advantage as the SIP receptor chip is the only consumable part of the setup. The bifunctional meander is a fixed part of the device that only needs to be recalibrated periodically. The entire device is not larger than a matchbox and in principle, it is also suitable for in-line applications due to the long-term stability of the synthetic SIP receptors.

The HTM setup, developed in this work, reaches a LoD of 100 CFU/mL, which is at the low end of the currently documented state-of-the-art sensor methods, irrespective of the underlying receptor type and transducer principle. Moreover, this concentration was actually measured and not extrapolated from higher concentrations. Even in the complex matrix of non-cleared apple juice, the LoD stays the same, underpinning the relevance of this new development for food safety analysis.

The SIP receptor chips were subjected to a stringent cross-sensitivity test resulting in a specific signal generated only for *E. coli* and not for the related species, all belonging to the coliform group of the *Enterobacteriaceae* family. These SIP receptors can be synthesized on a wide variety of readily available support materials.

The improved HTM device has now reached a performance level that brings the original HTM concept for cell detection from 2013[9] very close to real-life applications. Moreover, it is a generic concept, which can be easily adapted for other micro-organisms. The proof of concept delivered here for bacterial detection in real-life food applications can be used in a broader sense for environmental monitoring, agriculture and the diagnostics of infectious diseases.

Acknowledgements

References

[1]   P. Mehrotra, Biosensors and their applications – A review, *Journal of Oral Biology and Craniofacial Research* **6** (2), 153-159 (2016).

[2]   L. H. Wang, V. Kodeck, S. Van Vlierberghe, J. Ren, J. Teng, X. Y. Han, X. G. Jian, R. Baets, G. Morthier and M. S. Zhao, A low cost photonic biosensor built on a polymer platform, *Optical Sensors and Biophotonics III* **8311**, (2011).

[3]   P. Cliquet, B. M. Goddeeris, K. Bonroy and E. Cox, Penicillin-specific antibodies: Monoclonals versus polyclonals in ELISA and in an optical biosensor, *Food and Agricultural Immunology* **16** (2), 101-115 (2005).

[4]   M. A. Morales and J. M. Halpern, Guide to selecting a biorecognition element for biosensors, *Bioconjugate Chemistry* **29** (10), 3231-3239 (2018).

[5]   B. Van Dorst, J. Mehta, K. Bekaert, E. Rouah-Martin, W. De Coen, P. Dubruel, R. Blust and J. Robbens, Recent advances in recognition elements of food and environmental biosensors: A review, *Biosensors and Bioelectronics* **26** (4), 1178-1194 (2010).

[6]   J. P. Chambers, B. P. Arulanandam, L. L. Matta, A. Weis and J. J. Valdes, Biosensor recognition elements, *Current Issues in Molecular Biology* **10**, 1-12 (2008).

[7]   P. Leblebici, K. Leirs, D. Spasic and J. Lammertyn, Encoded particle microfluidic platform for rapid multiplexed screening and characterization of aptamers against influenza A nucleoprotein, *Analytica Chimica Acta* **1053**, 70-80 (2019).

[8]   S. M. Bian, J. D. Lu, F. Delport, S. Vermeire, D. Spasic, J. Lammertyn and A. Gils, Development and validation of an optical biosensor for rapid monitoring of adalimumab in serum of patients with Crohn's disease, *Drug Testing and Analysis* **10** (3), 592-596 (2018).

[9]   K. Eersels, B. van Grinsven, A. Ethirajan, S. Timmermans, K. L. Jiménez Monroy, J. F. Bogie, S. Punniyakoti, T. Vandenryt, J. J. Hendriks, T. J. Cleij, M. J. Daemen, V. Somers, W. De Ceuninck and P. Wagner, Selective identification of macrophages and cancer cells based on thermal transport through surface-imprinted polymer layers, *ACS Applied Materials & Interfaces* **5** (15), 7258-7267 (2013).

[10]   O. Hayden, K. J. Mann, S. Krassnig and F. L. Dickert, Biomimetic ABO blood-group typing, *Angewandte Chemie International Edition in English* **45** (16), 2626-2629 (2006).

[11]   K. Eersels, P. Lieberzeit and P. Wagner, A review on synthetic receptors for bioparticle detection created by surface-imprinting techniques—From principles to applications, *ACS Sensors* **1** (10), 1171-1187 (2016).

[12]   E. Yilmaz, D. Majidi, E. Ozgur and A. Denizli, Whole cell imprinting based *Escherichia coli* sensors: A study for SPR and QCM, *Sensors and Actuators B: Chemical* **209**, 714-721 (2015).

[13]   F. L. Dickert, O. Hayden and K. P. Halikias, Synthetic receptors as sensor coatings for molecules and living cells, *Analyst* **126** (6), 766-771 (2001).

[14]   I. Percin, N. Idil, M. Bakhshpour, E. Yilmaz, B. Mattiasson and A. Denizli, Microcontact imprinted plasmonic nanosensors: Powerful tools in the detection of *Salmonella paratyphi*, *Sensors* **17** (6), (2017).

[15]   M. Golabi, F. Kuralay, E. W. H. Jager, V. Beni and A. P. F. Turner, Electrochemical bacterial detection using poly(3-aminophenylboronic acid)-based imprinted polymer, *Biosensors and Bioelectronics* **93**, 87-93 (2017).

[16]   E. Steen Redeker, K. Eersels, O. Akkermans, J. Royakkers, S. Dyson, K. Nurekeyeva, B. Ferrando, P. Cornelis, M. Peeters, P. Wagner, H. Diliën, B. van Grinsven and T. J. Cleij, Biomimetic bacterial identification platform based on Thermal Wave Transport Analysis (TWTA) through surface-imprinted polymers, *ACS Infectious Diseases* **3** (5), 388-397 (2017).

[17]   R. Schirhagl, E. W. Hall, I. Fuereder and R. N. Zare, Separation of bacteria with imprinted polymeric films, *Analyst* **137** (6), 1495-1499 (2012).

[18]   K. N. Ren, N. Banaei and R. N. Zare, Sorting inactivated cells using cell-imprinted polymer thin films, *Acs Nano* **7** (7), 6031-6036 (2013).

[19]   B. van Grinsven, N. Vanden Bon, H. Strauven, L. Grieten, M. Murib, K. L. Monroy, S. D. Janssens, K. Haenen, M. J. Schöning, V. Vermeeren, M. Ameloot, L. Michiels, R. Thoelen, W. De Ceuninck and P. Wagner, Heat-transfer resistance at solid-liquid interfaces: A tool for the detection of single-nucleotide polymorphisms in DNA, *ACS Nano* **6** (3), 2712-2721 (2012).

[20]   P. Losada-Pérez, K. L. Jiménez-Monroy, B. van Grinsven, J. Leys, S. D. Janssens, M. Peeters, C. Glorieux, J. Thoen, K. Haenen, W. D. Ceuninck and P. Wagner, Phase transitions in lipid vesicles detected by a complementary set of methods heat-transfer measurements, adiabatic scanning calorimetry, and dissipation-mode quartz crystal microbalance, *Physica Status Solidi (a)* **211** (6), 1377-1388 (2014).

[21]   T. Nakano, G. Kikugawa and T. Ohara, A molecular dynamics study on heat conduction characteristics in DPPC lipid bilayer, *The Journal of Chemical Physics* **133** (15), 154705 (2010).

[22]   K. Betlem, S. Hoksbergen, N. Mansouri, M. Down, P. Losada-Pérez, K. Eersels, B. van Grinsven, T. J. Cleij, P. Kelly, D. Sawtell, M. Zubko, C. Banks and M. Peeters, Real-time analysis of microbial growth by means of the Heat-Transfer Method (HTM) using *Saccharomyces cerevisiae* as model organism, *Physics in Medicine* **6**, 1-8 (2018).

[23]   M. Lenz, U. Striedl and Fröhler, SMD Packages. Thermal resistance, theory and practice, *Released by Infineon Technologies AG, Munich, Germany*, (2000).

[24]   WHO, 2011. Guidelines for drinking-water quality, 4 ed. World Health Organization, Geneva, Switzerland.

[25] I. Dewaele, R. Ducatelle, L. Herman, M. Heyndrickx and K. De Reu, Sensitivity to disinfection of bacterial indicator organisms for monitoring the *Salmonella Enteritidis* status of layer farms after cleaning and disinfection, *Poultry Science* **90** (6), 1185-1190 (2011).

[26] D. Persoons, J. Dewulf, A. Smet, L. Herman, M. Heyndrickx, A. Martel, B. Catry, P. Butaye and F. Haesebrouck, Prevalence and persistence of antimicrobial resistance in broiler indicator bacteria, *Microbial Drug Resistance* **16** (1), 67-74 (2010).

[27] J. L. Holland, L. Louie, A. E. Simor and M. Louie, PCR detection of *Escherichia coli* O157 : H7 directly from stools: Evaluation of commercial extraction methods for purifying fecal DNA, *Journal of Clinical Microbiology* **38** (11), 4108-4113 (2000).

[28] B. Masschelein, A. Robles-Kelly, C. Blanch, N. Tack, B. Simpson-Young and A. Lambrechts, Towards a colony counting system using hyperspectral imaging, *Imaging, Manipulation, and Analysis of Biomolecules, Cells, and Tissues X* **8225**, (2012).

[29] Z. J. Zhang, Y. J. Guan, M. Li, A. D. Zhao, J. S. Ren and X. G. Qu, Highly stable and reusable imprinted artificial antibody used for in situ detection and disinfection of pathogens, *Chemical Science* **6** (5), 2822-2826 (2015).

[30] ISO, 2001. ISO 16649-2:2001(en). Microbiology of food and animal feeding stuffs - Horizontal method for the enumeration of beta-glucuronidase-positive Escherichia coli - Part 2: Colony-count technique at 44 degrees C using 5-bromo-4-chloro-3-indolyl β-D-glucuronide.

[31] O. Lazcka, F. J. Del Campo and F. X. Munoz, Pathogen detection: A perspective of traditional methods and biosensors, *Biosensors and Bioelectronics* **22** (7), 1205-1217 (2007).

[32] G. A. Zelada-Guillen, S. V. Bhosale, J. Riu and F. X. Rius, Real-time potentiometric detection of bacteria in complex samples, *Analytical Chemistry* **82** (22), 9254-9260 (2010).

[33] B. van Grinsven, K. Eersels, O. Akkermans, S. Ellermann, A. Kordek, M. Peeters, O. Deschaume, C. Bartic, H. Diliën, E. Steen Redeker, P. Wagner and T. J. Cleij, Label-free detection of *Escherichia coli* based on thermal transport through surface imprinted polymers, *ACS Sensors* **1** (9), 1140-1147 (2016).

[34] T. Cohen, J. Starosvetsky, U. Cheruti and R. Armon, Whole cell imprinting in sol-gel thin films for bacterial recognition in liquids: Macromolecular fingerprinting, *International Journal of Molecular Sciences* **11** (4), 1236-1252 (2010).

[35] W. Stilman, S. Jooken, G. Wackers, P. Cornelis, M. Khorshid, D. Yongabi, O. Akkermans, S. Dyson, B. van Grinsven, T. Cleij, L. van Ijzendoorn, P. Wagner and K. Eersels, Optimization and characterization of a flow cell for heat-transfer-based biosensing, *Physica Status Solidi a-Applications and Materials Science* **214** (9), 1600758 (2017).

Modified Heat-Transfer Method

[36]   EC, 2007. Commission Regulation (EC) No 1441/2007 of 5 December 2007 amending Regulation (EC) No 2073/2005 on microbiological criteria for foodstuffs.

[37]   EC, 1998. Council Directive 98/83/EC of 3 November 1998 on the quality of water intended for human consumption.

[38]   EC, 2003. Proposal for a Directive of the European Parliament and of the Council concerning the quality of bathing water (2003/C 45 E/15) COM(2002) 581 final - 2002/0254(COD).

[39]   Finetubes: http://www.finetubes.de/uploads/attachments/g145_Legierungen_304_und_304L.pdf: data retrieved on February 12, 2019.

[40]   M. Bäcker, S. Pouyeshman, T. Schnitzler, A. Poghossian, P. Wagner, M. Biselli and M. J. Schöning, A silicon-based multi-sensor chip for monitoring of fermentation processes, *Physica Status Solidi a-Applications and Materials Science* **208** (6), 1364-1369 (2011).

[41]   Resistor Guide: http://www.resistorguide.com/temperature-coefficient-of-resistance/: data retrieved on October 10, 2016.

[42]   D. Necas and P. Klapetek, Gwyddion: An open-source software for SPM data analysis, *Central European Journal of Physics* **10** (1), 181-188 (2012).

[43]   D. Yongabi, M. Khorshid, P. Losada-Pérez, K. Eersels, O. Deschaume, J. D'Haen, C. Bartic, J. Hooyberghs, R. Thoelen, M. Wübbenhorst and P. Wagner, Cell detection by surface imprinted polymers SIPs: A study to unravel the recognition mechanisms, *Sensors and Actuators B: Chemical* **255**, 907-917 (2018).

[44]   M. V. Pergal, J. V. Dzunuzovic, R. Poreba, D. Micic, P. Stefanov, L. Pezo and M. Spirkova, Surface and thermomechanical characterization of polyurethane networks based on poly(dimethylsiloxane) and hyperbranched polyester, *Express Polymer Letters* **7** (10), 806-820 (2013).

[45]   P. Keblinski, J. A. Eastman and D. G. Cahill, Nanofluids for thermal transport, *Materials Today* **8** (6), 36-44 (2005).

[46]   J. A. Eastman, S. U. S. Choi, S. Li, W. Yu and L. J. Thompson, Anomalously increased effective thermal conductivities of ethylene glycol-based nanofluids containing copper nanoparticles, *Applied Physics Letters* **78** (6), 718-720 (2001).

[47]   S. K. Yadav, Dose–response models to understand toxicodynamics for pollutants in ecosystems, *International Journal of Environmental Science: Development and Monitoring* **4** (3), 4 (2013).

[48]   D. Mara, 2003. Faecal indicator organisms. In: D. Mara and N. Horan (Eds.), Handbook of Water and Wastewater Microbiology, 105-112. Academic Press.

[49]   A. Gennaro, D. Yongabi, O. Deschaume, C. Bartic, P. Wagner and M. Wübbenhorst, Cell detection by surface imprinted polymers (SIPs) - A study of the sensor surface by optical and dielectric relaxation spectroscopy, *IEEE Transactions on Dielectrics and Electrical Insulation* **25** (3), 816-821 (2018).

[50]   K. N. Ren and R. N. Zare, Chemical recognition in cell-imprinted polymers, *Acs Nano* **6** (5), 4314-4318 (2012).

[51]   F. Q. Li and J. Kosel, An efficient biosensor made of an electromagnetic trap and a magneto-resistive sensor, *Biosensors and Bioelectronics* **59**, 145-150 (2014).

[52]   S. Tokonami, Y. Nakadoi, M. Takahashi, M. Ikemizu, T. Kadoma, K. Saimatsu, L. Q. Dung, H. Shiigi and T. Nagaoka, Label-free and selective bacteria detection using a film with transferred bacterial configuration, *Analytical Chemistry* **85** (10), 4925-4929 (2013).

[53]   N. A. Masdor, Z. Altintas and I. E. Tothill, Sensitive detection of *Campylobacter jejuni* using nanoparticles enhanced QCM sensor, *Biosensors and Bioelectronics* **78**, 328-336 (2016).

[54]   N. Idil, M. Hedstrom, A. Denizli and B. Mattiasson, Whole cell based microcontact imprinted capacitive biosensor for the detection of *Escherichia coli*, *Biosensors and Bioelectronics* **87**, 807-815 (2017).

[55]   Engineering Toolbox: https://www.engineeringtoolbox.com/thermal-conductivity-d_429.html: data retrieved on November 13, 2018.

Chapter 4: Software Development

4.1 Introduction

For the experiments involving meander calibration, the EBU/DISC combination (**Chapter 2**) or the modified HTM (**Chapter 3**), custom control programs were written in-house using the LabVIEW graphical programming language. These three programs played a major role in enabling most of the measurements related to the two projects discussed in this work: The differential impedimetric sensor cell (DISC) in **Chapter 2** and the modified heat-transfer method (HTM) in **Chapter 3**. Both projects were successfully published in respectively Physica Status Solidi a[1] and Biosensors & Bioelectronics[2]. Moreover, a slightly adapted version of the LabVIEW program that controls the EBU/DISC combination, which was updated to support different hardware, has been used in several other research projects: This includes, the detection of Vitamin K by MIP receptors[3], the direct detection of bacteria obtained from contaminated surfaces using SIP receptors[4], the detection of small organic molecules by MIP-functionalized thermocouples[5], the detection of bacteria using thermal wave transport analysis through SIP receptors[6], and the optimization and characterization of a flowcell for heat-transfer based biosensing applications[7].

4.2 General Concept

For ease of maintenance and future upgradability, a high degree of modularity was pursued in constructing the program flow. At the highest level, the programs consist of three large modules: The graphical user interface (GUI), data logging, and measurement process control. The GUI, as its name implies, is the part of the program that the user interacts with and therefore it needs to be able to respond quickly to any input by the user. Moreover, it should assist the user in operating the program correctly. For example, by temporarily

enabling/disabling certain functions of the program, by asking for additional required information, or by asking for conformation before executing certain functions. Data logging is generally the slowest part of the program as it needs to write the data to a physical long-term storage device, such as a hard disc drive (HDD) or solid-state drive (SSD). The measurement process control module is the actual core of the program, as it executes the most compute-intensive functions of the program, such as communicating with the attached devices, processing the measurement results, and responding to these generated results.

For optimal program performance the communication between these three modules needs to be as efficient as possible. In general, there are two methods to implement the inter-module communication. One uses a shared variable and the other a dataqueue (**Figure 4-1**). When a shared variable is used, the module that needs to receive the data continuously polls the content of the shared variable (1) (usually every 10 – 100 ms) and executes the appropriate function or functions based on its contents or remains idle in case the variable is empty. This system is easy to implement and responds only when the sender module writes request into the shared variable (2). However, a trade-off needs to be made between a very responsive system with a polling cycle time of only a few milliseconds, which also spends a lot of time not doing any valuable work because it is busy reading a variable that does not change very often, and a system that limits the amount of time it spends polling the shared variable, but is not very responsive (polling cycle time greater than 100 ms). These days systems that are not responsive enough to user input can easily lead to a frustrating user experience.

Dataqueues require more programming experience to implement. However, they provide the fastest way to communicate between individual modules. The sender module writes a request into the dataqueue (1). At that time, and only then, the receiver module is notified of the presence of a new request that needs to be processed (2). Next, the receiver module reads and removes the request from the dataqueue and executes the appropriate functions (3). This system

is both very responsive and it does not spend any time unnecessarily reading a variable. This is especially useful for complex and very compute-intensive programs as it allows for a very responsive user interface while still allocating almost all available computational power to the process control module. Similarly, it allows the process control module to continue working as fast as possible while its generated data is stored in a queue, which can be transferred to permanent storage at a later time by the data logging module. The three general modules themselves also consist of multiple modules. For example, for each device a set of modules was created to provide a simple interface to ease integration into other programs.
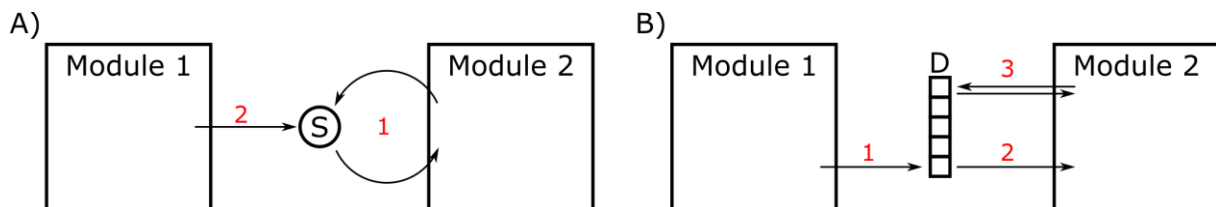
Figure 4-1 *Schematic illustration of inter-module communication using a shared variable (A) or a dataqueue (B). Using the shared variable, module 2 continuously polls the variable (1) waiting for changes introduced by module 1 (2). In case of a dataqueue, module 2 is notified (2) when a new request is added by module 1 (1). Only then will module 2 read the contents of the dataqueue to receive the request sent by module 1.*

Figure 4-2 shows the GUI for the meander calibration program, which only uses two multi-meters to measure the resistance of the meander and the Pt100, and a conversion module to calculate the temperature in °C from the resistance of the Pt100.
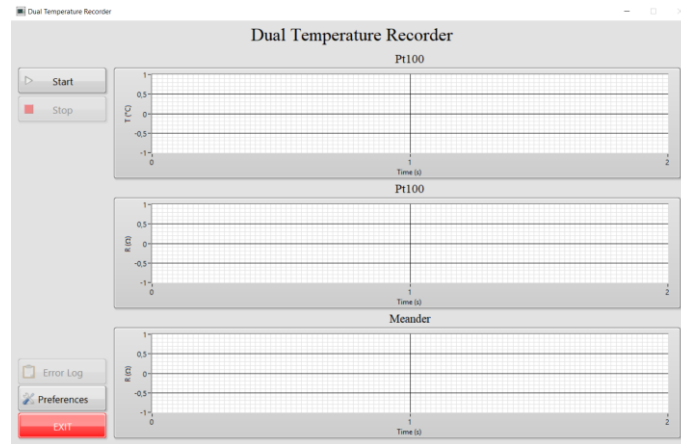
Figure 4-2 Graphical user interface (GUI) for the LabVIEW meander calibration program.

Figure 4-3 shows the GUI for the EBU/DISC control program. This program includes the remotely controlled pumps and the software based PID controller, which will be discussed in more detail in the following two paragraphs.
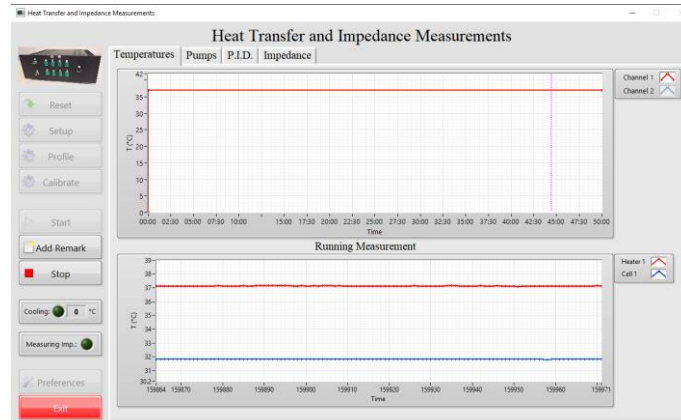
Figure 4-3 Graphical user interface (GUI) for the LabVIEW program that performs HTM and impedance measurements using the EBU/DISC device combination.

Figure 4-4 shows the GUI for the meander-based HTM measurement program. It also includes the remotely controlled pumps and a different version of the software based PID controller. It also has a module for Three-Point Delta resistance measurements. However, it does not include the impedance module.
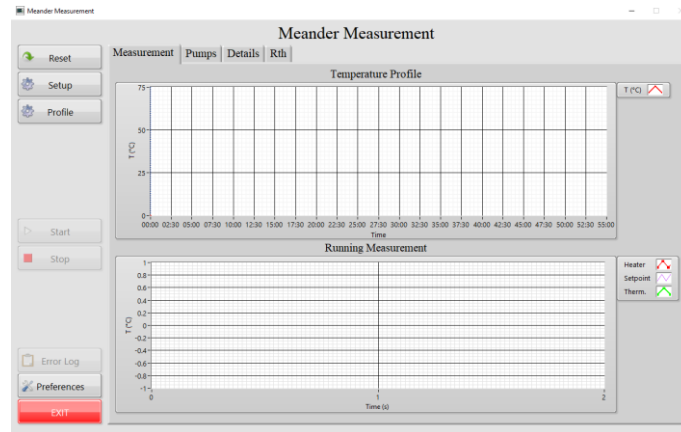
Figure 4-4 *Graphical user interface (GUI) for the LabVIEW program that performs meander-based HTM measurements.*

4.3 Syringe Pump Controller

The modules to control the syringe pumps required some additional attention as multiple pumps were attached using a single serial communication interface on the computer and each pump has its own controller module running in parallel with the others. It was therefore important to ensure that a request sent to one pump does not interfere with a request sent to another pump. To achieve this a semaphore was used. This is a special kind of global variable, which is available to all modules. When this variable is enabled, other modules, which are synchronized with this variable, must wait until it has been disabled by the module that originally enabled it. Essentially, this means that while one module is busy sending a request to one of the pumps, the other modules cannot send a request to the pumps until that module has finished sending its request.

4.4 PID Controller

In order to control the temperature of a heater, an algorithm is combined with a feedback loop. The algorithm calculates new values to be send to the heater controller at fixed time intervals based on the last three recorded differences between the required temperature and the

measured temperature. Therefore, this algorithm acts as a setpoint controller. The controller implements a proportional value (P) as the present error, where the integral (I) and derivative (D) respectively correspond to the average of the past errors and the prediction of future errors[8, 9]. In a next step, the controller combines these values to calculate a correction value, which is then added to the current signal that is being send to the heater controller. In case of a heater consisting of a copper block and power resistor, the PID-controller calculates new values for the voltage supplied to the power resistor. Whereas, for a meander-based heater, it calculates new values for the current supplied to the meander.

References

[1]   P. Cornelis, G. Wackers, I. Thomas, M. Brand, T. Putzeys, A. Gennaro, M. Wübbenhorst, S. Ingebrandt and P. Wagner, A novel modular device for biological impedance measurements: The differential impedimetric sensor cell (DISC), *Physica Status Solidi a-Applications and Materials Science* **215** (15), 1701029 (2018).

[2]   P. Cornelis, S. Givanoudi, D. Yongabi, H. Iken, S. Duwé, O. Deschaume, J. Robbens, P. Dedecker, C. Bartic, M. Wübbenhorst, M. J. Schöning, M. Heyndrickx and P. Wagner, Sensitive and specific detection of *E. coli* using biomimetic receptors in combination with a modified heat-transfer method, *Biosensors and Bioelectronics* **136**, 97-105 (2019).

[3]   K. Eersels, H. Diliën, J. W. Lowdon, E. Steen Redeker, R. Rogosic, B. Heidt, M. Peeters, P. Cornelis, P. Lux, C. P. Reutelingsperger, L. J. Schurgers, T. J. Cleij and B. van Grinsven, A novel biomimetic tool for assessing vitamin K status based on molecularly imprinted polymers, *Nutrients* **10** (6), 751 (2018).

[4]   B. van Grinsven, K. Eersels, S. Erkens-Hulshof, H. Diliën, K. Nurekeyeva, P. Cornelis, D. Klein, F. Crijns, G. Tuijthof, P. Wagner, E. Steen Redeker and T. J. Cleij, SIP-based thermal detection platform for the direct detection of bacteria obtained from a contaminated surface, *Physica Status Solidi a-Applications and Materials Science* **215** (15), 1700777 (2018).

[5]   H. Diliën, M. Peeters, J. Royakkers, J. Harings, P. Cornelis, P. Wagner, E. Steen Redeker, C. E. Banks, K. Eersels, B. van Grinsven and T. J. Cleij, Label-free detection of small organic molecules by molecularly imprinted polymer functionalized thermocouples: Toward in vivo applications, *ACS Sensors* **2** (4), 583-589 (2017).

[6]   E. Steen Redeker, K. Eersels, O. Akkermans, J. Royakkers, S. Dyson, K. Nurekeyeva, B. Ferrando, P. Cornelis, M. Peeters, P. Wagner, H. Diliën, B. van Grinsven and T. J. Cleij, Biomimetic bacterial identification platform based on Thermal Wave Transport Analysis (TWTA) through surface-imprinted polymers, *ACS Infectious Diseases* **3** (5), 388-397 (2017).

[7]   W. Stilman, S. Jooken, G. Wackers, P. Cornelis, M. Khorshid, D. Yongabi, O. Akkermans, S. Dyson, B. van Grinsven, T. Cleij, L. van Ijzendoorn, P. Wagner and K. Eersels, Optimization and characterization of a flow cell for heat-transfer-based biosensing, *Physica Status Solidi a-Applications and Materials Science* **214** (9), 1600758 (2017).

[8]   K. J. Äström and R. M. Murray, 2008. Feedback Systems: An Introduction for Scientists and Engineers. Princeton University Press.

[9]   K. J. Äström, 2002. PID Control. In Control System Design, 216-251. University of California Press, Santa Barbara, CA, USA.

Chapter 5: General Conclusions and Outlook

This work focused on advancing two transducer platforms for biomimetic receptors: electrochemical impedance spectroscopy, which is already widely used, and the recently developed heat-transfer method. For the EIS platform the emphasis was on designing an innovative and cost-effective device for bioanalytical applications while for the HTM platform the emphasis was on lowering its detection limits in order to widen its range of possible applications.

Currently, a wide variety of biosensing applications based on impedance spectroscopy is already available, such as histamine detection using MIPs[1], atrazine detection using antibodies[2], and fingerprinting of *E. coli* biofilms[3]. These systems all have a single target that they can detect. However, some application cases require the detection of multiple targets in a sample. For instance, the presence of cadaverine dramatically increases the toxicity of histamine[4, 5]. To this end, the DISC/EBU system was designed. It is capable of sequentially measuring up to eight channels inside a temperature-controlled flow cell, which is important as the impedance of a material depends not only on the frequency, but also the temperature[6]. This enables it to measure up to seven or eight different targets compounds, depending on whether a reference channel is used or not, in a single small liquid sample. The availability of reference channels allows for performing differential measurements, which simplifies sample pre-treatment because any noise in the measurement signal caused by impurities in the sample can simply be removed by subtracting the reference channel from the measurement channel. Moreover, the performance of the DISC/EBU system was validated against a high-resolution dielectric spectrometer from Novocontrol. However, phase angle measurements can still be improved. This is an important parameter because at low frequencies, where the characteristics of the biosensor surface are analyzed, the double-layer capacitance of the surface is its main

contributor. At the moment, only a set of ten different resistors is used to calibrate the impedance analyzer. Therefore, adding a set of ten different capacitors to the calibration procedure could possibly improve the phase angle measurement capabilities of the analyzer.

Concerning the HTM platform, a completely new device was designed based on the thermal analysis of the original design[7]. The entire sample compartment of the device is still no larger than a matchbox. However, its LoD for cell detection has been significantly improved from around 10^4 CFU/mL to 100 CFU/mL. Moreover, this low LoD was also reached in more complex real-life samples such as non-cleared apple juice without requiring sample pre-treatment. This means that this improved HTM device has now reached a performance level which brings the original HTM concept for cell detection from 2013[8] very close to real-life applications. Moreover, it is a generic concept which can be easily adapted for other micro-organisms and other types of biomimetic receptors, such as MIPs for histamine detection. The sensor chips used in this work were SIPs designed to detect *E. coli*, which used readily available and corrosion-resistant stainless-steel as their support material. However, there are still some challenges that need to be overcome before this new platform is ready for application in a real-life context. A possible solution would be the development of an efficient washing protocol to regenerate the SIP inside the HTM platform and the development of a more efficient technique to prepare SIP receptors, which could possibly be based on the "master stamp" concept[9, 10]. In general, the creation of a "master stamp" is a two-step process. In a first step, MIPs or SIPs are produced, which are negative images of the target. In the second step, these MIPs or SIPs are used to create a new SIP, the master stamp, which will be a positive image (replica) of the original target. These master stamps can then be used instead of the real target to produce large quantities of SIPs with a consistent quality because they are more robust then their natural analogues. Both previously mentioned developments are required to enable long term monitoring applications.

In this work both transducer platforms use a flow-through flow cell, so experience gained from designing the flow cell for one platform can probably be transferred to the other platform. Moreover, it should be possible to combine both platforms into a single device.

References

[1]   M. Peeters, F. J. Troost, R. H. G. Mingels, T. Welsch, B. van Grinsven, T. Vranken, S. Ingebrandt, R. Thoelen, T. J. Cleij and P. Wagner, Impedimetric detection of histamine in bowel fluids using synthetic receptors with pH-optimized binding characteristics, *Analytical Chemistry* **85** (3), 1475-1483 (2013).

[2]   R. E. Ionescu, C. Gondran, L. Bouffier, N. Jaffrezic-Renault, C. Martelet and S. Cosnier, Label-free impedimetric immunosensor for sensitive detection of atrazine, *Electrochimica Acta* **55** (21), 6228-6232 (2010).

[3]   E. Goikoetxea, D. Routkevitch, A. de Weerdt, J. J. Green, H. Steenackers and D. Braeken, Impedimetric fingerprinting and structural analysis of isogenic *E. coli* biofilms using multielectrode arrays, *Sensors and Actuators B: Chemical* **263**, 319-326 (2018).

[4]   L. Lehane and J. Olley, Histamine fish poisoning revisited, *International Journal of Food Microbiology* **58** (1-2), 1-37 (2000).

[5]   L. F. Bjeldanes, D. E. Schutz and M. M. Morris, On the aetiology of scombroid poisoning: cadaverine potentiation of histamine toxicity in the guinea-pig, *Food and Cosmetics Toxicology* **16** (2), 157-159 (1978).

[6]   W. Chen, W. Zhu, O. K. Tan and X. F. Chen, Frequency and temperature dependent impedance spectroscopy of cobalt ferrite composite thick films, *Journal of Applied Physics* **108** (3), 034101 (2010).

[7]   W. Stilman, S. Jooken, G. Wackers, P. Cornelis, M. Khorshid, D. Yongabi, O. Akkermans, S. Dyson, B. van Grinsven, T. Cleij, L. van Ijzendoorn, P. Wagner and K. Eersels, Optimization and characterization of a flow cell for heat-transfer-based biosensing, *Physica Status Solidi a-Applications and Materials Science* **214** (9), 1600758 (2017).

[8]   K. Eersels, B. van Grinsven, A. Ethirajan, S. Timmermans, K. L. Jiménez Monroy, J. F. Bogie, S. Punniyakoti, T. Vandenryt, J. J. Hendriks, T. J. Cleij, M. J. Daemen, V. Somers, W. De Ceuninck and P. Wagner, Selective identification of macrophages and cancer cells based on thermal transport through surface-imprinted polymer layers, *ACS Applied Materials & Interfaces* **5** (15), 7258-7267 (2013).

[9]   R. Schirhagl, U. Latif, D. Podlipna, H. Blumenstock and F. L. Dickert, Natural and biomimetic materials for the detection of insulin, *Analytical Chemistry* **84** (9), 3908-3913 (2012).

[10]   R. Schirhagl, P. A. Lieberzeit and F. L. Dickert, Chemosensors for viruses based on artificial immunoglobulin copies, *Advanced Materials* **22** (18), 2078-2081 (2010).

Curriculum Vitae

Peter Cornelis was born on February 20, 1975 in Hasselt, Belgium. In 1996, he obtained his bachelor's degree in biology at Hasselt University (known at that time as 'Limburgs Universitair Centrum' or L.U.C.) and graduated in 1998 as master in Biochemistry at Antwerp University. In 1999, he obtained a Postgraduate degree in Biomedical and Clinical Engineering Techniques from KU Leuven. After a few months training he started working as an IT-assistant in the private sector until he returned to study at Hasselt University in 2012. In 2014, he obtained his master's degree in Biomedical Sciences, more specifically in Bioelectronics and Nano-technology. Afterwards, he started his PhD in the ZMB group (Laboratory for Soft Matter and Biophysics) within the Physics and Astronomy department of the KU Leuven. His research interests cover biosensors for medical diagnostics, biophysical systems and more generally all topics that combine multiple science disciplines. Currently, P. Cornelis is author or co-author of more than 10 journal publications and co-inventor of a patent application.

List of Publications and Patents

Publications

1. _**P. Cornelis**_, S. Givanoudi, D. Yongabi, H. Iken, S. Duwé, O. Deschaume, J. Robbens, P. Dedecker, C. Bartic, M. Wübbenhorst, M. J. Schöning, M. Heyndrickx, and P. Wagner, "Sensitive and specific detection of _E. coli_ using biomimetic receptors in combination with a modified heat-transfer method" _Biosensors and Bioelectronics_, 2019, 136, 97-105 (doi: 10.1016/j.bios.2019.04.026).

2. M. Khorshid, P. Losada-Pérez, _**P. Cornelis**_, M. Dollt, S. Ingebrandt, C. Glorieux, F. U. Renner, B. van Grinsven, R. Thoelen, W. De Ceuninck, and P. Wagner, "Exploring the limits of the heat-transfer method HTM: A case study on gold-thiol-ethanol interfaces" _Langmuir_, submitted March, 2019.

3. K. Eersels, H. Diliën, J. W. Lowdon, E. Steen Redeker, R. Rogosic, B. Heidt, M. Peeters, _**P. Cornelis**_, P. Lux, C. P. Reutelingsperger, L. J. Schurgers, T. J. Cleij, and B. van Grinsven, "A novel biomimetic tool for assessing vitamin K status based on molecularly imprinted polymers" _Nutrients_, 2018, 10(6), 751-762 (doi: 10.3390/nu10060751).

4. _**P. Cornelis**_, G. Wackers, I. Thomas, M. Brand, T. Putzeys, A. Gennaro, M. Wübbenhorst, S. Ingebrandt, and P. Wagner, "A novel modular device for biological impedance measurements: The differential impedimetric sensor cell (DISC)" _Physica Status Solidi A_, 2018, 215, 1701029 (doi: 10.1002/pssa.201701029).

5. B. van Grinsven, K. Eersels, S. Erkens-Hulshof, H. Diliën, K. Nurekeyeva, _**P. Cornelis**_, D. Klein, F. Crijns, G. Tuijthof, P. Wagner, E. Steen Redeker, and T. J. Cleij, "SIP-based thermal detection platform for the direct detection of bacteria obtained from a contaminated surface" _Physica Status Solidi A_, 2018, 215, 1700777 (doi: 10.1002/pssa.201700777).

6. T. Vandenryt, B. van Grinsven, K. Eersels, _**P. Cornelis**_, S. Kholwadia, T. J. Cleij, R. Thoelen, W. De Ceuninck, M. Peeters, and P. Wagner, "Single-shot detection of neurotransmitters in whole-blood samples by means of the heat-transfer method in combination with synthetic receptors" _Sensors_, 2017, 17(12), 2701-2712 (doi:10.3390/s17122701).

7. H. Diliën, M. Peeters, J. Royakkers, J. Harings, **_P. Cornelis_**, P. Wagner, E. Steen Redeker, C. E. Banks, K. Eersels, B. van Grinsven, and T. J. Cleij, "Label-free detection of small organic molecules by MIP-functionalized thermocouples: towards in vivo applications" *ACS Sensors*, 2017, 2(4), 583-589.

8. E. Steen Redeker, K. Eersels, O. Akkermans, J. Royakkers, S. Dyson, K. Nurekeyeva, B. Ferrando, **_P. Cornelis_**, M. Peeters, P. Wagner, H. Diliën, B. van Grinsven, and T. J. Cleij, "Biomimetic bacterial identification platform based on thermal wave transport analysis (TWTA) through surface imprinted polymers" *ACS Infectious Diseases*, 2017, 3(5), 388-397.

9. W. Stilman, S. Jooken, G. Wackers, **_P. Cornelis_**, M. Khorshid, D. Yongabi, O. Akkermans, S. Dyson, B. van Grinsven, T. J. Cleij, L. van Ijzendoorn, P. Wagner, and K. Eersels, "Optimization and characterization of a flow cell for heat-transfer-based biosensing" *Physica Status Solidi A*, 2017, 214(9), 1600758 (doi:10.1002/pssa.201600758).

10. M. Peeters, B. van Grinsven, T. J. Cleij, K. L. Jiménez-Monroy, **_P. Cornelis_**, E. Pérez Ruiz, G. Wackers, R. Thoelen, W. De Ceuninck, J. Lammertyn, and P. Wagner, "Label-free protein detection based on the heat-transfer method - A case study with the peanut allergen Ara h 1 and aptamer-based synthetic receptors" *ACS Applied Materials & Interfaces*, 2015, 7(19), 10316-10323.

11. **_P. Cornelis_**, T. Vandenryt, G. Wackers, E. Kellens, P. Losada-Pérez, R. Thoelen, W. De Ceuninck, K. Eersels, S. Drijkoningen, K. Haenen, M. Peeters, B. van Grinsven, and P. Wagner, "Heat transfer resistance as a tool to quantify hybridization efficiency of DNA on a nanocrystalline diamond surface" *Diamond & Related Materials*, 2014, 48, 32-36.

12. G. Wackers, T. Vandenryt, **_P. Cornelis_**, E. Kellens, R. Thoelen, W. De Ceuninck, P. Losada-Pérez, B. van Grinsven, M. Peeters, and P. Wagner, "Array formatting of the heat-transfer method (HTM) for the detection of small organic molecules by molecularly imprinted polymers" *Sensors*, 2014, 14(6), 11016-11030.

Patents

1. P. Wagner, M. Khorshid, **_P. Cornelis_**, and G. Wackers, "Thermic Sensor" → Filed by KU Leuven, U.K., Patent Application No. GB1701291.5, Date: January 26, 2017.